Fermilab

FERMILAB-THESIS-2003-03

Search for $t\bar{t}$ Resonances in $p\bar{p}$ collisions at $\sqrt{s} = 1.8$ TeV

Ph. D. in Physics

Submitted by

Supriya Jain

Under the Guidance of

Prof. N. K. Mondal

Tata Institute of Fundamental Research

Mumbai 400 005

2003

To my parents and sisters

STATUTORY DECLARATIONS

Name of the Candidate	:	Supriya Jain
Title of the Thesis	:	Search for $t\bar{t}$ Resonances in $p\bar{p}$ collisions at $\sqrt{s} = 1.8$ TeV
Degree	:	Doctor of Philosophy
Subject	:	Physics
Name of the Supervisor	:	Professor N. K. Mondal
Registration No.	:	TIFR–201 (5 April, 1999)
Place of Research	:	Tata Institute of Fundamental Research, Mumbai, India

STATEMENT BY THE CANDIDATE

As required by the University Ordinances 770 and 771, I wish to state that the work embodied in this thesis titled **Search for $t\bar{t}$ Resonances in $p\bar{p}$ collisions at $\sqrt{s} = 1.8$ TeV** forms my own contribution to the research work carried out under the guidance of **Prof. N. K. Mondal** at the Tata Institute of Fundamental Research. This work has not been submitted for any other degree of this or any other University. Whenever references have been made to previous works of others, it has been clearly indicated as such and included in the Bibliography.

Certified by,

Signature of the Supervisor	*Signature of the Candidate*
Prof. N. K. Mondal	**Supriya Jain**

Contents

List of Figures . . . . . **xiii**

List of Tables . . . . . **xviii**

Synopsis . . . . . **xix**

0.1 Introduction xix

0.2 The DØ Detector xx

0.3 Data Sample xx

0.4 Monte Carlo Signal and Backgrounds xxi

0.5 Kinematic Fitting xxiii

0.6 Bayesian Fit xxiii

0.7 Upper Limits on $\sigma_X B(X \to t\bar{t})$ xxv

0.8 Effect of Experimental Uncertainties and Results xxvi

0.9 Conclusion xxviii

Bibliography . . . . . **xxviii**

List of Publications . . . . . **xxxi**

Acknowledgments . . . . . **xxxiii**

1 Introduction **1**

1.1 A Brief Tour of the Standard Model 2

1.2 Production and Decay of $t\bar{t}$ pairs in Standard Model 6

1.3 Beyond the Standard Model 9

2 Experimental Apparatus **17**

2.1 Coordinate Systems 17

2.2 Luminosity and Cross Section 19

2.3 The Beam 20

2.4 Overview of the DØ Detector 24

2.5 Central Detectors 25

2.5.1 Vertex Drift Chamber (VTX) 27

2.5.2 Transition Radiation Detector (TRD) 28

2.5.3 Central Drift Chamber (CDC) 29

2.5.4 Forward Drift Chamber (FDC) 31

2.6 Calorimetry 32

2.7 Muon System 37

2.8 Triggering and Readout 41

2.8.1 Electron (and photon) triggers 43

2.8.2 Muon triggers 44

2.8.3 Jet triggers 45

2.8.4 Missing transverse energy ($\not\!\!E_T$) triggers 46

2.8.5 Main Ring Vetoes 46

3 Reconstruction and Particle ID **49**

3.1 The Reconstruction Program 49

3.2 Vertex Finding 51

3.3 Electron Identification 52

3.3.1 Candidate Construction 53

3.3.2 Efficiency 58

3.3.3 Electron Energy Corrections 60

3.4 Muon Identification 61

3.4.1 Efficiency 63

3.5 Jet Reconstruction 64

3.5.1 Cone Jet Algorithm 66

3.5.2 Jet Energy Corrections 67

3.6 Missing Energy Reconstruction 74

3.6.1 Definition of Missing Transverse Energy 75

4 Data sample and Event Selection. **77**

4.1 Data sample 79

4.2 Principal sources of background 80

4.3 Selection Criteria 83

4.3.1 Topological analysis 83

4.3.2 Tag analysis 86

5 Kinematic fit **91**

5.1 Constrained Fit 92

5.2 Determination of p_z^ν 95

5.3 Error matrix **G** 95

5.4 Results from the kinematic fit 96

6 Event simulation 101

7 Data Analysis 107

7.1 Bayesian fit of data to a three-source model 107

7.2 Extraction of upper limits on $\sigma_X B$ 114

7.2.1 Calculation of acceptance ($\mathcal{A}$) 124

7.2.2 Upper limits on $\sigma_X B$ 136

8 Systematic uncertainties and Results 145

8.1 Upper limits on $\sigma_X B$ including errors on $\mathcal{AL}$ 148

8.2 Results 150

9 Conclusions 153

A Jet-parton permutations 155

B Simplification for $P(f_1, f_2, f_3|D, M_X)$ 157

C Electron ID efficiency for Monte Carlo events 159

D Correction for the branching fraction ($\mathcal{B}$) 165

E $(\sigma_X B)_{95}$ using an alternate approach 169

F $(\sigma_X B)_{95}$ with Gaussian priors for backgrounds 177

Bibliography 179

List of Figures

1 Normalized distributions of $m_{t\bar{t}}$ for sum of all Standard Model backgrounds (shaded) and sum of signal ($X \rightarrow t\bar{t}$) and Standard Model backgrounds (unshaded) for $M_X = 600$ GeV/c^2. The data $m_{t\bar{t}}$ distribution is shown by dots. xxvi

2 The DØ Run I 95% confidence level upper limits on $\sigma_X B$ as a function of resonance mass M_X. Included for reference are the predicted topcolor assisted technicolor cross sections for a width $\Gamma_X = 1.2\%\ M_X$.xxviii

1.1 Lowest order $t\bar{t}$ production processes. 7

1.2 The ETC vector gauge boson of mass M_{ETC} mediating interactions between fermions (f) and technifermions (F) via the coupling g_{ETC}, at scales $\Lambda_{ETC} >> \Lambda_{TC}$. 12

2.1 Schematic of the Fermilab accelerator complex. 21

2.2 Cutaway view of the DØ detector. 26

2.3 Side view of the DØ central detector. 27

2.4 End view of one quadrant of the VTX chamber. 28

2.5 A cross section of a TRD layer. 29

2.6 End view of 3 of 32 CDC modules. 30

2.7 Exploded view of one of the FDCs. 31

2.8 The DØ calorimeter. 33

2.9 Schematic view of a calorimeter cell. 34

2.10 Side view of the calorimeters. 36

2.11 Side elevation of the muon system. 38

2.12 Number of nuclear interaction lengths as a function of polar angle. . 39

2.13 An elevation view of the DØ detector showing the location of the muon scintillation counters. 40

3.1 Jet evolution. (a) Jets at *parton*, *particle* and *calorimeter* levels. (b) Section of the calorimeter with individual particle showers. 65

3.2 The measured jet energies for quarks from $W \to q\bar{q}$ in $t\bar{t}$ Monte Carlo events are plotted against the corresponding parton energies. Radiation outside the jet cone causes the measured jet energy to be lower than the energy at the parton level. The dashed line is drawn along the diagonal, and the solid line is a linear fit to the points. This plot is based on HERWIG fragmentation with $|\eta_{det}^{\rm jet}| < 0.2$. 70

3.3 The energy scale deviation ΔS as a function of η_{det}^{j} for (a) data and (b) Monte Carlo (MC). The curves are empirical multi-Gaussian fits to the points. 72

3.4 The relative energy scale difference between data and Monte Carlo as a function of photon E_T after all jet corrections are applied. The curves indicate an error band of $\pm(2.5\% + 0.5\,\mathrm{GeV})$ of the jet energy. 73

3.5 Transverse energy balance for $(Z \to ee) +$jets events. All jet corrections are applied. The curve is a Gaussian fit to the histogram. . . . 73

3.6 Masses of $W \to q\bar{q}$ and $t \to bq\bar{q}$ in standard $t\bar{t}$ Monte Carlo with $m_t = 175\,\mathrm{GeV}/c^2$, both (a), (b) with standard corrections only and (c), (d) with all jet corrections. The arrows locate the input W boson and top quark masses. 74

4.1 A $t\bar{t} \to l$ + jets decay. 78

4.2 E_T^W distribution for Monte Carlo W+jets events (solid histogram), QCD multijet background data (dashed histogram), and $t\bar{t}$ signal with $m_t = 175\,\mathrm{GeV}/c^2$ (dotted histogram) [33]. All preselections are applied except for the E_T^W cut. The arrow shows the cut value. . . . 84

4.3 $|\eta^W|$ distribution for data (histogram), predicted Standard Model $t\bar{t}$ plus non–$t\bar{t}$ background (filled circles), and non–$t\bar{t}$ background alone (open triangles). All preselections are applied except for the η^W cut. The arrow shows the cut value. 85

4.4 Distribution of $\Delta\phi(\not\!\!E_T, \mu)$ vs. $\not\!\!E_T$ for e + jets/μ events for (a) multijet background sample; (b) W + jets sample (VECBOS Monte Carlo); (c) Standard Model (SM) $t\bar{t}$ Monte Carlo (ISAJET, $m_t = 140$ GeV/c^2); (d) SM $t\bar{t}$ Monte Carlo (ISAJET, $m_t = 160$ GeV/c^2). The contour shows the cut values. 87

4.5 The correlation between $\not\!\!E_T$ and the azimuthal angle between $\not\!\!E_T$ and the highest-p_T muon for μ + jets/μ events for (a) VECBOS W + jets Monte Carlo ($\int \mathcal{L}dt = 80$ pb^{-1}); (b) ISAJET SM $t\bar{t}$ Monte Carlo (m_t = 160 GeV/c^2, 3240 pb^{-1}); (c) multijet events with a non-isolated high-p_T muon with no μ–tag; (d) multijet events with a non-isolated high-p_T muon with an additional tagging muon. 88

5.1 χ^2 distribution for 3 degrees of freedom and the χ^2 distribution (normalized to unity after preselections) for the **correct** jet-parton permutation in the $e+jets$ channel for Standard Model $t\bar{t}$ production. It can be seen that there are very few events beyond $\chi^2 = 10$ indicated by the arrow. 97

5.2 χ^2 for the **best** permutation for DØ Run I lepton+jets data, Standard Model $t\bar{t}$ production, W+jets and multijets backgrounds. Preselections are applied and the contents in all four channels (ej, ej/μ, μj, $\mu j/\mu$) are added. *Efficiency* is defined as the fraction of preselected events that remain after the $\chi^2 < 10$ cut. *Rejection* is defined as the fraction of preselected events that are eliminated by the $\chi^2 < 10$ cut. 98

5.3 χ^2 distribution for X $\rightarrow t\bar{t}$ at $M_X = 600$ GeV/c^2 and 350 GeV/c^2. Preselections are applied and the contents in all four channels (ej, ej/μ, μj, $\mu j/\mu$) are added. 98

5.4 χ^2 distribution for X $\rightarrow t\bar{t}$ at $M_X = 400$ GeV/c^2 and 450 GeV/c^2. Pre-selections are applied and the contents in all four channels (ej, ej/μ, μj, $\mu j/\mu$) are added. 99

5.5 χ^2 distribution for X $\rightarrow t\bar{t}$ at $M_X = 500$ GeV/c^2 and 550 GeV/c^2. Pre-selections are applied and the contents in all four channels (ej, ej/μ, μj, $\mu j/\mu$) are added. 99

5.6 χ^2 distribution for X $\rightarrow t\bar{t}$ at $M_X = 650$ GeV/c^2 and 750 GeV/c^2. Pre-selections are applied and the contents in all four channels (ej, ej/μ, μj, $\mu j/\mu$) are added. 100

5.7 χ^2 distribution for X $\rightarrow t\bar{t}$ at M_X = 850 GeV/c^2 and 1000 GeV/c^2. Pre-selections applied and the contents in all four channels (ej, ej/μ, μj, $\mu j/\mu$) are added. 100

6.1 Distributions of $m_{t\bar{t}}$ for DØ Run I lepton plus jets data, Standard Model $t\bar{t}$ production, W + jets and multijets combined in the ratio 0.78:0.22, and signal ($X \rightarrow t\bar{t}$) for $M_X = 600$ GeV/c^2. The histograms are not normalized. 105

6.2 Distributions of $m_{t\bar{t}}$ for signal ($X \rightarrow t\bar{t}$) for M_X = 350-1000 GeV/c^2. The histograms are not normalized. The bin size is different for different M_X, and also non-uniform in $m_{t\bar{t}}$. 106

7.1 P($n_1|D$, M_X), P($n_2|D$, M_X) and P($n_3|D$, M_X) versus n_1, n_2 and n_3 respectively for $M_X = 600$ GeV/c^2. 113

7.2 Normalized distributions of $m_{t\bar{t}}$ for sum of all Standard Model (SM) backgrounds (shaded histogram) and sum of signal ($X \rightarrow t\bar{t}$) and SM backgrounds (unshaded histogram) for M_X = 350 and 400 GeV/c^2. The data $m_{t\bar{t}}$ distribution is shown by dots along with the statistical errors. 115

7.3 Normalized distributions of $m_{t\bar{t}}$ for sum of all SM backgrounds (shaded histogram) and sum of signal ($X \rightarrow t\bar{t}$) and SM backgrounds (unshaded histogram) for M_X = 450 GeV/c^2 and 500 GeV/c^2. The data $m_{t\bar{t}}$ distribution is shown by dots. 116

7.4 Normalized distributions of $m_{t\bar{t}}$ for sum of all SM backgrounds (shaded histogram) and sum of signal ($X \to t\bar{t}$) and SM backgrounds (unshaded histogram) for M_X = 550 and 600 GeV/c^2. The data $m_{t\bar{t}}$ distribution is shown by dots. 117

7.5 Normalized distributions of $m_{t\bar{t}}$ for sum of all SM backgrounds (shaded histogram) and sum of signal ($X \to t\bar{t}$) and SM backgrounds (unshaded histogram) for M_X = 650 and 750 GeV/c^2. The data $m_{t\bar{t}}$ distribution is shown by dots. 118

7.6 Normalized distributions of $m_{t\bar{t}}$ for sum of all SM backgrounds (shaded histogram) and sum of signal ($X \to t\bar{t}$) and SM backgrounds (unshaded histogram) for M_X = 850 and 1000 GeV/c^2. The data $m_{t\bar{t}}$ distribution is shown by dots. 119

7.7 Normalized distributions of the transverse momentum of top quark (p_T^t) for sum of all SM backgrounds (shaded histogram) and sum of signal ($X \to t\bar{t}$) and SM backgrounds (unshaded histogram) for M_X = 400, 500, 600 and 750 GeV/c^2. The data p_T^t distribution is shown by dots. 120

7.8 Normalized distributions of the transverse momentum of anti-top quark ($p_T^{\bar{t}}$) for sum of all SM backgrounds (shaded histogram) and sum of signal ($X \to t\bar{t}$) and SM backgrounds (unshaded histogram) for M_X = 400, 500, 600 and 750 GeV/c^2. The data $p_T^{\bar{t}}$ distribution is shown by dots. 121

7.9 Normalized distributions of the difference in pseudorapidity η between the two top quarks ($|\Delta\eta^{t,\bar{t}}|$). The shaded histogram is the sum of all SM backgrounds, and the unshaded histogram is the sum of signal ($X \rightarrow t\bar{t}$) and SM backgrounds for M_X = 400, 500, 600 and 750 GeV/c^2. The data $|\Delta\eta^{t,\bar{t}}|$ distribution is shown by dots. 122

7.10 Normalized distributions of the difference in azimuthal angle ϕ between the two top quarks ($|\Delta\phi^{t,\bar{t}}|$). The shaded histogram is the sum of all SM backgrounds, and the unshaded histogram is the sum of signal ($X \rightarrow t\bar{t}$) and SM backgrounds for M_X = 400, 500, 600 and 750 GeV/c^2. The data $|\Delta\phi^{t,\bar{t}}|$ distribution is shown by dots. 123

7.11 The posterior probability density and the cumulative probability vs. $\sigma_X B$ for M_X = 350 and 400 GeV/c^2. The arrow shows the 95% confidence level upper limit on $\sigma_X B$. 137

7.12 The posterior probability density and the cumulative probability vs. $\sigma_X B$ for M_X = 450 and 500 GeV/c^2. The arrow shows the 95% confidence level upper limit on $\sigma_X B$. 137

7.13 The posterior probability density and the cumulative probability vs. $\sigma_X B$ for M_X = 550 and 600 GeV/c^2. The arrow shows the 95% confidence level upper limit on $\sigma_X B$. 138

7.14 The posterior probability density and the cumulative probability vs. $\sigma_X B$ for M_X = 650 and 750 GeV/c^2. The arrow shows the 95% confidence level upper limit on $\sigma_X B$. 138

7.15 The posterior probability density and the cumulative probability vs. $\sigma_X B$ for M_X = 850 and 1000 GeV/c^2. The arrow shows the 95% confidence level upper limit on $\sigma_X B$. 139

7.16 The DØ Run I 95% confidence level upper limits on $\sigma_X B$ as a function of resonance mass M_X. W+jets and multijets are combined in the ratio 0.78:0.22. Included for reference are the predicted topcolor assisted technicolor cross sections for a width, $\Gamma_X = 1.2\%\ M_X$. . . . 141

8.1 The DØ Run I 95% confidence level upper limits on $\sigma_X B$ as a function of resonance mass M_X. W+jets and multijets are combined in the ratio 0.78:0.22. The error on $\sum_i A_i \mathcal{L}_i$ is included as a Gaussian in the expression for the posterior probability density for $\sigma_X B$. Included for reference are the predicted topcolor assisted technicolor cross sections for a width, $\Gamma_X = 1.2\%\ M_X$. 151

C.1 The transverse momentum, p_T, of the matched reconstructed electron and the leading electron at generator-level with $p_T > 18$ GeV/c, in the **CC** and the **EC**, for a sample of Standard Model $t\bar{t}$ production generated using Pythia. 162

C.2 Plots (a) and (b) show the p_T of the matched reconstructed electron versus the p_T of the leading electron at generator-level, in the CC and EC respectively, for a sample of Standard Model $t\bar{t}$ production generated using Pythia. Plots (c) and (d) show the histograms for the difference between the p_T of the matched reconstructed electron and that of the leading electron at generator-level, in the CC and EC respectively. 163

C.3 The Monte Carlo electron identification efficiency in the CC versus M_X. The errors shown are statistical. 164

E.1 The maximum likelihood estimate vs. $\sigma_X B$ for different M_X. While maximizing the likelihood, the parameters α and β are constrained to be > 0 in MINUIT. 172

E.2 The DØ Run I 95% confidence level upper limits on $\sigma_X B$ as a function of resonance mass M_X. While maximizing the likelihood, the parameters α and β are constrained to be > 0 in MINUIT. Included for reference are the predicted topcolor assisted technicolor cross sections for a width, $\Gamma_X = 1.2\%\ M_X$. 173

E.3 The maximum likelihood estimate vs. $\sigma_X B$ for different M_X. While maximizing the likelihood, no constraint is applied on the parameters α and β in MINUIT. 174

E.4 The DØ Run I 95% confidence level upper limits on $\sigma_X B$ as a function of resonance mass M_X. While maximizing the likelihood, no constraint is applied on the parameters α and β in MINUIT. Included for reference are the predicted topcolor assisted technicolor cross sections for a width, $\Gamma_X = 1.2\%\ M_X$. 175

List of Tables

1 Summary of event selections xxii

2 The expected numbers of signal ($X \to t\bar{t}$) counts $< n_1 >$ and background counts from Standard Model $t\bar{t}$ production $< n_2 >$ and from W+jets and multijets $< n_3 >$ for different M_X. 41 events are observed in the $m_{t\bar{t}}$ distribution of l + jets data after applying the precuts and the $\chi^2 < 10$ cut. xxv

3 The 95% C.L. upper limits on $\sigma_X \times B(X \to tt)$ for narrow resonances of mass M_X and natural width $\Gamma_X = 0.012 M_X$ decaying into $t\bar{t}$. . . xxvii

1.1 Particles of the Standard Model [1]. 3

1.2 Possible decay modes for a $t\bar{t}$ pair. 8

1.3 The 18 independent parameters of the Standard Model. 9

2.1 Tevatron Parameters for Run I. 24

3.1 Summary of electron ID cuts. 59

3.2 Summary of muon ID cuts. 64

3.3 Parameters for parton-level jet corrections. $E(\text{corr.}) = (\text{E}_{\text{jet}}^{\text{ptcl}} - \text{A})/\text{B}$. 71

4.1 Triggers used during run Ia (1992–1993). "Exposure" gives the effective integrated luminosity for each trigger, taking into account any prescaling. 80

4.2 Same as Table **??** for run Ib (1994–1995). 81

4.3 Same as Table **??** for run Ic (1995–1996). 82

4.4 Summary of event selections ('preselections') 89

5.1 Object resolutions. The operator $\oplus$ denotes a sum in quadrature. . . 96

7.1 The mean number of signal counts, $< n_1 >$, from $X \to t\bar{t}$, and background counts from Standard Model $t\bar{t}$ production, $< n_2 >$, as well as from W+jets and multijets, $< n_3 >$, for different values of M_X. 41 events are observed in the $m_{t\bar{t}}$ distribution of lepton + jets data after applying all selections. 112

7.2 Trigger efficiencies (in %) for the four lepton+jets channels 125

7.3 The multiplicative correction factors for the isolated muon to account for differences between data and Monte Carlo muon identification efficiencies. The Monte Carlo is assumed to be processed through Run Ib post-zap mu-smear package. 129

7.4 The multiplicative correction factors for the tag muon to account for differences between data and Monte Carlo muon identification efficiencies. The Monte Carlo is assumed to be processed through Run Ib post-zap mu-smear package. 130

7.5 The overall multiplicative correction factors for the identification of isolated muons and the tag muons for the different run periods. . . . 130

7.6 The break-up for the luminosity fractions for different run periods. . 131

7.7 The overall luminosity weighted relative data to Monte Carlo correction factors for the identification of isolated muons and tag muons. . 131

7.8 Total number of generated events (N_{gen}), and the number remaining (N_{sel}) in the four lepton+jets channels in different η regions for different M_X, after applying all selection criteria. 132

7.9 Acceptance A_i (in %) for the four lepton+jets channels for different M_X. 136

7.10 Integrated luminosity for the four lepton+jets channels. 140

7.11 $\sum_i A_i \mathcal{L}_i$ for different M_X, with the statistical errors and the systematic errors from various sources. 142

7.12 The 95% C.L. upper limits on $\sigma_X B$ for narrow resonances of mass M_X and natural width $\Gamma_X = 0.012 M_X$ decaying into $t\bar{t}$. The top quark mass is chosen to be 175 GeV/c^2 and flat priors are assumed for the expected sources of signal and background. 143

8.1 The systematic uncertainty on ϵ^{sel} due to the jet energy scale, the initial–state/final–state radiation, and the choice of the parton distribution functions, as well as the total error on $\sum_i A_i \mathcal{L}_i$ for different M_X. 149

8.2 The 95% C.L. upper limits on $\sigma_X B$ for narrow resonances of mass M_X and width $\Gamma_X = 0.012 M_X$ decaying into $t\bar{t}$. Error on $\sum_i A_i \mathcal{L}_i$ is included as a Gaussian function. W+jets and multijets are combined in the ratio 0.78:0.22. 152

C.1 The Monte Carlo electron identification efficiency, ϵ^{e-ID}(MC), for different M_X and for Standard Model (SM) $t\bar{t}$ production in the CC and EC. The errors shown are statistical. 161

D.1 $t\bar{t}$ branching fractions can be read off from the table which displays the W^+W^- decay branching fractions, and the resulting $t\bar{t}$ final state combinations. It can be seen that the total branching fraction for $t\bar{t}$ to lepton plus jets is 36/81 and to dileptons is 9/81. 166

D.2 Branching fractions for $t\bar{t}$ decay with leptons in the final state under unconstrained and constrained decay modes for the W bosons. . . . 166

D.3 The correction factor N_{gen}/N'_{gen} determined using Pythia for different values of M_X. 168

E.1 The 95% C.L. upper limits on $\sigma_X B$ for narrow resonances of mass M_X and width $\Gamma_X = 0.012 M_X$ decaying into $t\bar{t}$. 176

F.1 The 95% CL upper limits on $\sigma_X B$ with Gaussian priors for backgrounds. The effect of errors on $\mathcal{AL}$ is included. 179

Synopsis

0.1 Introduction

The Standard Model ($SU(3)_C \times SU(2)_L \times U(1)_Y$) gives a very satisfactory account of the interaction of the gauge bosons with the fundamental fermions, and accomodates their masses by the mechanism of Yukawa couplings to a postulated Higgs boson, but it does not give a dynamical explanation for the origin of masses.

In the 1990's, a new model called the topcolor-assisted technicolor (TC2) [1] was proposed by Hill to provide a dynamical explanation for electroweak symmetry breaking and flavor symmetry breaking, thereby giving masses to the weak gauge bosons and the fermions. In TC2, the technicolor[2] interactions at the electroweak scale can cause electroweak symmetry breaking, and extended technicolor along with walking technicolor can generate the hard masses of all fermions *except* that of the top quark. The strong topcolor [3] interactions, broken near 1 TeV, can induce a massive dynamical $t\bar{t}$ condensate and all but a few GeV of the top mass, but contribute little to electroweak symmetry breaking.

At present, direct searches for heavy $t\bar{t}$ resonances (X) are possible only at the Tevatron, the 1.8 TeV $p\bar{p}$ collider located at the Fermi National Accelerator Laboratory. Experiments seek an excess, beyond that predicted by the Standard Model, in the distribution of the invariant mass of the $t\bar{t}$ decay products. Previous

searches from the Tevatron have limited a leptophobic X to mass higher than 480 GeV/c^2 [4]. In the present analysis we describe a direct search for $t\bar{t}$ narrow, heavy resonances, X, in the inclusive decay modes $t\bar{t} \rightarrow \ell\,\nu + 4$ (or more) jets, where ℓ = e or μ, using $\sim$130 pb^{-1} of data recorded from 1992 to 1996 by the DØ experiment at the Tevatron. Seeing no significant deviation from Standard Model prediction, we present model-independent 95% confidence level upper limits on $\sigma_X B(X \rightarrow t\bar{t})$. We also present a lower limit on the $t\bar{t}$ resonance mass M_X for a particular topcolor-assisted technicolor model [5].

0.2 The DØ Detector

The DØ detector is a multi-purpose particle detector with its design optimized to have good electron and muon identification capabilities, and to measure jets and $\not\!\!E_T$ with good resolution. The detector consists of three major systems : a non-magnetic central tracking system, a hermetic uranium liquid-argon calorimeter and a muon spectrometer. Neutrinos are inferred from an imbalance in the total detected momentum perpendicular to the $p\bar{p}$ beam. A detailed description of the DØ detector can be found in Ref. [6].

0.3 Data Sample

In the $t\bar{t} \rightarrow W^+b\ W^-\bar{b}$ decay, we consider the final state in which one W boson decays hadronically while the other W boson decays to an electron or a muon and its associated neutrino (lepton+jets events). Due to the large top quark mass, the signature for such an event is a high-p_T isolated lepton (e or μ), large missing transverse energy ($\not\!\!E_T$) due to the undetected neutrino, and at least four jets. We may have additional soft muons (μ tags) arising mainly from b and c quark

semileptonic decays. We thus consider two orthogonal classes of events [7] for this analysis, whose selection is respectively based on: a) a purely topological selection of lepton+jets events which we denote as $e + jets$ and $\mu + jets$, and b) a selection based primarily on the presence of a non-isolated muon (μ tag) but also makes some cuts on the topology of the event. These events are denoted as $e + jets/\mu$ and $\mu + jets/\mu$.

The present search builds upon the techniques developed for the measurement of the top quark mass at DØ. Details of the trigger requirements, reconstruction of events and identification of the final state particles in the lepton+jets channel can be found in Ref. [7, 8]. The principal sources of background with lepton+jets final state are due to (a) Standard Model $t\bar{t}$ production, (b) production of a W boson in association with the requisite number of jets with the W boson decaying into a lepton and its corresponding neutrino, and (c) production of multijets ($N_j \sim 5$), in which one of the jets is misidentified as a lepton, and instrumental effects simulate sufficient $\not\!\!E_T$ that satisfies the neutrino requirement. For the measurement of the top quark mass most selections were optimized to reduce the contribution from non-$t\bar{t}$ sources. We therefore use similar selections in the present analysis also and these are summarized in Table 1.

0.4 Monte Carlo Signal and Backgrounds

The resonance signal $X \to t\bar{t}$ is modeled using the Pythia-6.1 [9] Monte Carlo event generator with $m_t = 175$ GeV/c^2 and CTEQ3M [10] parton distribution functions. Initial and final state radiation (ISR/FSR) are included. About 10000 events at nine different resonance masses M_X between 400-1000 GeV/c^2 are generated,

Table 1: Summary of event selections

	e+jets	μ+jets	e+jets/μ	μ+jets/μ
Lepton (l)	E_T >20 GeV $\|\eta\|$ <2	p_T >20 GeV/c $\|\eta\|$ <1.7	E_T >20 GeV $\|\eta\|$ <2	p_T >20 GeV/c $\|\eta\|$ <1.7
$\not\!\!E_T$	$\not\!\!E_T$ >20 GeV $\not\!\!E_T^{cal}$ >25 GeV	$\not\!\!E_T$ >20 GeV $\not\!\!E_T^{cal}$ >20 GeV	$\not\!\!E_T$ >20 GeV	$\not\!\!E_T$ >20 GeV $\not\!\!E_T^{cal}$ >20 GeV
Jets	$\geq$ 4 jets E_T >15 GeV $\|\eta\|$ <2	$\geq$ 4 jets E_T >15 GeV $\|\eta\|$ <2	$\geq$ 4 jets E_T >15 GeV $\|\eta\|$ <2	$\geq$ 4 jets E_T >15 GeV $\|\eta\|$ <2
μ tag	No	No	Yes	Yes
Other	$\|\not\!\!E_T\| + \|E_T^l\|$ >60 GeV $\|\eta^W\|$ <2	$\|\not\!\!E_T\| + \|E_T^l\|$ >60 GeV $\|\eta^W\|$ <2	$\not\!\!E_T$ >35 GeV if $\Delta\phi(\not\!\!E_T, \mu) < 25°$	$\Delta\phi(\not\!\!E_T, \mu) < 170°$, $\frac{\|\Delta\phi(\not\!\!E_T,\mu) - 90°\|}{90°}$ $< \frac{\not\!\!E_T}{45GeV}$
Events passing above criteria	42	41	4	3

using a width $\Gamma_X = 0.012 M_X$[1]. The generated events are processed through the DØGEANT detector simulation package [11] and reconstructed using the DØ event reconstruction program. A standard set of corrections is applied to electromagnetic objects and jets [7].

The backgrounds are estimated from a combination of Monte Carlo simulations and collider data [7]. The selections summarized in Table 1 are also applied to the Monte Carlo signal and background samples.

[1]This width is significantly smaller than the mass resolution of the DØ detector for $t\bar{t}$ systems which is estimated to be ≈4% of M_X. Hence, the results we obtain will be dominated by the detector resolution and will be independent of the choice of Γ_X.

0.5 Kinematic Fitting

For every event in data, Monte Carlo signal and background, we apply a three constraint (3C) kinematic fit to the $t\bar{t} \to (l\nu b)(q\bar{q}\bar{b})$ hypothesis by minimizing a $\chi^2 = (\mathbf{x} - \mathbf{x}^m)^T \mathbf{G}(\mathbf{x} - \mathbf{x}^m)$, where $\mathbf{x}^m(\mathbf{x})$ is the vector of measured (fit) variables and $\mathbf{G}^{-1}$ is its error matrix [7]. The two reconstructed W boson masses are constrained to equal the W boson pole mass M_W and the reconstructed t and $\bar{t}$ quark masses are equated to $m_t = 173.3$ GeV/c^2 [7]. Only ≥ 4 highest E_T jets are used in the mass fit. All other jets are assumed to be due to initial state radiation. There are 6 (12) possible assignments of these jets to quarks in events with (without) a μ tag, each having two solutions to the ν longitudinal momentum, p_z^ν. For every possible permutation, we apply additional parton-level and η-dependent jet corrections [7] if $40 < \mathrm{m}(q\bar{q}) < 140$ GeV/c^2, where $\mathrm{m}(q\bar{q})$ is the reconstructed mass of the hadronically decaying W boson. All permutations passing the $\mathrm{m}(q\bar{q})$ cut are tried and the fitted variables in the matrix $\mathbf{x}$ with the lowest χ^2 are used to reconstruct the invariant mass $m_{t\bar{t}}$ of the $t\bar{t}$ system. It has been seen that the jet permutation with the lowest χ^2 is the correct choice for ≈20% of Monte Carlo top events [7]. We apply a χ^2<10 cut to further reduce non-$t\bar{t}$ background whereupon 41 events are left in the data sample of which 4 are μ-tagged.

0.6 Bayesian Fit

For each generated M_X sample, we use Bayesian statistics [14] to determine the number of events expected from the Monte Carlo signal and the background sources in the observed lepton+jets data sample. We fit the data $m_{t\bar{t}}$ distribution

to a three-source model comprising signal ($X \to t\bar{t}$) and backgrounds due to Standard Model $t\bar{t}$ production as well as W+jets and multijets[2]. We assign a likelihood L that assumes Poisson statistics for all samples and define the posterior probability $P(n_1, n_2, n_3, K|D)$ for getting n_1, n_2 and n_3 events from the three sources respectively, under the model K, given the observed data set D as:

$$P(n_1, n_2, n_3, K|D) = \frac{L(D|n_1, n_2, n_3, K) w(n_1, n_2, n_3|K)}{\mathcal{N}'}, \tag{1}$$

where $\mathcal{N}'$ is the normalization constant which is obtained by requiring:

$$\int P(n_1, n_2, n_3, K|D) dn_1 dn_2 dn_3 = 1. \tag{2}$$

The different models K correspond to the choice of different masses M_X. Bayesian integration [14] over possible true signal and background populations in each bin i yields the likelihood $L(D|n_1, n_2, n_3, K)$:

$$\begin{aligned} L(D|n_1, n_2, n_3, K) &= \prod_{i=1}^{M} \sum_{k_1,k_2,k_3=0}^{D_i} \prod_{j=1}^{3} \binom{A_{ji} + k_j}{k_j} \\ &\quad \times \frac{p_j^{k_j}}{(1+p_j)^{A_{ji}+k_j+1}}, \end{aligned} \tag{3}$$

where D_i (A_{ji}) is the actual number of events in bin i for data (Monte Carlo source j); the indices k_j satisfy the multinomial constraint $\sum_{j=1}^{3} k_j = D_i$; $p_j = n_j/(M + \sum_{i=1}^{M} A_{ji})$, with j = 1,2,3, is an estimate of the strength of the j^{th} source; M is the number of bins used; and $w(n_1, n_2, n_3|K)$ denotes the joint prior probability for the three source strengths. We assume *flat* priors for each of the three sources. The expected number of counts in the data from any source j can then be obtained as $< n_j >$:

[2]We fix the ratio of W+jets and multijets background to 0.78:0.22 [7]

$$< n_j >= \int\int\int n_j P(n_1, n_2, n_3, K|D) dn_1 dn_2 dn_3. \quad (4)$$

The normalized counts obtained for the signal ($< n_1 >$) and the two background sources ($< n_2 >$, $< n_3 >$) are listed in Table 2 for a few resonance masses M_X. The data $m_{t\bar{t}}$ distribution and the corresponding distributions from the three Monte Carlo sources normalized to $< n_1 >$, $< n_2 >$ and $< n_3 >$ respectively, for M_X = 600 GeV/c^2, are shown in Figure 1. We see no statistically significant evidence of any signal beyond Standard Model expectations in the data $m_{t\bar{t}}$ distribution. Similar agreement between Standard Model prediction and observed data distribution is seen for the other resonance masses as well. We thus proceed to set upper limits on the production cross section of X (σ_X) times its branching fraction (B) to $t\bar{t}$.

Table 2: The expected numbers of signal ($X \to t\bar{t}$) counts $< n_1 >$ and background counts from Standard Model $t\bar{t}$ production $< n_2 >$ and from W+jets and multijets $< n_3 >$ for different M_X. 41 events are observed in the $m_{t\bar{t}}$ distribution of l + jets data after applying the precuts and the $\chi^2 < 10$ cut.

M_X (GeV/c^2)	$< n_1 >$	$< n_2 >$	$< n_3 >$	Background $< n_2 >+< n_3 >$
400	9.0±7.0	20.5±10.8	13.9±10.2	34.4±14.9
500	4.9±4.2	22.2±11.5	15.3±10.5	37.5±15.6
600	4.2±3.2	23.7±11.6	15.4±10.6	39.0±15.7
750	1.6±1.6	26.8±11.7	12.6±9.9	39.4±15.3
850	$1.4^{+1.5}_{-1.4}$	26.9±11.7	12.5±9.8	39.4±15.3

0.7 Upper Limits on $\sigma_X B(X \to t\bar{t})$

We express $n_1 = \mathcal{A}\mathcal{L}\sigma_X B$ in Eq. (1), where $\mathcal{A}$ is the acceptance for $X \to t\bar{t}$ events and $\mathcal{L}$ is the integrated luminosity for data. We then integrate Eq. (1) over n_2 and n_3, and define the upper limits on $\sigma_X B$ at 95% confidence level as:

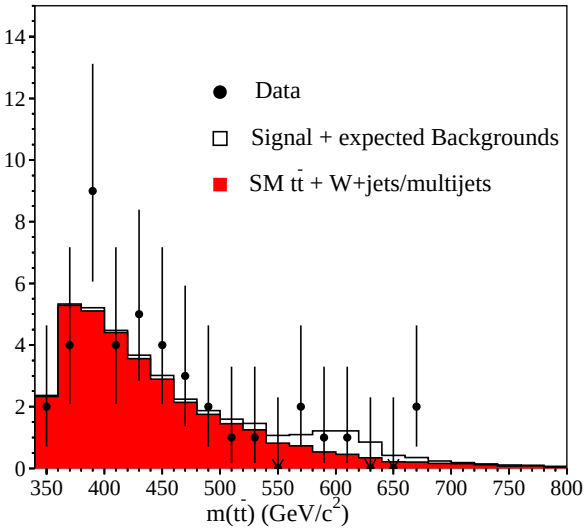

Figure 1: Normalized distributions of $m_{t\bar{t}}$ for sum of all Standard Model backgrounds (shaded) and sum of signal ($X \rightarrow t\bar{t}$) and Standard Model backgrounds (unshaded) for $M_X = 600$ GeV/c^2. The data $m_{t\bar{t}}$ distribution is shown by dots.

$$\int_0^{(\sigma_X B)_{95}} P(\sigma_X B, K|D) d(\sigma_X B) = 0.95 \tag{5}$$

for every M_X.

0.8 Effect of Experimental Uncertainties and Results

The expected shapes of the background and data $m_{t\bar{t}}$ distributions and the signal acceptance rate are subject to several sources of systematic uncertainty. We investigate the uncertainties in the signal acceptance with respect to the jet E_T scale, ISR/FSR, and the choice of parton distribution functions. The uncertainty due to jet energy scale is estimated by scaling the jet energies by $\pm$(2.5%+0.5 GeV) [7]

before applying any selection. For ISR/FSR, we compare the signal acceptance with and without ISR/FSR (in Pythia). We also compare the signal acceptance for the two parton distribution sets of CTEQ3M and GRV94L. The total error for signal acceptance times the integrated luminosity ($\mathcal{AL}$) due to the above sources of uncertainties and including the statistical uncertainties and uncertainties in the trigger efficiency, e/μ identification, and the effective integrated luminosity is 23.8 % for $M_X = 600$ GeV/c^2.

For each M_X we convolute the posterior probability density $P(\sigma_X B, K|D)$ with a Gaussian prior for $\mathcal{AL}$, with the estimated value of $\mathcal{AL}$ as the mean of the Gaussian and its error as one standard deviation from the mean. The upper limits on $\sigma_X B$ at 95% confidence obtained using Eq. (5) and integrating over all possible values of $\mathcal{AL}$, are listed in Table 3. We also use our limits to constrain a model of topcolor assisted technicolor and exclude the existence of a leptophobic X with mass M_X <560 GeV/c^2 for a natural width $\Gamma_X = 0.012 M_X$ as shown in Figure 2.

Table 3: The 95% C.L. upper limits on $\sigma_X \times B(X \rightarrow\ tt)$ for narrow resonances of mass M_X and natural width $\Gamma_X = 0.012 M_X$ decaying into $t\bar{t}$.

M_X (GeV/c^2)	95% C.L. upper limits on $\sigma_X \times$ B(X $\rightarrow t\bar{t}$) (pb)
400.	5.0
450	4.5
500	2.7
550	2.3
600	2.3
650	2.0
750	1.3
850	1.5
1000	2.0

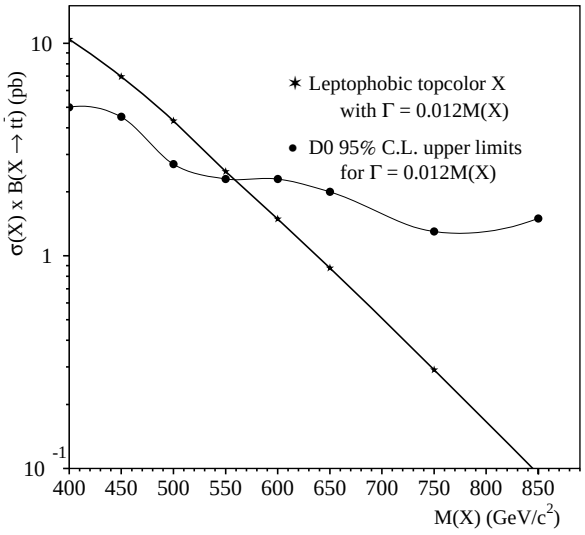

Figure 2: The DØ Run I 95% confidence level upper limits on $\sigma_X B$ as a function of resonance mass M_X. Included for reference are the predicted topcolor assisted technicolor cross sections for a width $\Gamma_X = 1.2\%\ M_X$.

0.9 Conclusion

In conclusion, after analysing 130 pb^{-1} of data, we find no evidence for $t\bar{t}$ resonance and so establish upper limits on $\sigma_X B(X \to t\bar{t})$ at 95% confidence for M_X between 400 and 1000 GeV/c^2. We also exclude at 95% confidence level, the existence of a leptophobic X with mass M_X <560 GeV/c^2 for a width $\Gamma_X = 0.012 M_X$.

Bibliography

[1] C. T. Hill, Phys. Lett. **B345**, 483 (1995).

[2] S. Weinberg, Phys. Rev. **D13**, 974 (1976); L. Susskind, Phys. Rev. **D20**, 2619 (1979); S. Dimopoulos, L. Susskind, Nucl. Phys. **B155**, 237 (1979); E. Eichten, K. Lane, Phys. Lett. **B90**, 125 (1980).

[3] C. T. Hill, Phys. Lett. **B266**, 419 (1991); S. P. Martin, Phys. Rev. **D45**, 4283 (1992), *ibid* **D46**, 2197 (1992); Nucl. Phys. **B398**, 359 (1993).

[4] CDF Collaboration, T. Affolder *et al.*, Phys. Rev. Lett. **85** , 2062 (2000).

[5] R. M. Harris, C. T. Hill and S. Parke, Cross section for Topcolor Z'_t decaying to $t\bar{t}$, arXiv:hep-ph/9911288 (1999).

[6] DØ Collaboration, S. Abachi *et al.*, Nucl. Instrum. Methods Phys. Res., Sect. A **338** , 185 (1994).

[7] DØ Collaboration, B. Abbott *et al.*, Phys. Rev. **D58**, 4769 (1999).

[8] DØ Collaboration, V.M. Abazov *et al.*, *$t\bar{t}$ Production Cross Section in $p\bar{p}$ collisions at $\sqrt{s}$ = 1.8 TeV* , (submitted to Phys. Rev. D).

[9] T. Sjøstrand, Comput. Phys. Commun. **82**, 74 (1994).

[10] H. L. Lai, *et al.*, Phys. Rev. **D51** , 4763 (1995).

[11] DØ Collaboration, J. Womersley, in *Proceedings of the XXVI International Conference on High Energy Physics, Dallas, Texas,* edited by J. R. Sanford (AIP, New York, 1993), p.1800.

[12] G. Marchesini, *et al.*, Comp. Phys. Comm. **67**, 465 (1992).

[13] F. A. Berends, H. Kuijf, B. Tausk and W. T. Giele, Nucl. Phys. B **357** , 32 (1991).

[14] P. C. Bhat, H. B. Prosper, and S. Snyder, Phys. Lett. **B407** , 73 (1997).

List of Publications

• In Proceedings

– "*Search for Narrow-Width $t\bar{t}$ Resonances in $p\bar{p}$ collisions at $\sqrt{s}$ = 1.8 TeV*", V. M. Abazov *et al.*, (DØ Collaboration), hep-ex/0302037; submitted for the proceedings of

* $XXXI$ **International Conference on High Energy Physics (ICHEP 2002)**, Amsterdam, The Netherlands, 24-31 Jul., 2002
* V^{th} **International Conference on Quark Confinement and Hadron Spectrum**, Italy, 10-14 Sep., 2002
* IX^{th} **International Symposium on Particles, Strings and Cosmology (PASCOS '03)**, TIFR, India, 3-8 Jan., 2003

• In Journals

– "*Search for Narrow-Width $t\bar{t}$ Resonances in $p\bar{p}$ collisions at $\sqrt{s}$ = 1.8 TeV*", V. M. Abazov *et al.*, (DØ Collaboration), to be submitted to **Phys. Rev. Lett.**

Acknowledgments

I would like to thank my advisor, Naba Mondal, for the insight and knowledge that he has given me, and for the kind understanding that he has shown towards me, during the past six years. I express my sincere gratitude to him for his constant encouragement and support which helped me overcome many difficulties I faced in my research career. I find it difficult to imagine a better advisor !

I would also like to convey my special thanks to Prof. V.S. Narasimham for always patiently listening to my doubts and questions and helping me understand various aspects of particle physics; to B.S.Acharya, M.R.Krishnaswamy, Sunand Banerjee, Sudeshna Banerjee, and Shashi Dugad for fruitful discussions on several occasions.

I would also like to thank everyone who has helped me in achieving the completion of this work especially Dhiman Chakraborty, Scott Snyder, Brian Connolly, Veronica Sorin, and Andrew Green, who have assisted me at various stages of data analysis and Monte Carlo simulations.

I extend my appreciation to the non-author members of the editorial board (Ken, Elemer, Drew, Sherry, Tom Diehl) and to Ela, Cecilia, Tom Ferbel, and Paul Grannis, for their corrections and ideas to improve this work, and to John Hobbs, Harrison Prosper, and Pushpa Bhat for helping me understand various details regarding Run I data, as well as the Bayesian approach to analyze the data. Sreerup,

Uma Mahanta, Sridhar, and D.P.Roy for the knowledge they imparted to me on various theoretical aspects of particle physics.

I also appreciate the help provided by members of the scientific section of our group at TIFR, Sathyanarayana, Nagaraj, Reddy, and Kalmani on various occasions during the past five years, and wish to express my heart felt gratitude to them.

I acknowledge the help and co-operation of the members of the office of Department of High Energy Physics, my seniors Shanker, Ambreesh and Satyaki, and friends Tania, Nirmalya, Prolay, Avdhesh, Jyothsna, Subhendu, Piyali, Kavita, Amisha, Arati, Punita, Seema Dhamija, Garima, Krithika, Mihaela, Usha, Florencia, and Srilatha, for their love, understanding, and support during these five years.

It is my pleasure to acknowledge the excellent facilities and research environment provided by TIFR. I am also happy to acknowledge the Kanwal Rekhi Scholarship of the TIFR Endowment Fund.

I would also like to convey my special thanks to my physics teachers Shyamali Biswas and Rita Chandra, who instilled in me an interest in physics in school, and then in college. Special thanks are also due to Amitabha Mukherjee, Shobhit Mahajan, and Shekhar Mishra for their constant encouragement to march ahead despite all odds.

My sincerest thanks are also due to my friends in the Soka Gakkai (Pat, Gerry, Oko, Ariana, and Fransisca), and to my mentor in life, Dr Daisaku Ikeda, from whom I am striving to learn to live as a global citizen.

Finally, I would like to express profound thanks to my parents, who have struggled tirelessly to provide a secure home and the best possible education, and to all my family members for their love and encouragement that has spurred me on.

Chapter 1

Introduction

With the discovery of the top quark by the DØ and CDF collaborations, and the subsequent measurement of its mass and production cross section, we now turn towards investigating the top-antitop invariant mass distribution for evidence of any new physics beyond the Standard Model. This thesis presents a detailed account of the search for a new vector gauge boson, X, decaying to $t\bar{t}$ pairs.

The general plan is as follows. The Standard Model, its major shortfalls, and aspects of some models beyond the Standard Model, will be discussed in this chapter. In chapter 2 the experimental apparatus used for this study, the DØ detector, will be described in detail. In chapter 3 the algorithms used to identify final-state objects such as leptons and jets, will be described. The principal sources of background and event selection will be discussed in chapter 4. In chapters 5 and 6, we present the kinematic fitting of the $t\bar{t}$ invariant mass distribution, and the simulation of $X \to t\bar{t}$ events. The analysis of data using Bayesian statistics, and the systematic uncertainties and results will be

discussed in chapters 7 and 8 respectively. In chapter 9, we will summarize the results and discuss future prospects.

Some extra studies performed, and more detailed information pertaining to this analysis, will be discussed in the appendices.

1.1 A Brief Tour of the Standard Model

The Standard Model (SM) of particle physics is a quantum field theory that describes how the known particles interact via three of the four forces in nature: electromagnetism, weak and strong forces, at very small distance scales ($\approx 10^{-15}$ m). It is not currently known how to include the fourth force, gravitational interaction, to obtain a single field theory, but since gravity is so much weaker than the other three forces for distances $\sim 10^{-15}$ m, it is completely ignorable in almost all experiments of interest in high-energy physics.

In Table 1.1, we list the particle types of the Standard Model. These can be divided into three major groups: quarks, leptons and gauge bosons. The quarks and leptons are all spin-$\frac{1}{2}$ particles and are grouped into three *generations* of two particles each. Each particle has an associated antiparticle with the same mass but opposite quantum numbers. The corresponding particles in each generation have similar properties, except for their masses, which increase with each successive generation. All 'normal' matter (protons, neutrons and electrons) is composed of particles from the first generation. Particles in

	symbol	name	mass (MeV/c^2)	charge (e)
Quarks	d	down	≈ 8	$-1/3$
(spin = 1/2)	u	up	≈ 4	2/3
	s	strange	≈ 150	$-1/3$
	c	charm	≈ 1400	2/3
	b	bottom	≈ 4500	$-1/3$
	t	top	≈ 175 GeV/c^2	2/3
Leptons	e	electron	0.511	-1
(spin=1/2)	ν_e	electron neutrino	< 3 eV/c^2	0
	μ	muon	105.7	-1
	ν_μ	muon neutrino	< 0.19	0
	τ	tau	1777	-1
	ν_τ	tau neutrino	< 18.2	0
Gauge bosons	γ	photon	0	0
(spin = 1)	W	W	80.4 GeV/c^2	1
	Z	Z	91.2 GeV/c^2	0
	g	gluon	0	0
Higgs	H[a]	Higgs	?	?

Table 1.1: Particles of the Standard Model [1].

[a]Not yet observed.

higher generations can be produced in high-energy interactions, through man-made accelerators or when cosmic rays hit the upper atmosphere, but they are unstable and ultimately decay into first generation particles or photons.

Each generation of leptons consists of one charged particle (the electron, muon and tau) and an associated neutral particle (the neutrinos). Experimentally, masses of the neutrinos are constrained to be quite small; the Standard Model assumes that they are zero. The charged leptons can exhibit electromagnetic and weak interactions, but the neutrinos are affected only by the weak interaction. This makes the direct detection of neutrinos very difficult, but their presence can be inferred from an imbalance in the total measured momentum.

The quarks have fractional electric charge — either 1/3 or 2/3 the charge of an electron, and are affected by the strong force also, which binds them together inside nuclei, and is described in more detail below.

The gauge bosons are spin-1 particles, and act as mediators of the electromagnetic, weak and strong forces.

Electromagnetism ('quantum electrodynamics' or 'QED'), for example, is mediated by the photon, which couples to particles with electric charge. The coupling strength in this case is not constant: it increases with the energy involved in the interaction.

The weak interaction is mediated by the W and Z bosons. Unlike the photon which is massless, the W and Z bosons are quite heavy, thereby implying that the weak force has a short range. One of the major features of the Standard Model is the fact that it treats the weak force and electromagnetism

in a unified manner as the 'electroweak' force.

The strong force ('quantum chromodynamics' or 'QCD') is mediated by gluons. Gluons couple to objects which possess 'color' charge, which are the quarks and the gluons themselves. A color charge has three possible values, conventionally called 'red', 'green' and 'blue' for quarks; antiquarks come in 'anti-red', 'anti-green' and 'anti-blue' colors. However, as the energy of interaction increases, the strength of the strong coupling gets smaller. Therefore at the high energies typical of modern high-energy experiments ($E \geq 10$ GeV), quarks behave nearly like free particles ('*asymptotic freedom*'), and the behaviour of the strong force can be calculated using the same sort of perturbative techniques as are used for electromagnetism. However, at lower energies (such as would be typical of quarks bound in a nucleon) the coupling strength becomes large enough that perturbation theory breaks down. The behaviour of such systems is presently not calculable from first principles.

The fact that the strength of this interaction increases as the energy of the interaction decreases, or equivalently, as the distance scale of the interaction increases, also ensures that at distance scales larger than a nucleon, quarks always appear in bound states, a phenomenon known as *quark confinement*. It is thought that these bound states (called hadrons) are always formed so that the color charges cancel exactly (either a quark and its antiquark with the opposite color, or a mixture of all three colors) and the total electric charge is integral.

In order to pull a quark out of a bound state such as a nucleon, one must expend sufficient energy to create a new quark-antiquark pair, one of which

will pair with the removed quark, and the other one will take the place of the removed quark. This means that if a quark is produced or knocked out of a nucleus in some interaction, it will rapidly 'clothe' itself with other quarks which bind together to form a collection of composite particles[1]. Experimentally, what one 'sees' is not a single quark or gluon, but a collimated *jet* of many hadrons moving along directions close to that of the original quark.

The remaining ingredient of the Standard Model is the Higgs boson. The standard method of introducing a new interaction into models like the Standard Model (by demanding a gauge symmetry) requires that the associated gauge bosons be massless. Therefore the Higgs mechanism was introduced in which a new scalar particle interacts with the W and Z bosons in order to give them their masses. The quarks and leptons can also acquire masses through this mechanism. If this description is correct, the Higgs should appear as a real, observable particle. To date, however, it has not been observed.

1.2 Production and Decay of $t\bar{t}$ pairs in Standard Model

In the Standard Model, the production of $t\bar{t}$ pairs proceeds via the strong interactions in $q\bar{q}$ annihilation and gluon fusion, depicted in Figure 1.1. At a center of mass energy, $\sqrt{s} = 1.8$ TeV, however, the $t\bar{t}$ cross section for production via $q\bar{q}$ annihilation is dominant by a factor of ≈ 5 since the gg

[1]This process is usually called '*fragmentation* and *hadronization*'.

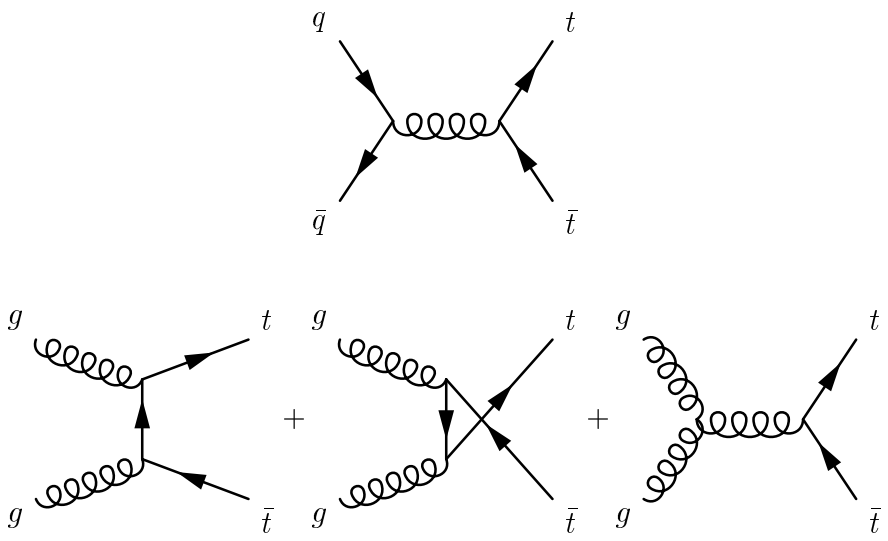

Figure 1.1: Lowest order $t\bar{t}$ production processes.

interactions at this energy rarely contain enough energy to produce a $t\bar{t}$ pair.

Within the Standard Model, a top quark will almost always decay into a (real) W boson and a b quark [2]. The b quark from the top quark decay will form a jet, while the W boson will decay into either a lepton-neutrino pair or a quark-antiquark pair. To a good approximation, each possible final state of the W is equally probable; however, one must remember to count each quark flavor three times, since quarks come in three colors. Thus, the probability for the W boson to decay into each of the three lepton flavors is about 1/9, and the probability for it to decay into each of the two available quark final states is about 1/3.

With two top quarks in each event, each decaying into a W boson and a b quark, the events may be classified based on how the W bosons decay as (see

	$W \to e\nu_e$ (1/9)	$W \to \mu\nu_\mu$ (1/9)	$W \to \tau\nu_\tau$ (1/9)	$W \to q\bar{q}$ (2/3)
$W \to e\nu_e$ (1/9)	1/81	1/81	1/81	2/27
$W \to \mu\nu_\mu$ (1/9)	1/81	1/81	1/81	2/27
$W \to \tau\nu_\tau$ (1/9)	1/81	1/81	1/81	2/27
$W \to q\bar{q}$ (2/3)	2/27	2/27	2/27	4/9

Table 1.2: Possible decay modes for a $t\bar{t}$ pair.

Table 1.2):

- Events in which both the W bosons decay leptonically are called *dilepton* events. These final states are expected to have small backgrounds (especially when the lepton is an electron or a muon[2]). However, as can be seen from Table 1.2, they also have a rather small branching ratio, with the electron and the muon channels comprising only $4/81 \approx 4.9\%$ of $t\bar{t}$ decays.

- Events in which both the W bosons decay into $q\bar{q}$ pairs are called *all-jets* events. This channel boasts the largest branching ratio of about 44%. Unfortunately, it is dominated by a huge background from QCD multijet processes.

- Events in which one W boson decays leptonically and the other decays into quarks are called *semileptonic* or *lepton + jets* events. Compared to the dilepton channels, the lepton + jets channels have a much larger

[2]In case of tau leptons there is a huge background from QCD jets in a $p\bar{p}$ collision; since the tau leptons leave a signature similar to jets in the detector, it is difficult to identify them efficiently.

Quantity	Number of parameters
Quark masses	6
e, μ, τ masses	3
Coupling constants	3
Independent parameters of CKM matrix	3
Magnitude of CP violation	1
Fundamental electroweak mass scale	1
Higgs mass	1

Table 1.3: The 18 independent parameters of the Standard Model.

cross section — the branching ratio for each lepton + jets channel is $4/27 \approx 15\%$. Requiring a leptonically decaying W boson also reduces the amount of background present in the *all-jets* channel.

1.3 Beyond the Standard Model

The aim of particle physics is to focus on efforts to understand at a more basic level the laws which govern fundamental interactions. The Standard Model has been a great achievement in particle physics. A large number of experimental results have confirmed nearly every feature of the theory to a high degree of precision. However, it is by no means the ultimate theory because it leaves many questions and problems unanswered [3]. A few notable ones are listed.

First of all, the Standard Model requires 18 independent free parameters (listed in Table 1.3) which cannot be calculated theoretically, but must be determined through experiment. The existence of a large number of free parameters strongly suggests that the theory is far from being complete.

Secondly, the Higgs mechanism that is responsible for the spontaneous electroweak symmetry breaking (EWSB), was introduced in an *ad hoc* way into the theory. No first principle tells us why the potential for the scalar Higgs field (ϕ) should be written as:

$$V(\phi) \;=\; \mu^2\phi^\dagger\phi \;+\; \lambda(\phi^\dagger\phi)^2 \tag{1.1}$$

with $\mu^2 < 0$ and $\lambda > 0$.

Thirdly, in the Standard Model, the Higgs self-interaction through fermion loops [4] leads to quadratic divergence of the Higgs mass. The Higgs mass m_H^2 $= -2\mu^2 + 2\Lambda^2$, requires a cut-off Λ at which new physics occurs. If the Standard Model is considered to include gravity as well, the most natural choice for the cut-off Λ would be the Planck scale, *i.e.* $\Lambda \sim 10^{19}$ GeV. Therefore in order to get a physical Higgs mass of, say, order 1 TeV, we must ensure cancellation of the divergence ($2\Lambda^2$) to a fantastic precision of 1 part in 10^{32}. This implies an excessive *fine-tuning* of parameters which is not very natural.

Therefore, it is thought that the Standard Model, as it stands, is likely to represent the low-energy limit of a more global symmetry which might serve to explain electroweak symmetry breaking and the number of fermion generations observed, as well as predict the values of the parameters listed in Table 1.3. One such potential candidate is called 'supersymmetry' [5], which extends the

symmetry of space-time with the introduction of several additional quantum mechanical dimensions. It solves the fine-tuning problem in an elegant way by introducing a supersymmetric particle (sparticle) corresponding to each Standard Model particle with spin differing by 1/2 and all other quantum numbers remaining the same. The radiative corrections to the Higgs mass involving loop diagrams of fermions cancel those involving the sfermions. Supersymmetry also predicts the existence of more than one Higgs particle, but does not provide a *dynamical* explanation of electroweak and flavor symmetry breaking.

In the 1970s, the 'technicolor' model [6] was proposed to provide a dynamical explanation of electroweak and flavor symmetry breaking. It provides a mechanism for imparting mass to the W and Z bosons, by introducing a new strong force which is analogous to the strong color force. In this model, just like the quarks in quantum chromodynamics, a new spectrum of particles, called the techniquarks, exist, which transform according to the fundamental representation of the technicolor gauge group $\mathrm{SU(N_{TC})}$ and the usual representation of the Standard Model gauge group $\mathrm{SU(3)_C \times SU(2)_L \times U(1)_Y}$. The electroweak symmetry breaking arises from the condensation of techniquark bilinears at the technicolor scale Λ_{TC} ($\sim$ 1 TeV). The generation of realistic masses for the charged leptons and quarks seems attainable in this framework, via extended technicolor (ETC), in particular with a slowly running ("walking") coupling.

Extended technicolor (ETC) predicts the existence of massive vector gauge bosons, which, at energy scales $\Lambda_{ETC} >> \Lambda_{TC}$, can mediate interactions between fermions and technifermions and generate the fermion masses, as shown

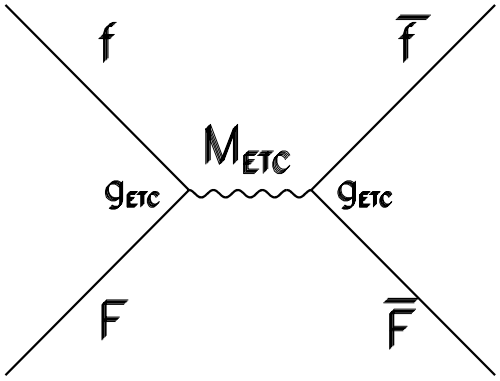

Figure 1.2: The ETC vector gauge boson of mass M_{ETC} mediating interactions between fermions (f) and technifermions (F) via the coupling g_{ETC}, at scales $\Lambda_{ETC} >> \Lambda_{TC}$.

in Figure 1.2. The mass of the ETC gauge boson (M_{ETC}) is related to the fermion mass (m_f) as:

$$m_f \approx \frac{g_{ETC}^2 \Lambda_{TC}^3}{M_{ETC}^2}, \tag{1.2}$$

where g_{ETC} is the ETC vector-fermion gauge coupling. Since the masses required for the different generations span the range from $m_e \approx 0.5$ MeV to $m_q \approx 1$ GeV (assuming all the neutrinos are massless[3]), and g_{ETC} are gauge couplings that should all be of the same order of magnitude, the only simple way

[3]For an explanation of the non-zero but small masses of the neutrinos as evident from many present day experiments, see Ref. [7].

of reproducing the required variation in masses seems to be to have a whole spectrum of the ETC vector gauge bosons with *different* masses, one for each fermion. Assuming g_{ETC} is of order unity and $\Lambda_{TC} \approx 1$ TeV, we therefore need a set of ETC gauge bosons with progressively decreasing masses, with M_{ETC} ranging from $\approx 10^3$ TeV to ≈ 30 TeV, in order to get the masses of the charged leptons and the u, d, s, c and b quarks. For the top quark ($m_t \approx$ 175 GeV), we would need $M_{ETC} \approx 1$ TeV. But since extended technicolor is valid for scales Λ_{ETC} ($\approx \frac{M_{ETC}}{g_{ETC}}$) $>>$ Λ_{TC} (~ 1 TeV), the large mass of the top quark cannot be explained by the technicolor models alone.

An alternate approach was developed in the early 90's based on a new interaction of the third generation quarks. This interaction, called topcolor, was invented as a minimal dynamical scheme to reproduce the simplicity of the one-doublet Higgs model *and* explain the very large mass of top quarks [8]. In topcolor, a large top quark condensate ($< t\bar{t} >$) is formed by new strong interactions at the energy scale Λ_t [9]. But in order that the resulting low-energy theory simulate the Standard Model, particularly its small violation of the weak isospin, the topcolor scale must be very high: $\Lambda_t \sim 10^{15}$ GeV $>> m_t$. The original topcolor scenario is therefore unnatural, requiring a fine-tuning of couplings of order one part in $\frac{\Lambda_t^2}{{m_t}^2} \approx 10^{25}$.

Since technicolor could be a natural mechanism for electroweak symmetry breaking, while topcolor dynamics most aptly explain the large top quark mass, it was proposed by Hill [10] to combine the two into what he called the topcolor assisted technicolor (TC2) model. In TC2, the technicolor interactions at the electroweak scale can cause electroweak symmetry breaking, and extended

technicolor along with walking technicolor can generate the hard masses of all fermions *except* that of the top quark. The strong topcolor interactions, now broken near 1 TeV, can induce a massive dynamical $t\bar{t}$ condensate and all but a few GeV of the top mass, but contribute little to electroweak symmetry breaking. The combination neatly removes the objections that topcolor is unnatural and that technicolor cannot generate a large top quark mass.

In the original scheme of TC2, the QCD gauge group $\mathrm{SU(3)_C}$ is embedded into a larger structure, eg., $\mathrm{SU(3)_1 \times SU(3)_2}$ with couplings h_1 and h_2 respectively. Similarly the weak hypercharge gauge group $\mathrm{U(1)_Y}$ is embedded into a larger structure, eg., $\mathrm{U(1)_1 \times U(1)_2}$. $\mathrm{SU(3)_1 \times U(1)_1}$ couples to the first and second generations and $\mathrm{SU(3)_2 \times U(1)_2}$ couples to the third generation. At a scale of order 1 TeV, $\mathrm{SU(3)_1 \times SU(3)_2 \times U(1)_1 \times U(1)_2}$ is dynamically broken to the subgroup of ordinary color and weak hypercharge $\mathrm{SU(3)_C \times U(1)_Y}$. At this energy the $\mathrm{SU(3)_2 \times U(1)_2}$ couplings are strong while the $\mathrm{SU(3)_1 \times U(1)_1}$ couplings are weak ($h_2 >> h_1$). The breaking of $\mathrm{SU(3)_1 \times SU(3)_2 \rightarrow SU(3)_C}$ gives rise to massive gauge bosons – a color octet of "colorons" V_8; the breaking of $\mathrm{U(1)_1 \times U(1)_2 \rightarrow U(1)_Y}$ gives rise to a color singlet Z'.

In the TC2 scheme, new models can also be constructed by grouping $\mathrm{U(1)_1}$ and $\mathrm{U(1)_2}$ with the three fermion generations differently [11]. For example, in Ref. [11], a model is proposed in which $\mathrm{U(1)_1}$ couples to the second generation and $\mathrm{U(1)_2}$ couples to the first and third generations. The color singlet, Z', in this model, couples preferentially to the third quark generation, and has no significant couplings to the leptons, and is, hence, called a leptophobic Z'. Further, in order to provide the large mass to the top quark, while at the same

time to ensure that the b quark is light, a 'tilting' mechanism is introduced such that the formation of the $t\bar{t}$ condensate is enhanced, while the formation of the $b\bar{b}$ condensate is blocked. Therefore, the cross section for $Z' \rightarrow t\bar{t}$, in this model, is large enough that it should be possible to observe or exclude this model, for a significant range of the Z' masses and widths, using current data from the Tevatron Collider. The evidence for the Z' decaying to $t\bar{t}$ pairs would appear as a resonance peak at the Z' mass, in the $t\bar{t}$ invariant mass distribution.

Within the framework of the Standard Model, no particle decays to a $t\bar{t}$ pair[4] and hence the observation of a resonance peak in the $t\bar{t}$ invariant mass distribution will be a direct evidence of physics beyond the Standard Model. In this thesis, we search for such a signal (any resonance X decaying to $t\bar{t}$) in the $t\bar{t}$ invariant mass spectrum using the data collected from $p\bar{p}$ collisions between 1992 and 1996, by the DØ detector at the Tevatron. Previous searches by the CDF experiment at the Tevatron have found no evidence for any deviation from Standard Model predictions, in the $t\bar{t}$ invariant mass spectrum, and have set a lower limit of 480 GeV/c^2 [12] on the mass of a leptophobic Z'.

In the present analysis, we consider the *lepton + jets* events in order to reconstruct the $t\bar{t}$ invariant mass in view of its more favorable signal to background ratio, compared to the other two $t\bar{t}$ decay modes.

[4]It is true that the Standard Model Higgs must couple to the top quark, but the expected production cross section for $H \rightarrow t\bar{t}$ at the Tevatron is negligible.

Chapter 2

Experimental Apparatus

This chapter contains a brief description of the DØ detector. The details of the detector can be found in Ref. [13].

2.1 Coordinate Systems

In what follows, a right-handed coordinate system will be used, with the positive z-axis aligned along the beam in the direction of the protons and the positive y-axis pointing up. Cylindrical (r, ϕ, z) coordinates are sometimes used, as are spherical (r, ϕ, θ) coordinates. The angular variables are defined so that $\phi = \pi/2$ is parallel to the positive y-axis, and $\theta = 0$ is coincident with the positive z-axis. Instead of θ, it is often convenient to use the pseudorapidity η defined as

$$\eta = -\ln \tan \frac{\theta}{2}. \tag{2.1}$$

The pseudorapidity approximates the true rapidity,

$$y = \frac{1}{2} \ln \frac{E + p_z}{E - p_z}, \tag{2.2}$$

in the limit that $m \ll E$ (where m is the invariant mass, $m^2 = E^2 - |\vec{p}|^2$). The distribution of events in η is invariant under a Lorentz boost along the z axis, and particle production usually scales per unit of (pseudo)rapidity. As defined by Eq. (2.1), η is called the physics pseudorapidity, and is calculated using the reconstructed (event) vertex in an interaction. Since in a $p\bar{p}$ collision at Tevatron, the event vertex does not, in general, appear at the center of the detector, another quantity called the detector pseudorapidity (η_{det}) is often used. It is defined with respect to the geometric center of the detector, instead of the event vertex.

It is also often convenient to use instead of momentum, the 'transverse' momentum, which is the momentum vector projected onto a plane perpendicular to the beam axis:

$$p_T = p \sin\theta. \tag{2.3}$$

This is particularly useful due to the fact that in a $p\bar{p}$ collision, the momenta along the beam of the colliding partons are not known (since many of the products of the collision escape down the beam pipe). However, the transverse momenta of the products escaping down the beam pipe are very small compared to their momenta along the beam, so one can safely apply momentum conservation in the transverse plane. One can also define a 'transverse energy' as:

$$E_T = E \sin\theta. \tag{2.4}$$

When treated as a vector, the direction of E_T should be taken to be the same as the p_T vector.

2.2 Luminosity and Cross Section

In beam-colliding machines, interaction rates are measured in terms of instantaneous luminosity, L, which is given by:

$$L = \frac{N_p N_{\bar{p}} B f_0}{4\pi A}, \tag{2.5}$$

in case of $p\bar{p}$ collisions. Here N_p is the total number of protons per bunch, $N_{\bar{p}}$ is the total number of antiprotons per bunch, B is the number of bunches of each type, f_0 is the frequency of bunch revolution (47.7 kHz), and A is the cross-sectional area of the bunches ($\sim 5 \times 10^{-5}\ cm^2$). The peak instantaneous luminosity at the Tevatron for Run I (1992-1996) was typically in the range 10^{30} – 10^{31} $\mathrm{cm}^{-2}\,\mathrm{s}^{-1}$. The interaction rate, R, is related to the instantaneous luminosity, L, by:

$$R = \sigma L, \tag{2.6}$$

where σ is the cross section of the particular interaction, and is a measure of the probability of its occurrence. Cross sections are often expressed in *barns*, where $1\,\mathrm{barn} = 10^{-24}\,\mathrm{cm}^2$. The number of events (N) of a specific type expected after running an experiment for a period of time is found by integrating the luminosity with respect to time:

$$N = \sigma \int L dt. \tag{2.7}$$

The quantity $\int L dt$ is called *integrated luminosity*; the total integrated luminosity for Run I was measured to be 130 pb^{-1} (chapter 4).

2.3 The Beam

The DØ detector is located at the Fermilab Tevatron, presently the world's highest-energy hadron collider, with a center-of-mass energy of 1800 GeV. A schematic of the accelerator complex is shown in Figure 2.1.

The Tevatron is a proton storage ring of radius 1000 m. The ring is filled with bunches of protons and antiprotons, which circulate in opposite directions. At the B0 and D0 experimental areas, these beams are made to collide with each other. The process of filling the ring is quite complicated; a summary of the major steps is given below.

The beams originate in the preaccelerator. There, H^- ions are formed and accelerated to 750 keV by an electrostatic Cockroft-Walton accelerator. The preaccelerator operates in a pulsed mode with a frequency of 15 Hz. The ions are bunched and transported to the start of the Linac. The Linac is a 150 m long linear accelerator, which boosts the energy of the ions to 400 MeV. After emerging from the Linac, the ions are passed through a carbon foil which strips off the electrons, leaving bare protons. The protons are then injected into the Booster, a 151 m diameter synchrotron. (A synchrotron is a device which confines charged particles in a closed orbit using bending magnets. RF cavities can be used to increase the energy of the stored particles; when this is done, the field of the bending magnets must also be increased in a synchronous manner in order to keep the particles in the same orbit.) The Booster accelerates the protons to an energy of 8 GeV. The protons are then injected into the Main Ring, a large (1000 m radius) synchrotron composed of conventional magnets.

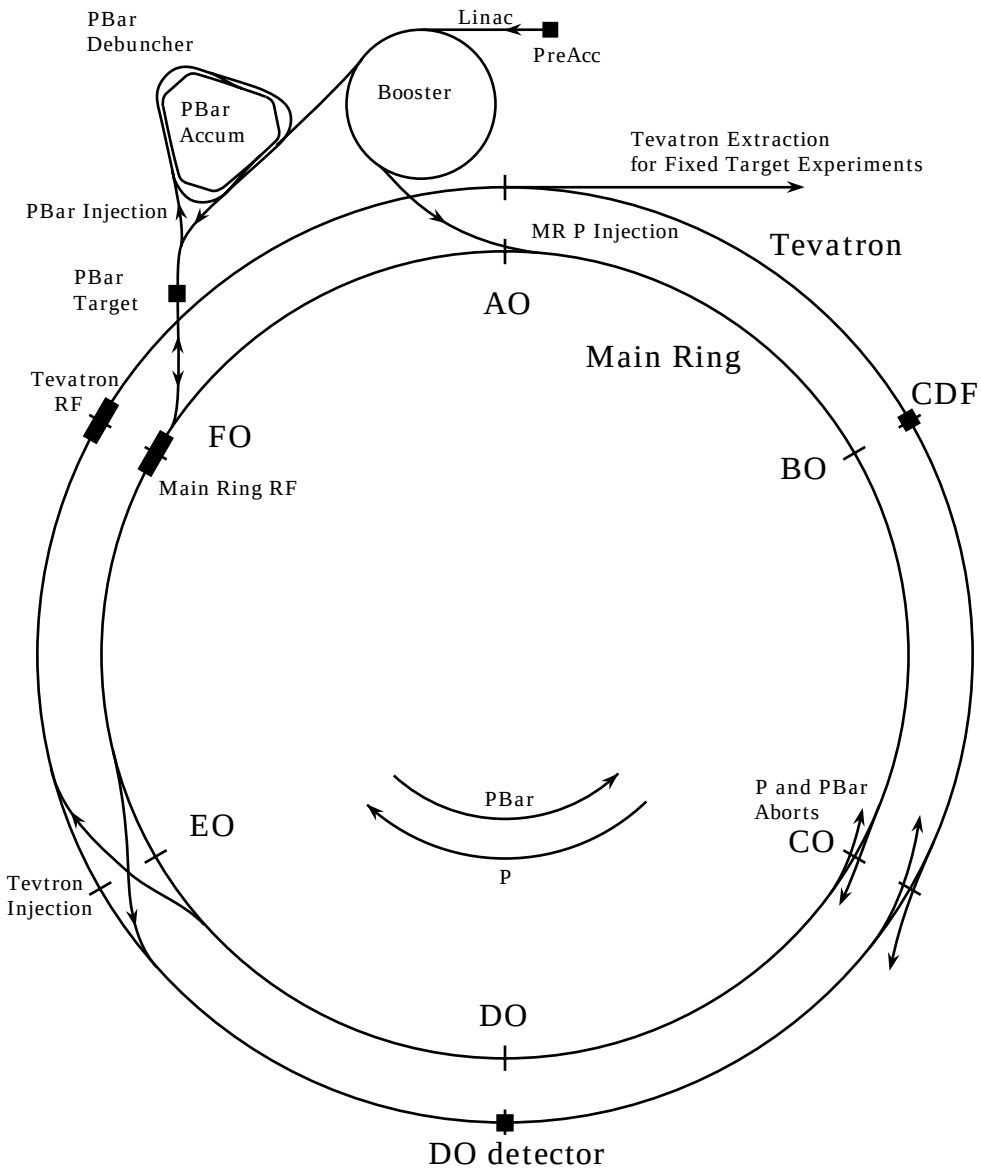

Figure 2.1: Schematic of the Fermilab accelerator complex.

The Main Ring lies mostly in a plane, except at the B0 and D0 experimental areas where it is bent into overpasses to allow room for the detectors (the separation between the Main Ring and the Tevatron is 19 feet at B0 and 7.5 feet at D0). Protons in the Main Ring can be used to make antiprotons (see below), or they can be accelerated to 150 GeV and injected into the Tevatron.

The Tevatron is a proton synchrotron made from superconducting magnets [14], and it lies just below the Main Ring in the accelerator tunnel. The Tevatron is filled with six bunches of protons and six bunches of antiprotons, traveling in opposite directions. The beams are accelerated to the maximum energy of 900 GeV each and allowed to collide at the B0 and D0 experimental areas. (At other points where the beams would collide, they are kept apart by electrostatic separators). The beams are typically kept colliding for about 20 hours, after which the machine is emptied and refilled with new batches of protons and antiprotons.

The remaining major part of the accelerator complex is the antiproton source [15], which is used to produce and store antiprotons for use in the collider. While collisions are occurring in the Tevatron, the Main Ring continually runs antiproton production cycles at a rate of one every 2.4 s. Protons are accelerated to 120 GeV and extracted onto a nickel target. Each of these collisions produces a spray of nuclear debris, which includes some antiprotons. Immediately following the target is a lithium lens, a cylindrical piece of lithium through which a large (0.5 MA) current is passed. This generates an azimuthal magnetic field which acts to focus negatively-charged particles passing through it. Following the lens is a bending magnet which selects negatively-charged

particles with energies of 8 GeV and transports them to the Debuncher. The Debuncher is a storage ring in which antiprotons are first 'debunched' (rotated in phase space from a configuration with a small time spread and large momentum spread to one with a large time spread but small momentum spread) and then stochastically 'cooled' to further reduce the momentum spread. Stochastic cooling [15, 16] operates by measuring the trajectory of collections of particles relative to the desired orbit. From this information, a correction signal is derived which is passed across the ring to kicker electrodes which apply a force on the particles to move them back towards the desired orbit. The effect on any single particle is very small due to the incoherent contribution of all the other particles near it in the beam, but when repeated over a large number of turns, the effect becomes significant. The antiprotons are kept in the Debuncher until just before the next pulse arrives, about 2.4 s later. They are then transferred to the Accumulator, another storage ring which lies inside the Debuncher. There, cooling continues for several hours, and eventually the antiprotons settle into a dense core near the inner radius of the Accumulator. When enough have accumulated to fill the Tevatron (typically on the order of $50 - 150 \times 10^{10}$), they are extracted from the Accumulator, accelerated to 150 GeV in the Main Ring, and injected in bunches into the Tevatron.

Some of the major parameters of the Tevatron for run I are given in Table 2.1. A more detailed introduction to the accelerator may be found in [17].

Accelerator radius	1000 m
Maximum beam energy	900 GeV
Injection energy	150 GeV
Peak luminosity	$\approx 1 \times 10^{31}\,\mathrm{cm}^{-2}\,\mathrm{s}^{-1}$
Number of bunches	6 p, 6 $\bar{p}$
Intensity per bunch	$\approx 1 \times 10^{11} p$, $\approx 5 \times 10^{10} \bar{p}$
Crossing angle	0°
Bunch length	50 cm
Transverse beam radius	43 μm
Energy spread	0.15×10^{-3}
RF frequency	53 MHz
$\bar{p}$ stacking rate	$\approx 3.5 \times 10^{10}$/hour
Beam crossing frequency	290 kHz
Period between crossings	3.5 μs

Table 2.1: Tevatron Parameters for Run I.

2.4 Overview of the DØ Detector

DØ is a large, multipurpose detector for studying $p\bar{p}$ collisions which has been operating at the Fermilab Tevatron since 1992. The design was optimized for the study of high-p_T physics and high mass states, and stresses the identification and measurement of electrons and muons, the measurement of the direction and total energy of high-p_T jets, and the determination of the total transverse energy.

A cut-away view of the DØ detector is shown in Figure 2.2. The detector is about 13 m high $\times$ 11 m wide $\times$ 17 m long with a total weight of about 5500 tons. It consists of three major systems: the central tracking system, the calorimeter, and the muon detector. The *central tracking* detectors

are closest to the interaction point, and are devices designed to measure the three-dimensional trajectories of charged particles passing through them. The *calorimeter* surrounds the central tracking detectors, and is a device which measures the energy of particles. A calorimeter should be 'thick' so that it will absorb all the energy of incident particles, whereas, the central tracking detectors should contain as little material as possible so as to minimize multiple scattering and losses prior to the calorimeter. A calorimeter is typically thick enough to stop all known particles except for muons and neutrinos. The *muon detectors* are tracking chambers outside the calorimeter; since muons have long lifetime, and have no strong interactions, any charged particle originating from the interaction point and penetrating the calorimeter is most probably a muon. A magnetic field of about 2 Tesla is provided for a measurement of the muon momentum.

A brief overview of the individual detector elements is provided below.

2.5 Central Detectors

The central tracking system measures the three-dimensional trajectories (tracks) of charged particles passing through them. Using the tracks, the interaction vertex for an event is determined. The system consists of four parts: the Vertex drift chamber (VTX), the Transition Radiation Detector (TRD), the Central Drift Chamber (CDC), and two Forward Drift Chambers (FDC). The entire tracking assembly is contained within a non-magnetic cylindrical volume concentric with the beryllium beam pipe, with an inner radius of 3.7

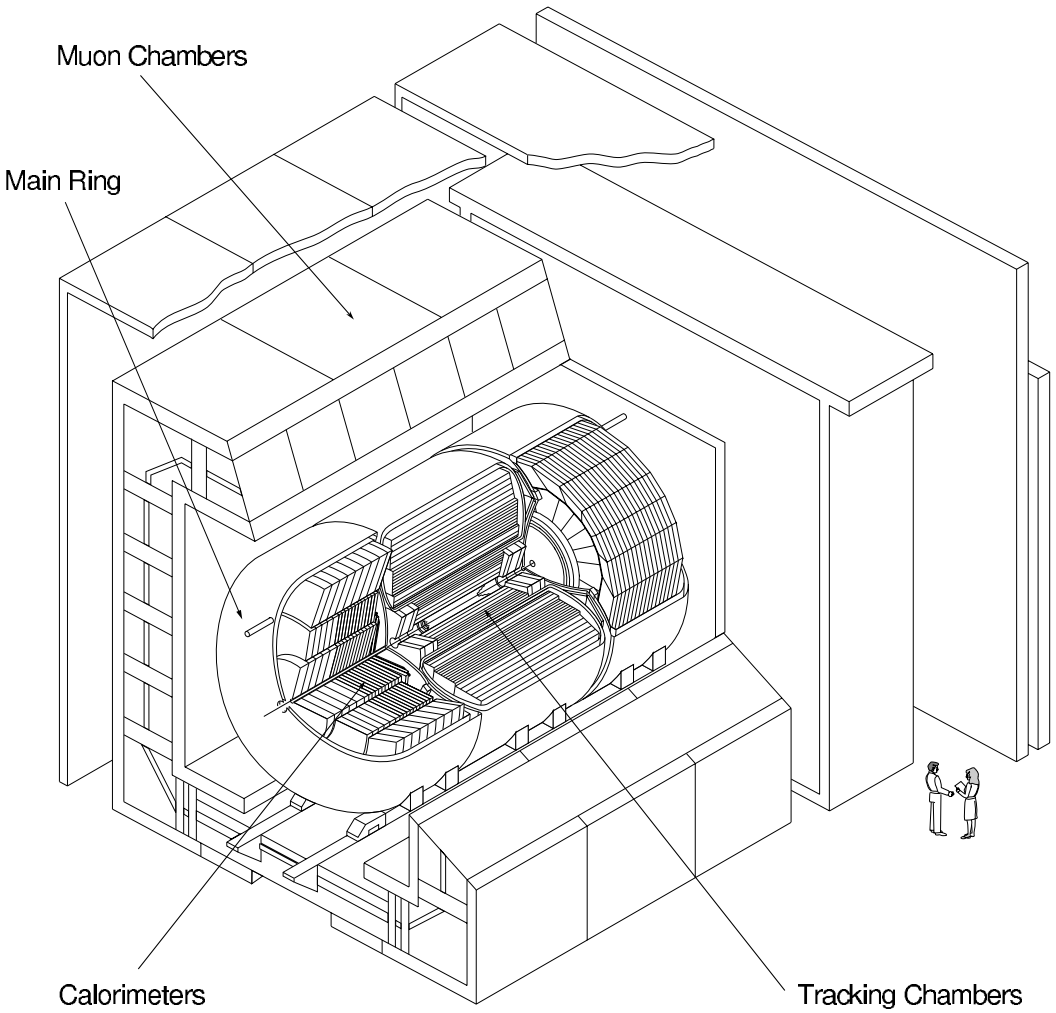

Figure 2.2: Cutaway view of the DØ detector.

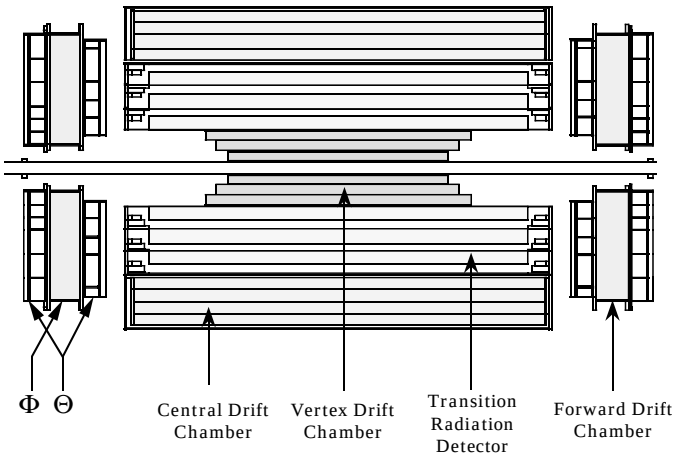

Figure 2.3: Side view of the DØ central detector.

cm and an outer radius of 78 cm as shown in Figure 2.3.

2.5.1 Vertex Drift Chamber (VTX)

The VTX is the innermost tracking chamber. It is designed to provide a precise measurement of the $p\bar{p}$ interaction vertex along the z axis. It extends from 3.7 cm to 16.2 cm in radius, and to ± 58 cm in z. It consists of three concentric cylindrical drift chambers, holding arrays of sense wires parallel to the beam line as shown in Figure 2.4. The sense wires operate at an electric potential of 2.5 kV. Carbon dioxide (CO_2) mixed with 5% etane (C_2H_6) and 5% water serves as the *active medium*. Incoming charged particles ionize the active medium and produce electrons which drift to the sense wire in the electric field. The arrival times of drift electrons at the sense wires provide detailed charged particle tracking in the r-ϕ plane [18]. Readout at both ends of the wires provides a measurement of the z co-ordinate of the particle. The

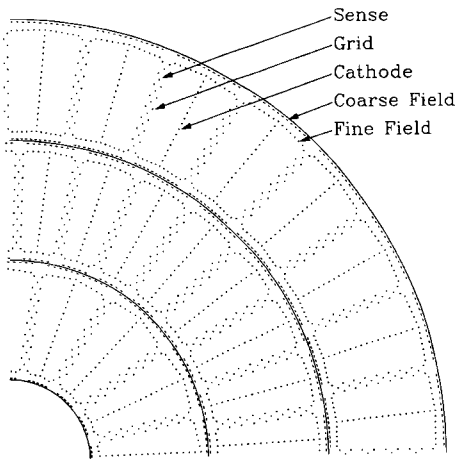

Figure 2.4: End view of one quadrant of the VTX chamber.

spatial resolution of the VTX is about 60 μm in $r\phi$ and 1.5 cm in z.

2.5.2 Transition Radiation Detector (TRD)

When a highly relativistic charged particle crosses the boundary of two materials with different dielectric constants, it radiates photons in the forward direction; this radiation is called transition radiation [18]. The intensity of the radiation is proportional to the energy-mass (E/m) ratio of the particle. Thus for heavy particles, like the pions, the radiation is hardly measurable, while for the electrons, there is considerable transition radiation. The radiation spectrum emitted by multi-GeV electrons is in the form of X-rays.

The TRD is designed to achieve a 10^4 rejection factor against charged pions, while being 90% efficient with isolated electrons. It is located just outside the vertex drift chamber. It consists of three layers. Each layer has a radiator consisting of 393 layers of 18 μm-thick polypropylene foil with a

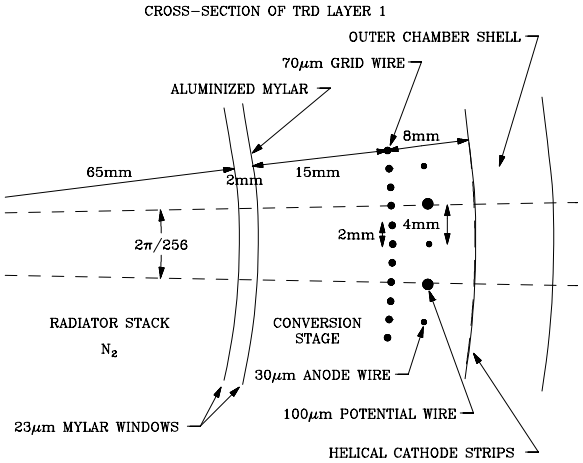

Figure 2.5: A cross section of a TRD layer.

mean separation of 150 μm as shown in Figure 2.5. The gaps are filled with dry nitrogen (N_2). Surrounding each radiator is a cylindrical drift chamber filled with a mixture of xenon (Xe), methane (CH_4) and ehane gases in the ratio 91%: 7%: 2%, designed to detect the X-rays. The TRD extends upto $|\eta_{det}| < 1.1$.

2.5.3 Central Drift Chamber (CDC)

The CDC lies between the TRD and the calorimeter. It consists of four concentric layers of cells located between 49.5 cm and 74.5 cm in radius and between ± 92 cm in z. An end view of a portion of the CDC is shown in Figure 2.6.

Each layer of CDC has 32 identical modules, which are arranged in a cylinder. Each layer is offset by one half cell from the previous layer. Each cell contains seven sense wires (indicated by the smallest dots in Figure 2.6) with

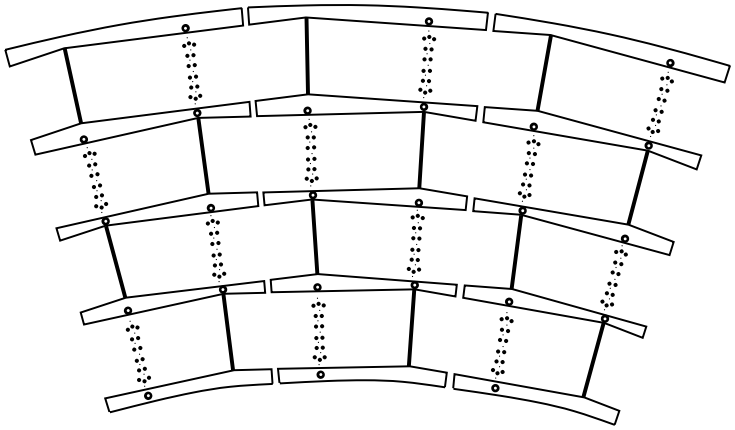

Figure 2.6: End view of 3 of 32 CDC modules.

two grounded potential wires in between the sense wires. Two delay lines lie inside the inner and outer cell walls. The active medium in CDC is gaseous argon (Ar), methane, carbon dioxide, and water in the ratio 92.5%:4%:3%:0.5%. The $r\phi$ position measurement is achieved by the drift chamber principle discussed in Section 2.5.1. The delay lines are used for determining the position in z. The delay lines are inductive wires which transmit an induced electric pulse when an avalanche occurs nearby. By measuring the difference in the arrival time of pulses at both ends of the delay line, one can infer the z position of the avalanche. For the CDC, the $r\phi$ resolution is about 180 μm and the z resolution is about 2.9 mm.

The CDC is used for the reconstruction of a charged particle track. The tracks are also used to determine the event vertex as discussed in Section 3.2.

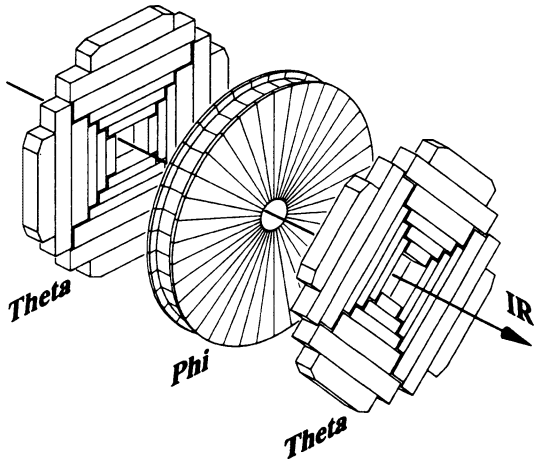

Figure 2.7: Exploded view of one of the FDCs.

2.5.4 Forward Drift Chamber (FDC)

The FDC has a tracking coverage of $1.0 < |\eta_{det}| < 3.2$. There are two sets of chambers, one located at each end of the CDC. Figure 2.7 shows an exploded view of one of the FDCs. Each FDC consists of three layers of chambers: one Φ layer sandwiched between two Θ layers. The Φ layer is a single chamber divided into 36 azimuthal drift cells, each containing 16 axial sense wires. Each of the four quadrants of a Θ chamber consists of 6 rectangular cells. Each cell contains 8 sense wires and one delay line. The two Θ chambers are rotated in ϕ by 45° to obtain optimal position resolution. The operating principle of the FDC is the same as that of the CDC. The $r\phi$ resolution is about 200 μm and the z resolution is about 4 mm.

2.6 Calorimetry

Because of the absence of a central magnetic field at DØ for Run I, the experiment relies heavily on the calorimeter for energy measurements. The calorimeter also plays an important part in the identification of electrons, photons, hadrons, and muons, as well as in the determination of the transverse energy imbalance used to infer the presence of neutrinos. The geometry of the calorimeter is shown in Figure 2.8. It is segmented into three major parts: one central calorimeter (CC), and two end calorimeters (EC), each consisting of an inner electromagnetic (EM) section, a fine hadronic (FH) section, and a coarse hadronic (CH) section, and housed in a steel cryostat. Between the cryostats are the inter-cryostat detector (ICD) and the 'massless gap' (MG) detector.

The electrons/photons (EM objects) and hadrons lose energy in the calorimeter through different mechanisms. A high-energy electron ($E >> 10$ MeV) loses its energy primarily through bremsstrahlung, while a high-energy photon loses energy primarily through electron-positron pair production. The particles emitted in these processes can themselves undergo bremsstrahlung and pair production, producing secondary electrons, positrons, and photons, eventually giving rise to an *electromagnetic shower* [18]. The rate at which an incident EM object loses energy can be described by the following equation:

$$\frac{dE}{E} = -\frac{dx}{X_0}. \tag{2.8}$$

where X_0 is called the *radiation length*, and is the thickness of the collision material required for the EM object to lose all but 1/e of its initial energy.

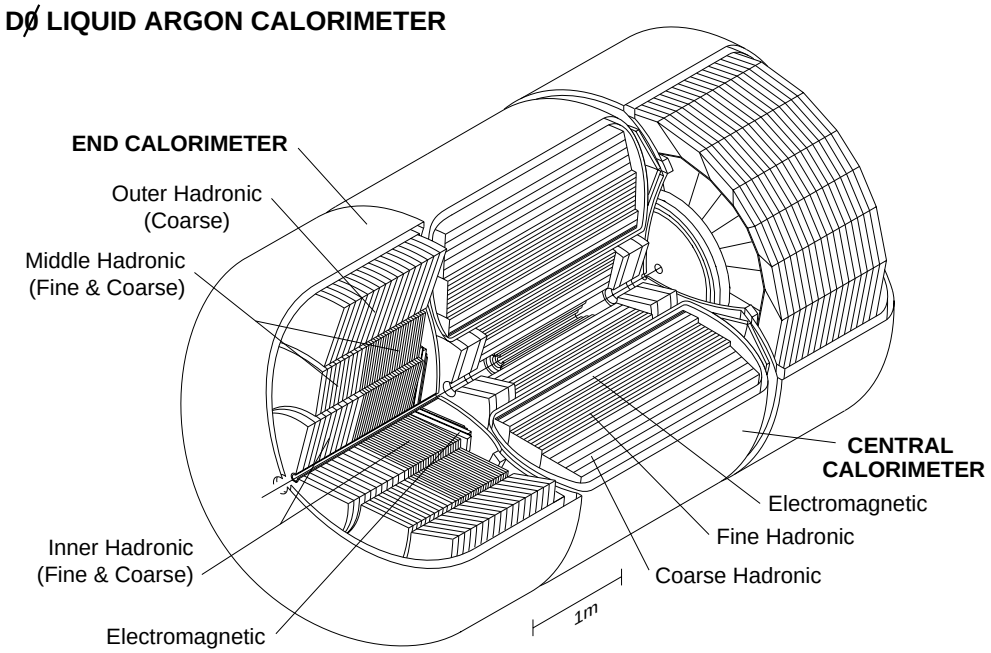

Figure 2.8: The DØ calorimeter.

It is a constant for a given type of material. For example, for uranium, it is about 3.2 mm.

Hadrons also produce showers in material, but through a qualitatively different process. They lose energy primarily through inelastic collisions with atomic nuclei. These collisions produce secondary hadrons, which eventually result in *hadronic showers*. The energy loss in this case, can also be characterized by Eq. (2.8), with X_0 being the *nuclear interaction length*. The nuclear interaction length in uranium is about 10.5 cm. Thus, hadronic showers, in general, tend to be longer than electromagnetic showers.

The showering process converts a single high-energy particle into many low-energy particles. The next step is to measure the energy of these particles.

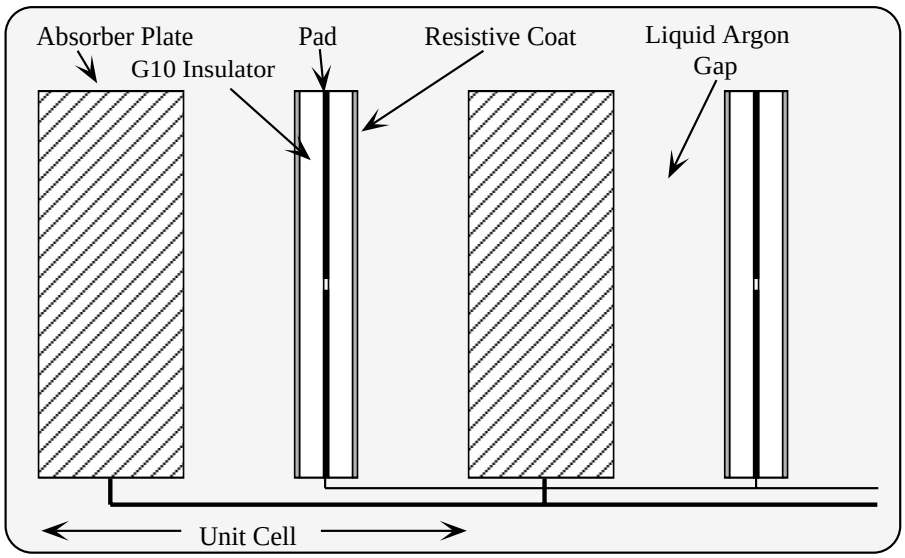

Figure 2.9: Schematic view of a calorimeter cell.

In order to build a calorimeter to contain most of the high-energy showers as well as to keep the cost reasonable, DØ uses a 'sampling' calorimeter. It consists of alternate layers of a dense absorber in which the shower is created, and an active medium which is sensitive to particles passing through it. Since most of the energy is absorbed in the inert material, only a portion of the incident energy can be detected in the active medium. From the sampling fraction, which depends on the design of the detector, the incident energy can be inferred. A schematic view of the DØ calorimeter units (called *calorimeter cells*) is shown in Figure 2.9. At DØ, liquid argon is used as the active medium while plates of uranium (3 mm thick), uranium mixed with 1.7% niobium (6 mm thick), and copper/steel (46.5 mm) are used as the absorber in the EM, FH, and CH calorimeter, respectively.

The material used as the absorber is important. It needs to be dense enough to hold the showers within reasonable size, and it should also improve the energy resolution. In general, the response of a calorimeter (i.e., the ratio of the measured signal to the energy of an incident particle) will tend to be smaller for hadronic showers as compared to the response to electromagnetic showers, since ν's and μ's produced by π and K decays will escape from the detector. The energy spent in breaking up nuclei will also be invisible. This is quantified by the e/π *ratio*, the ratio of the calorimeter responses to electrons and pions. It is highly desirable that it is close to unity due to the following reason. A hadronic shower will include not only hadrons but also electromagnetic component from π^0 and η decays. The fraction of a hadron's energy which is deposited as electromagnetic showers can undergo large variations from shower to shower, but if the e/π ratio is 1, these fluctuations will not affect the energy resolution. A calorimeter with $e/\pi \approx 1$ is called a *compensating* calorimeter. DØ uses uranium as the primary absorber material, since the 'invisible' energy losses from nuclear break-up can be compensated by the extra energy released by nuclear fission of uranium. The e/π ratio of the DØ calorimeter has been measured and it reduces from about 1.11 at 10 GeV to about 1.04 at 150 GeV.

A side view of one quadrant of the DØ calorimeter is shown in Figure 2.10. Each EM section is 21 radiation lengths deep, and is divided into four longitudinal layers: EM1-EM4 layers. The hadronic sections are 7-9 nuclear interaction lengths deep, and are divided into four (in CC) or five (in EC) layers. The cells are aligned in towers projecting back toward the center of the detector. The size of each cell is $\Delta\eta \times \Delta\phi = 0.1 \times 0.1$, except in the third layer of

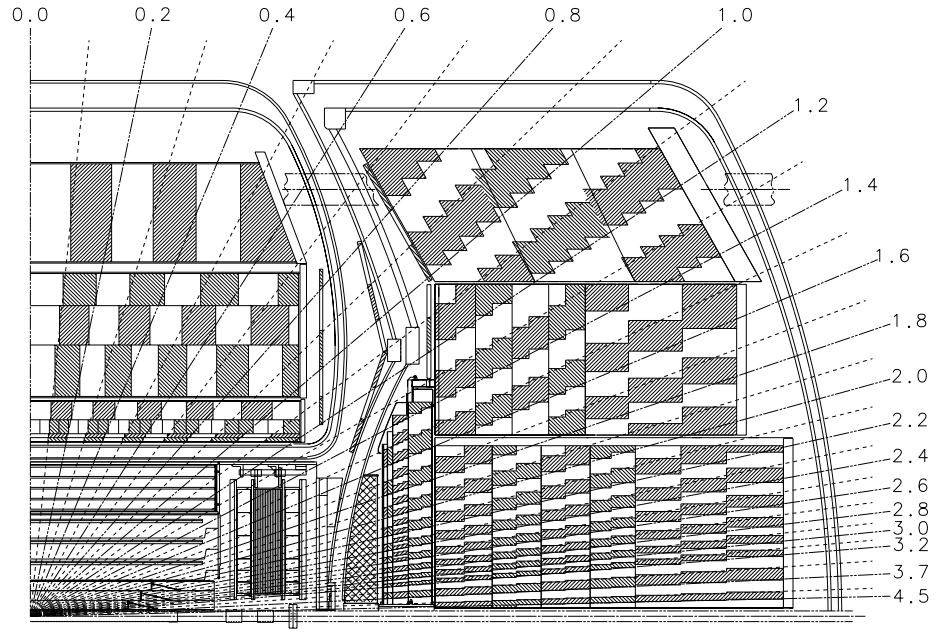

Figure 2.10: Side view of the calorimeters.

the EM calorimeter, where the maximum of an electromagnetic shower is expected. The third layer is therefore segmented into finer cells of size $\Delta\eta \times \Delta\phi$ $= 0.05 \times 0.05$, in order to improve the position resolution of the shower. The CC and EC extend to about $|\eta_{det}| < 4.0$.

If one examines Figure 2.10, it is apparent that in the transition region ($0.8 < |\eta_{det}| < 1.4$) between the CC and the EC there is a relatively large amount of uninstrumented material. This is primarily due to the cryostat walls and the support structures for the calorimeter modules. Two additional devices are used in this region to sample some of the energy deposited in this

dead material. The first of these are the massless gaps (MG). These are simply rings of two signal boards immersed in liquid argon. The second device is the inter–cryostat detector (ICD). This is a ring of scintillation counters mounted on the exterior of the EC cryostats. Both the MG and the ICD have the standard segmentation of 0.1×0.1 in η-ϕ space.

The energy resolutions for electromagnetic objects and pions as measured using test beams [13] are:

$$\frac{\sigma(E)}{E(GeV)} = \frac{15\%}{\sqrt{E}} \oplus 0.3\%, \text{ for EM objects} \tag{2.9}$$

$$\frac{\sigma(E)}{E(GeV)} = \frac{40\%}{\sqrt{E}}, \text{ for charged pions.} \tag{2.10}$$

For hadronic jets, the energy resolution is determined to be:

$$\frac{\sigma(E)}{E(GeV)} = \frac{80\%}{\sqrt{E}}. \tag{2.11}$$

The position resolution for electrons is found to be about 0.8–1.2 mm, varying approximately as $1/\sqrt{E}$.

2.7 Muon System

The DØ muon system [19] consists of five magnetized iron toroids which are surrounded by three layers of proportional drift tubes (PDTs). See Figure 2.11. The PDTs measure the trajectory of muons before and after they traverse the magnetized iron; thus a measurement of the muon momentum can be made. The five magnets are the CF (Central Fe), extending to $|\eta_{det}| < 1$, the two EFs (End Fe) between $1 \leq |\eta_{det}| < 2.5$, and the two SAMUS (Small

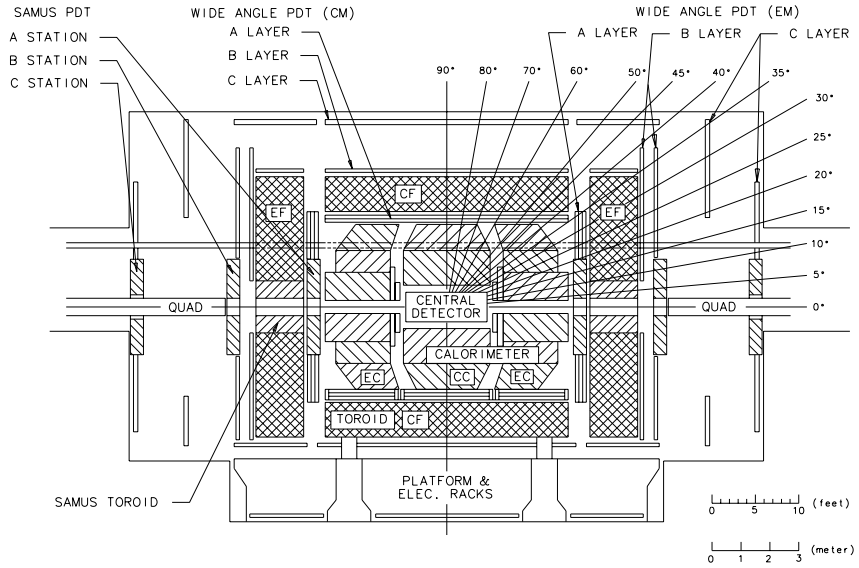

Figure 2.11: Side elevation of the muon system.

Angle MUon System) magnets between $2.5 \leq |\eta_{det}| < 3.6$. The CF and the two EFs together are referred to as the Wide Angle MUon System, or WAMUS. Each section has one layer of drift tubes (the A layer) just inside the magnet, a second layer (B layer) just outside the magnet, and a third layer (C layer) 1–3 m further out. Tracks through the B and C layers give the trajectory after the magnet, while tracks through the A layer give the trajectory before the magnet. Layer A can determine the incident direction of muons to within 0.6 $m$rad and its position in z to within 100 μm; layers B and C can determine the direction and position of an outgoing muon to within 0.2 $m$rad and 170 μm, respectively. The A layer tracks can also be matched to tracks in the central detector and to minimum ionizing traces in the calorimeter in order to improve the direction measurement. The momentum (p) resolution is parametrized in

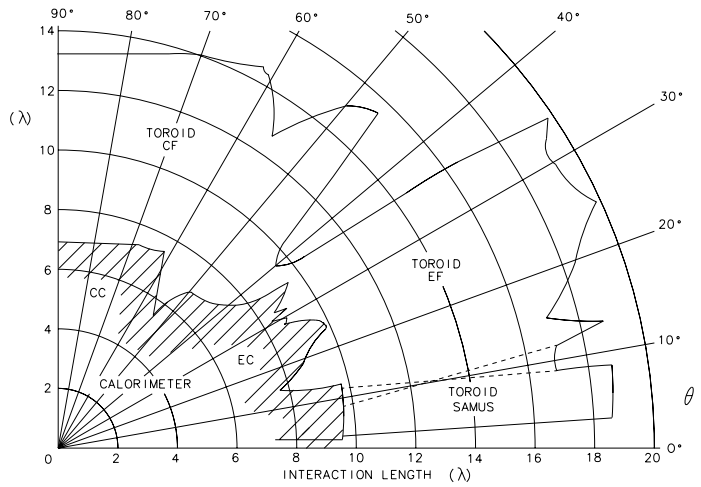

Figure 2.12: Number of nuclear interaction lengths as a function of polar angle.

terms of the inverse momentum $k = 1/p$ as:

$$\left(\frac{\delta k}{k}\right)^2 = (0.18)^2 + \left(\frac{0.003}{k\,\mathrm{GeV}}\right)^2, \tag{2.12}$$

since the resolution is more nearly Gaussian in this variable. The minimum muon momentum required to make it through both the calorimeter and iron is about $3.5\,\mathrm{GeV}/c$ [20] at $\eta = 0$. At higher η, this rises to about $5\,\mathrm{GeV}/c$.

There are two main backgrounds to contend with in case of muons: cosmic ray muons, and leakage of the end portions of the hadronic showers. As for the latter background, the more the material which must be traversed prior to entering the muon system, the smaller will be the background due to hadronic punchthrough. Figure 2.12 shows how the thickness of the detector in nuclear

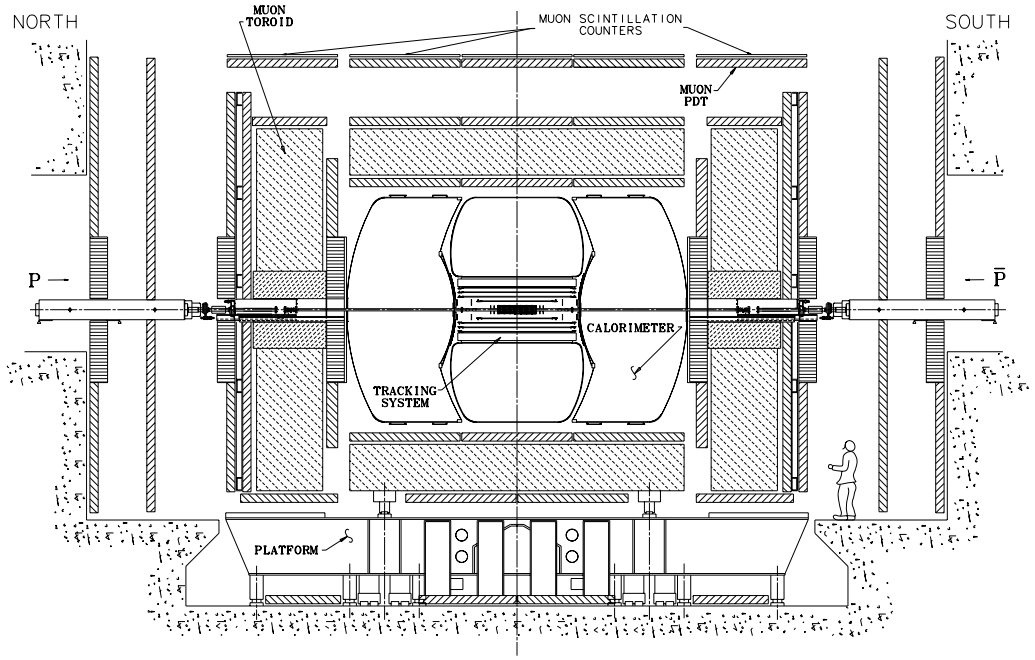

Figure 2.13: An elevation view of the DØ detector showing the location of the muon scintillation counters.

interaction lengths varies with polar angle. At DØ, the thickness of the calorimeter and the iron toroids is enough to keep the hadronic punchthrough negligible for most parts of the detector. This also makes it possible to track muons within jets[1]. In the present analysis we have used this feature of the detector to identify muons (called *tag* muons) from semi-leptonic decays of the b-quark.

To reduce the background from cosmic ray muons, additional scintillation counters were installed during the latter portions of data taking, on the sides and top of the central muon system (CF) as shown in Figure 2.13. These

[1]A muon within a jet is called a *non-isolated* muon; it will be discussed in more detail in chapter 4.

scintillation counters were fabricated at Fermilab and at Tata Institute of Fundamental Research (TIFR) using Bicron 404A scintillator. The light from the scintillation counters was collected by Bicron 91A wavelength shifting fibers and readout using 1.5-inch diameter EMI 9902KA photomultiplier tubes. Details of the fabrication and installation can be found in Ref [21]. The fast timing information of the scintillator allows the time-of-flight of the muon to be used as a discriminator against cosmic rays, as well as against effects of beam halo[2], and back–scattered particles[3].

2.8 Triggering and Readout

At the Tevatron, $p\bar{p}$ beam crossings occur at the interaction region at a rate of about 290 kHz. At a luminosity of 5×10^{30} cm^{-2} s^{-1}, an inelastic collision will occur in about 3/4 of these crossings [13]. However, the processes which are of the greatest interest are much rarer. As it is not feasible to record and process data from every crossing, there must be some mechanism to select out the small fraction of interesting events for permanent storage. This process is called *triggering*. The DØ trigger system reduces the event rate from 290 kHz to about 3-4 Hz, suitable for recording on tape.

---

[2]The beam halo is an accelerator–related effect, and inludes particles that traverse the detector along with the protons involved in the collision. These particles arrive early at the scintillation counters relative to the events associated with the $p\bar{p}$ interaction.

[3]The back–scattered particles are produced by particles from the $p\bar{p}$ interaction, that strike the inner radius of the calorimeter, beam collimators, and the accelerator quadrupole magnets at either end of the detector, and get scattered.

The trigger system at DØ is composed of three hardware stages (Level 0, Level 1, and Level 1.5) and one software stage (Level 2). The first stage (Level 0) consists of hodoscopes of scintillation counters mounted close to the beam on the inner surfaces of the end-calorimeter (EC) cryostats. It performs the following four functions:

- triggers on inelastic $p\bar{p}$ collisions by requiring coincidence between hits in the scintillation counters at the two sides of the detector;
- provides a fast measurement of the z position of the interaction vertex by calculating the difference in arrival time of hits in the scintillation counters at the two sides of the detector;
- measures the relative instantaneous luminosity;
- identifies events that are likely to contain multiple interactions within one beam crossing.

This stage is typically used as an input to Level 1.

The next stage (Level 1) forms fast analog sums of the transverse energies in calorimeter towers. These towers (called trigger towers) have a size of $\Delta\eta \times \Delta\phi = 0.2 \times 0.2$ and are segmented longitudinally into electromagnetic (EM) and hadronic sections. Based on these sums and also the patterns of hits in the muon spectrometer, the Level 1 trigger decision takes place within the time of a single beam crossing of 3.5 μs, unless a Level 1.5 decision is required (see Sections 2.8.1 and 2.8.2). The event rates from Level 1 and Level 1.5 are typically 800 Hz and 200-300 Hz, respectively.

Events accepted at Level 1 are digitized and passed on to the Level 2 trigger which consists of a farm of 48 general-purpose processors. Software filters running on these processors make the final trigger decision.

At both Level 1 and Level 2, the triggers are defined in terms of specific objects: electron/photon, muon, jet, and missing transverse energy, $\not\!\!E_T$. We will briefly describe below the triggers for these objects.

2.8.1 Electron (and photon) triggers

At Level 1, the triggers for electrons (and photons) require the transverse energy in the EM section of the calorimeter to be above programmed thresholds: $E_T \equiv E\sin\theta > T$, where E is the energy deposited in the tower, θ its angle with the beam as viewed from the center of the detector, and T a programmable threshold.

The Level 2 electron triggers exploit the full segmentation (in η-ϕ space) of the EM calorimeter to identify electron showers. Using the trigger towers above threshold at Level 1 as seeds, the algorithm forms clusters that include all cells (with energy deposits) in the four EM layers and the first FH layer in a region of $\Delta\eta \times \Delta\phi = 0.3 \times 0.3$, centered on the highest-E_T tower. It checks the shower shape against criteria on the fraction of the energy found in the different EM layers. The E_T of the electron is computed based on its energy and the z position of the interaction vertex as determined from the timing of hits in the Level 0 hodoscopes. The Level 2 algorithm can also apply an isolation requirement or demand an associated track in the central detector.

During later portions of data taking, the Level 1.5 trigger processor became available for selecting electrons and photons. For this purpose, the E_T of each EM trigger tower passing the Level 1 threshold is summed with the neighbouring tower that has the most energy and a cut is made on this sum. The hadronic portions of the two towers are also summed and the ratio of the EM transverse energy to the total transverse energy is required to be greater than 0.85. The use of a Level 1.5 electron trigger is indicated as an "EX" tower in subsequent reference.

2.8.2 Muon triggers

Muon triggers make use of hit patterns in the muon chambers at Level 1 and provide the number of muon candidates in different regions of the muon spectrometer. The algorithm searches for hit patterns consistent with a muon originating from the nominal vertex ($z = 0$). A Level 1.5 processor is also available and can be used to place a p_T requirement on the candidates (at the expense of a slightly increased dead time[4]). The use of a Level 1.5 muon trigger is indicated as an "MX" muon in subsequent reference.

At Level 2, muon tracks are reconstructed using the muon PDT hits and the z position of the interaction vertex from Level 0. Valid muon track selection is based on the muon p_T and quality requirements (similar to those of Section 3.4). The Level 2 muon trigger can also require the presence of a minimum ionizing particle trace in the calorimeter cells ("cal-confirm") along

[4]Level 1.5 decision times for muons typically range from 1 to 5 μs in the WAMUS regions, but can take up to 100 μs in the busy SAMUS region.

the track. In order to reduce background from cosmic rays and effects of beam halo and back-scattered particles, an additional trigger ("scint") was used in the later portions of data taking, after layers of scintillator were added to the exterior of the central muon system. This trigger required the scintillator timing to be in a window of 30 ns before to 70 ns after the beam crossing.

2.8.3 Jet triggers

Jet triggers use projective towers of energy deposition in the calorimeter similar to the EM trigger towers but including energy from all the layers in the hadronic portion of the calorimeter. Level 1 jet triggers require the sum of the transverse energy in the EM and FH sections of a calorimeter tower (jet tower) to be above programmed thresholds: $E\sin\theta > T$, where E is the energy deposit in the tower, θ its angle with the beam as seen from the center of the detector, and T a programmable threshold. Alternatively, Level 1 can sum up the transverse energies within "large-tiles" of size 0.8 $\times$ 1.6 in η-ϕ space and cut on these sums. The Level 2 jet algorithm begins with an E_T-ordered list of towers (or, *seeds*) that are above threshold at Level 1. A jet is formed by placing a cone of radius $R = \sqrt{\Delta\eta^2 + \Delta\phi^2}$ around the seed from Level 1. If another seed tower lies within the jet cone, then it is passed over and not allowed to seed a new jet. Using the vertex position measured by the Level 0 hodoscopes, the summed E_T in all of the towers included in the jet defines the jet E_T. If any two jet cones overlap, then the towers in the overlap region are added into the jet candidate that was formed first.

2.8.4 Missing transverse energy ($\not\!\!E_T$) triggers

The missing transverse energy ($\not\!\!E_T$) is used to denote the transverse energy of neutrinos and any other non-interacting particles. It is determined from an imbalance of the total transverse momentum in an event and is discussed in more detail in Section 3.6. At both Level 1 and 2, the missing transverse energy is computed from measurements in the calorimeter and is denoted as $\not\!\!E_T^{\rm cal}$. At Level 1, the z position is assumed to be $z = 0$. At Level 2, the vertex position from Level 0 is used. In the offline reconstruction as discussed in Section 3.6, the determination of $\not\!\!E_T^{\rm cal}$ uses the z position as determined by the tracking system which leads to a better resolution compared to that at the trigger level.

2.8.5 Main Ring Vetoes

During normal operation of the Tevatron, the Main Ring is used to produce antiprotons, with a cycle period of 2.4 s [17]. Since the Main Ring passes through the DØ detector (see Figure 2.2), losses from the Main Ring will show up in the detector and must be rejected. The largest losses occur when the beam is injected to the Main Ring. Therefore, one vetoes events during a 0.4 s window starting at injection, and allowing time for the calorimeter and muon high voltages to recover from the large losses. This results in a dead time of about $0.4/2.4 \approx 17\%$ [22]. Even after injection is complete, however, it is still possible to have observable losses whenever a Main Ring bunch passes through the detector. Therefore, events are also vetoed for a particular $p\bar{p}$

beam crossing if a Main Ring bunch is present in the detector within ±800 ns of the crossing. By doing so, one removes events which may be contaminated by Main Ring losses. There are additional schemes employed at the trigger level to reduce or eliminate particles lost from the Main Ring that affect the measurements in the detector. Details of these can be found in appendix B of Ref.[23].

Chapter 3

Reconstruction and Particle ID

The raw event data which comes from the detector is in terms of digitized counts in a calorimeter cell, counts per time bin for a tracking chamber wire, etc. They need to be converted into the kinematic parameters, like the E_T, η, and ϕ, of particles that originated from a $p\bar{p}$ collision, and interacted within the detector. The process of converting the raw detector data into descriptions of objects such as leptons and jets is called *reconstruction*, and is performed using a computer program called DØRECO.

3.1 The Reconstruction Program

The reconstruction process can be divided into three major steps:

- *Hit finding*, during which the raw data is unpacked and converted into 'hits' (i.e., energy deposits in calorimeter cells, or pulses on tracking chamber wires) of definite energy and spatial location.

- *Tracking and clustering*, during which hits which are close together spatially are joined to produce 'clusters' in the calorimeter and 'tracks' in the tracking chambers.

- *Particle identification*, during which information from all parts of the detector is combined to produce a collection of objects which are candidates for being jets, electrons, photons, or muons.

Hit finding for the tracking chambers starts by unpacking the raw digitized data of charge versus time and integrating it to find the total deposited charge (used to calculate dE/dx). The time of arrival of the pulse is used to determine the position of the hit.

In the central detector tracking, the goal is to identify groups of hits which lie along a line. Tracking is first done for each individual layer of the detector to produce track *segments*. Segments are then matched between the layers of each detector to form *tracks*. Finally, tracks are matched between the vertex chamber, the TRD, and the outer tracking chambers (CDC and FDC) [24].

For the calorimeter, hit finding consists primarily of converting the charge deposited in each cell from digitized counts to energy in GeV. This conversion ultimately comes from test beam measurements, in which the response of calorimeter modules to beams of known energy was measured [25].

Following unpacking, the cell energies are converted to transverse energy values using the position of the primary *interaction vertex*, as determined by the central tracking chambers. Cells with the same η and ϕ coordinates are

summed together in the electromagnetic and hadronic calorimeters to produce *towers*. These towers are the input to the jet and electron clustering algorithms, described in the sections below.

The processing of the data from the muon system is similar in spirit to that done for the central detectors but quite different in detail, due to the differences in geometry and in the nature of the front-end electronics.

3.2 Vertex Finding

The location of the hard $p\bar{p}$ collision from which the physical particles (that interact with the detector material) have presumably originated, is called the *interaction vertex*. It may be noted, that the cross-section of the beam is made as small as possible in the x and y directions, in order to maximize the luminosity. The typical cross-section of the beam in the transverse (x-y) plane was about $50\,\mu$m $\times$ $50\,\mu$m, near the center of the detector, with a drift over the period of a data run of less than $50\,\mu$m [26]. Thus, the (x, y) position of the vertex can be taken as a constant, and for many purposes can be set to $(0, 0)$ (the geometrical center of the detector in the transverse plane).

Since the $p\bar{p}$ bunch length along the beam direction is about 50 cm, the z-coordinate of the vertex, however, is less well constrained. Each bunch of particles in the Tevatron has some extent along the beam direction, and the resulting width of the z-distribution of interaction vertices in the detector is about 30 cm. Thus, it is necessary to measure the z-position of the vertex for each event individually. This is done using tracks found in the CDC [26, 27]

as follows:

- Take the tracks found in the CDC and project them back towards the center of the detector.
- For each track calculate the impact parameter — the minimum distance between the track and the z-axis of the detector. Discard all tracks with an impact parameter larger than some cutoff. (This eliminates low-momentum tracks which have undergone a large amount of multiple scattering.)
- Project each track into the (r-z) plane, and compute the intersection with the z-axis. Histogram the z-positions of the intersections.
- Fit a Gaussian around the peak of the resulting distribution. The mean is the estimate of the z-position of the vertex. The outlying regions of the histogram are also searched for any secondary peaks.

This procedure yields a resolution for the vertex z-coordinate of about 6 mm. Multiple vertices can typically be separated if they are at least 7 cm apart [27].

3.3 Electron Identification

Electrons are identified as localized deposits of energy in the electromagnetic calorimeter with an associated central detector track pointing back to the interaction vertex. Since the central tracking system does not measure the charge of particles, it is not possible to distinguish between electrons

and positrons. Therefore, we will henceforth use 'electron' to indicate both electrons and positrons. The algorithm for clustering calorimeter energy and quantities used to distinguish electrons from backgrounds are described below.

3.3.1 Candidate Construction

To identify electron candidates, the reconstruction program uses the following steps:

- Clusters are formed from calorimeter towers using a 'nearest neighbor' algorithm. Starting with the highest-E_T tower, adjacent towers are added to the cluster provided that they are above an E_T threshold, and that the cluster is not too big.

- A cluster is required to have at least 90% of its energy in the EM calorimeter, and at least 40% of the energy in a single tower.

- The centroid of the cluster is computed using the cells in the third EM layer. If $\vec{x}_i$ is the position of the center of cell i and E_i is the amount of energy deposited in that cell, then the centroid is the log-weighted center-of-gravity

$$\vec{x}_{\mathrm{COG}} = \frac{\sum_i w_i \vec{x}_i}{\sum_i w_i}, \text{ with} \tag{3.1}$$

$$w_i = \max\left(0, w_0 + \ln\left(\frac{E_i}{\sum_j E_j}\right)\right). \tag{3.2}$$

  The parameter w_0 is chosen to optimize the position resolution, and the sums are over all EM3 cells in the cluster. The position resolution achieved is about 1.5–2 mm in ϕ, and 0.05 in η.

- Finally, the reconstruction program searches for a central detector track pointing from the interaction vertex to the calorimeter cluster within a "road" of $\Delta\eta = \pm 0.1$, $\Delta\phi = \pm 0.1$. If such a track is found, the cluster is identified as an electron candidate; otherwise, it becomes a photon candidate.

Once an electron candidate has been determined as described above, numerous additional variables are used to improve the identification of electrons. These are briefly discussed below.

- Electromagnetic energy fraction: The electromagnetic energy fraction f_{EM} of a cluster is the ratio of its energy found in the EM calorimeter cells to its total energy. All electron candidates are required to have $f_{EM} \geq 0.9$.

- Isolation fraction ($\mathcal{I}$): Electron showers are compact and mostly contained in the core of EM cells within a cone radius $R = 0.2$ in (η-ϕ) space around the shower center. The isolation fraction $\mathcal{I}$ is defined as the ratio of the energy in the non-core EM and FH cells (E_{tot}) within a cone radius of 0.4 around the center to the energy in the EM cluster core (E_{EM})

$$\mathcal{I} = \frac{E_{\rm tot}(0.4) - E_{\rm EM}(0.2)}{E_{\rm EM}(0.2)}. \tag{3.3}$$

  This quantity tends to be substantially smaller for electrons from the decay of W and Z bosons than for the background, most of which originates from hadronic jets where the electron candidate is usually accompanied by nearby energetic particles.

- Covariance matrix (χ^2_e): A covariance matrix is used to compute a χ^2 variable (χ^2_e) representing the consistency of the cluster shape with that of an electron shower. The method is briefly described below.

  Suppose one has a set of N observations of events of a given type, where each observation consists of M variables: $\mathbf{x}^i = (x^i_1, \ldots, x^i_M)$. One can form the covariance matrix from the outer products

  $$\mathbf{V} = \frac{1}{N}\sum_{i=1}^{N}(\mathbf{x}^i - \bar{\mathbf{x}})^T(\mathbf{x}^i - \bar{\mathbf{x}}), \tag{3.4}$$

  where $\bar{\mathbf{x}}$ is the mean value of the N measurements:

  $$\bar{\mathbf{x}} = \frac{1}{N}\sum_{i=1}^{N}\mathbf{x}^i. \tag{3.5}$$

  An 'H-matrix' is then defined as the inverse of this covariance matrix

  $$\mathbf{H} = \mathbf{V}^{-1}. \tag{3.6}$$

  For any subsequent measurement $\mathbf{y}$, one can define a χ^2_e which describes how likely it is that $\mathbf{y}$ came from the same sample as the $\mathbf{x}$'s:

  $$\chi^2_e = (\mathbf{y} - \bar{\mathbf{x}})\mathbf{H}(\mathbf{y} - \bar{\mathbf{x}})^T. \tag{3.7}$$

  For electron identification, the events $\mathbf{x}$ used to build the H-matrix are Monte Carlo electron events. A total of 41 observables are used, consisting of the fractional energies in layers 1, 2, and 4 of the EM calorimeter, the fractional energies in each cell of a 6×6 array in the third EM layer (centered on the most energetic tower in the cluster), the z-position of the interaction vertex, and the logarithm of the total cluster energy. A

separate matrix is built for each ring of calorimeter cells with the same $|\eta|$ coordinate.

- Cluster–track match significance (σ_{trk}): This is a measure of the consistency between the track position and the cluster centroid. A significant source of background to electrons is photons, either produced directly or by the decay of π^0 and η mesons. Such photons do not create tracks in the central detector, but might appear to do so if some charged particle is nearby. This background can be reduced by requiring that the track point accurately at the centroid of the calorimeter cluster. To quantify this, one defines the cluster–track match significance (σ_{trk}):

$$\sigma_{trk} = \sqrt{\left(\frac{\Delta\phi}{\sigma_{\Delta\phi}}\right)^2 + \left(\frac{\Delta z}{\sigma_{\Delta z}}\right)^2}, \tag{3.8}$$

  where $\Delta\phi$, Δz are the co-ordinate differences between the cluster centroid and the point at which the track hits the calorimeter, and $\sigma_{\Delta\phi}$, $\sigma_{\Delta z}$ are the corresponding measurement resolutions. (This form is appropriate for the central calorimeter. In the end region, r replaces z.)

- Track ionization (dE/dx): Photons that convert to e^+e^- pairs before the calorimeter produce pairs of tracks that match an EM cluster well and are too close together to be resolved. Such double tracks can be identified by the amount of ionization (dE/dx) produced along the track; photon conversions typically deposit twice the charge expected from one minimum ionizing particle.

- TRD efficiency (ϵ_t): The response of the TRD is characterized by the

variable ϵ_t:

$$\epsilon_t(\Delta E) \;=\; \frac{\int_{\Delta E}^{\infty} \frac{\partial N}{\partial E}\,(E)\,dE}{\int_{0}^{\infty} \frac{\partial N}{\partial E}\,(E)\,dE}, \tag{3.9}$$

where ΔE is the difference between the total energy recorded in the TRD (E) and that recorded in the layer with the largest signal (this is done to reduce sensitivity to δ–rays) and $\frac{\partial N}{\partial E}$ is the electron energy spectrum from a sample of $W \to e\nu$ events [23]. Hadrons generally deposit energy mainly in a single layer (giving a small value for ΔE) and electrons deposit energy more evenly (giving a larger value for ΔE). Therefore, hadrons tend to have values of ϵ_t near unity whereas the distribution from electrons is roughly uniform over the allowed range from 0 to 1.

- Likelihood ratio (L_4, L_5): In order to obtain the maximum background rejection while keeping a high efficieny for real electrons, the variables f_{EM}, χ^2_e, σ_{trk}, and dE/dx are combined into an approximate four-variable likelihood ratio L_4 for the hypotheses that a candidate electron is signal or background. A five-variable likelihood ratio L_5 is also defined by including the TRD efficiency (ϵ_t) in the likelihood ratio L_4. The likelihood ratios are defined using the Neyman–Pearson test for signal (e) and background (b) hypotheses, where an EM cluster is considered to be an electron if it satisfies

$$L_n \;\equiv\; \frac{p_n(x|b)}{p_n(x|e)} \;<\; k, \tag{3.10}$$

where x is a vector of n observables, $p_n(x|H)$ is the probability density for x if the hypothesis H is true, and k is a cutoff value. The probability

densities are computed by forming the joint likelihood of the four or five variables:

$$\begin{aligned} p_4(x|H) &= p(f_{EM}|H) \cdot p(\chi_e^2|H) \cdot p(\sigma_{trk}|H) \cdot p(dE/dx|H) \quad (3.11) \\ p_5(x|H) &= p_4(x|H) \cdot p(\epsilon_t|H), \end{aligned}$$

where $p(y|H)$ is the probability density for a single variable y if the hypothesis H is true. These signal and background hypotheses are constructed respectively from inclusive $Z \to e^+e^-$ data and inclusive jet production.

Based on these quantities, the following two classes of electron candidates are defined:

- *loose* electrons are defined as objects satisfying $f_{EM} \geq 0.9$, $\chi_e^2 < 300$, $\mathcal{I}$ < 0.1 and $L_5 < 0.5$ for CC and EC clusters.
- *tight* electrons are defined as objects satisfying $f_{EM} \geq 0.9$, $\chi_e^2 < 300$, $\mathcal{I}$ < 0.1 and $L_4 < 0.25(0.3)$ for CC(EC) clusters.

The tight definition is used for the final selection of electrons in data. A summary of these tight electron identification criteria is given in Table 3.1.

3.3.2 Efficiency

The efficiencies for electron identification are obtained by using the $Z \to ee$ mass peak [23]. The procedure is based on a sample of data events using a trigger that has two reconstructed electromagnetic clusters, each with E_T

	CC	EC
Likelihood, L_4	0.25	0.3
Isolation	$\mathcal{I} < 0.1$	$\mathcal{I} < 0.1$
Cov. Matrix χ^2_e	$\chi^2_e < 300$	$\chi^2_e < 300$
EM energy frac.	$f_{EM} \geq 0.9$	$f_{EM} \geq 0.9$
Transverse Energy	$E_T > 20\,\mathrm{GeV}$	
Detector η	$\lvert\eta_{det}\rvert < 2$	

Table 3.1: Summary of electron ID cuts.

$\geq$ 20 GeV. From this sample, one of the electron candidates, denoted as the "tag", is required to be a good electron ($\chi^2_e \leq 100$, $\mathcal{I} \leq 0.15$). If the other electromagnetic cluster, denoted as the "probe", satisfies $\mathcal{I} \leq 0.1$, then the invariant mass of the pair, m(tag, probe), is recorded. This is done separately for probes in the CC and EC regions of the calorimeter. The number of entries in the Z boson mass window, 80 GeV/c^2 < m(tag, probe) < 100 GeV/c^2, with background subtracted, and in the instrumented region of the central tracking system, defines the number of true electron probes. The track finding efficiency, ϵ^{trk}, is defined as the ratio of the number of true electron probes with a track to the total number of true electron probes. Typical values are (82.7 $\pm$ 1.1) % for electrons in the CC and (85.2 $\pm$ 1.0) % for electrons in the EC. The efficiency of electron identification criteria (ϵ^{tight}) is defined by the ratio of the number of true electron probes with a reconstructed track that pass the tight identification requirements to the total number of true electron probes with a reconstructed track. Typical values of ϵ^{tight} are (81.1 $\pm$ 1.0) % in the CC and (51.4 $\pm$ 1.8) % in the EC. These efficiencies do not include geometric

factors due to uninstrumented fiducial regions of detector. The geometrical acceptance ($\mathcal{G}$) for electrons in the DØ detector is determined using Monte Carlo events and is (87.6 ± 0.5) % in the CC and (79.2 ± 1.4) % in the EC. The overall electron identification efficiency, ϵ^{e-ID}(data), is then defined as:

$$\epsilon^{e-ID}(data) = \epsilon^{trk} \times \epsilon^{tight} \times \mathcal{G}. \tag{3.12}$$

Substituting the values for ϵ^{trk}, ϵ^{tight}, and $\mathcal{G}$ in the above equation, we get, for the different regions of the DØ detector:

$$\epsilon^{e-ID}(data) = 0.588 \pm 0.011, \text{ in the CC } (|\eta_{det}| < 1.0) \tag{3.13}$$

$$\epsilon^{e-ID}(data) = 0.347 \pm 0.014, \text{ in the EC } (1.0 \leq |\eta_{det}| < 2.0) \tag{3.14}$$

3.3.3 Electron Energy Corrections

The absolute energy scale of the calorimeters was originally set using test beam calibration data. However, due to differences in conditions between the test beam setup and the DØ installation, this calibration is slightly low. Therefore, all electromagnetic objects are first scaled by a factor which was chosen to make the dielectron invariant mass peak in $Z \to ee$ events match the Z boson mass as measured by the LEP experiments. (This factor is determined separately for each of the three cryostats of the calorimeter[1] [28].)

[1]The current values of these factors are CC: 1.0443 ± 0.0021, North EC: 1.0463 ± 0.0085, South EC: 1.0230 ± 0.0086.

3.4 Muon Identification

Muons are identified as tracks in the muon chambers which point back at the interaction vertex. Since there is a magnetic field between the first and second layers of the proportional drift tubes in the muon chambers, tracking is done separately for segments before and after the magnet. High-p_T muon tracks in the end regions (EF, $|\eta_{det}| \geq 1.0$) are required to have hits on at least 5 PDT planes[2]. The track segments before and after the magnet are matched in order to determine the muon momentum, by measuring by how much the track bends while passing through the magnet[3]. The momentum resolution can be improved by matching the muon track with an associated track in the central detector and with an interaction vertex.

In addition, there are several other variables used to enhance muon identification against background. Those used in this analysis are:

- A-stub veto: Muon tracks with hits in only the innermost (A) layer are excluded.

- Impact Parameter: A three-dimensional impact parameter (IP_{3d}) is defined as the sum in quadratures, of the non-bend and bend-view impact parameters.

  The *non-bend impact parameter* is defined by projecting the muon track

[2]No explicit cut on the number of PDT hits is made in the central region (CF, $|\eta_{det}| < 1.0$), although a muon track in the CF, will typically have 7-10 hits.

[3]The muon momentum (p in meters) can be written in terms of the magnetic field (B in Tesla) and the bending radius (ρ in GeV/c) as $p \approx 0.3B\rho$.

into the x-y plane (it does not get bent in this plane), extrapolating the track formed by the B and C layers towards the center of the detector, and calculating the impact parameter between this extrapolated track and the interaction vertex.

The *bend-view impact parameter* is calculated by projecting the track into the plane in which the muon bends and calculating the impact parameter of this projection.

A cut on the three-dimensional impact parameter helps in discriminating against cosmic rays. Events with hits or a track in the muon chambers on the oppsite side in η and ϕ of a reconstructed muon in the CF are also rejected to reduce background from cosmic rays.

- Muon Quality (IFW4): For each track, the muon reconstruction code makes a set of cuts on the number of modules hit, impact parameters, and hit residuals. The number of cuts which the track fails is called 'IFW4'.

- Calorimeter Confirmation (MTC): A muon passing through the detector will typically deposit between 1 and 3 GeV of energy in the calorimeter. The energy contained in all cells within a one cell radius surrounding the muon track is summed and the following two variables are examined: HFrac and EFracH1. HFrac is the fraction of energy contained in the hadronic calorimeter along the muon track, and EFracH1 is the fraction of energy contained in the outermost layer of the hadronic calorimeter along the muon track.

- Path Length Through Iron Toroids ($\int B \cdot dl$): One tries to exclude muons passing through insufficient magnetic field which will result in a poor measurement of the muon momentum. This is specially true in the region $0.8 < |\eta_{det}| < 1.0$, where the toroid is thin. Eliminating muons in this region also reduces the background due to hadronic punchthrough.

The above cuts define high-p_T ($p_T > 20$ GeV/c), *isolated* muons. An isolated muon is defined to be one for which the distance R in η-ϕ space between the muon and the nearest jet, is greater than 0.5. In this analysis, we also consider soft muons from semileptonic decays of b quarks. These muons (called *tag* muons) are selected using requirements somewhat looser than those outlined above. The tag muon is required to have $p_T > 4$ GeV/c, and to be within $R < 0.5$ of a jet.

A summary of the muon ID cuts is given in Table 3.2.

3.4.1 Efficiency

The total muon–finding efficiency is the product of the muon geometrical acceptance and the muon identification efficiency. The muon geometrical acceptance is determined using Monte Carlo events as (73.7 ± 0.4) % in the CF and (64.1 ± 1.1) % in the EF. The overall muon–finding efficiency is well–modeled by a modified version of DØGEANT [29]. These modifications include input from muon resolutions measured using $Z \rightarrow \mu\mu$ data, and efficiencies of the proportional drift tubes. The muon identification efficiency is obtained from this modified version of DØGEANT but is further corrected to account

	Isolated muon	Tag muon
Momentum	$p_T > 20\,\text{GeV}$	$p_T > 4\,\text{GeV}$
Pseudorapidity	$\lvert\eta_{det}\rvert < 1.7$	$\lvert\eta_{det}\rvert < 1.7$
A-stub veto	yes	yes
IP_{3d}	< 20 cm	—
IFW4	$\leq 1(0)$ in CF(EF)	$\leq 1(0)$ in CF(EF)
MTC	(HFrac>0.6.and.EFracH1>0) .or.HFrac=1	(HFrac>0.6.and.EFracH1>0) .or.HFrac=1
$\int B \cdot dl$	> 0.55 Tm	—
Isolation	$\Delta R(\mu, \text{jet}) \geq 0.5$	$\Delta R(\mu, \text{jet}) < 0.5$

Table 3.2: Summary of muon ID cuts.

for time dependent detector inefficiencies and incorrect modeling of the muon track finding efficiency. This will be discussed in more detail in chapter 7.

3.5 Jet Reconstruction

As discussed in Section 1.1, when a parton (quark or gluon) leaves the site of a hard scattering, it *hadronizes*, or *fragments* into a collection of colorless hadrons. These hadrons will typically lie in a cone around the direction of motion of the original parton, and constitute a *jet*. These jets produce energy depositions in an array of cells in the calorimeter. To determine the jet energy, an algorithm is needed which assigns calorimeter cells to jets.

In Figure 3.1 we illustrate the evolution from *parton* through *particle* to *calorimeter* jets. As an example, consider a quark which may radiate a gluon, as shown in Figure 3.1a. The gluon may be merged with the quark into a single *parton* jet depending on the jet finding algorithm. Further evolution, through

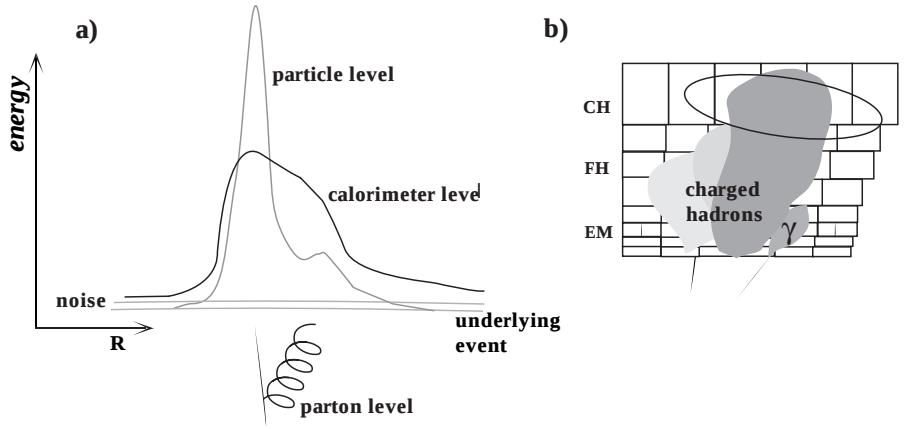

Figure 3.1: Jet evolution. (a) Jets at *parton*, *particle* and *calorimeter* levels. (b) Section of the calorimeter with individual particle showers.

parton showering and hadronization, yields a *particle* jet. After hadronization, the distinction between quark and gluon is blurred. Figure 3.1b shows an example of a jet as it enters the calorimeter: the charged hadrons produce wide showers, while photons from π^0's and η's leave narrower showers confined mainly to the EM portion of the calorimeter. The lightest shower in the figure shows that a fraction of the energy from a particle emitted inside a jet, is showered outside the *calorimeter* jet. *Calorimeter* jet is defined as the object reconstructed with a given algorithm from energy depositions in calorimeter cells. A fixed cone algorithm (described below) is used in this analysis.

3.5.1 Cone Jet Algorithm

The following is a description of the cone jet algorithm as used at DØ [30]:

- Preclustering: The calorimeter towers (see Section 3.1) are first sorted in E_T, and a set of 'seed' clusters are formed. Starting with the highest-E_T tower which has not yet been assigned to a precluster, the precluster is formed from all contiguous towers within $|\Delta\eta| < 0.3$, $|\Delta\phi| < 0.3$ with $E_T > 1\,\text{GeV}$. Preclustering continues until all towers with $E_T > 1\,\text{GeV}$ have been assigned to a seed cluster. For each precluster, the E_T-weighted centroid in η-ϕ space defines the axis of the corresponding jet candidate.

- Cone Clustering: A new cluster is defined around the trial axis including all calorimeter cells within a fixed distance $R = \sqrt{\Delta\eta^2 + \Delta\phi^2}$. The centroid of this new cluster is computed, which defines a new jet axis. This process is then repeated until it stabilizes.

- Merging and Splitting: Once the cone clustering has completed, some cells may turn out to have been assigned to more than one jet. If two jets share some cells, the fraction of the total energy which is shared between them, relative to the transverse energy of the lower-E_T jet, is examined. If the fraction is greater than 50%, the two jets are merged together, and the jet axis recalculated from the centroid of all the cells in the merged jet. Otherwise, the jets are split, and each shared cell is assigned to the closest jet.

- Jet E_T Definition: The E_T of a jet is defined by

$$E_T = \sqrt{E_x^2 + E_y^2}, \tag{3.15}$$

where E_x and E_y are the sums of the components of the individual cell energies:

$$\begin{aligned} E_x &= \sum_i E_x^i \\ E_y &= \sum_i E_y^i. \end{aligned} \tag{3.16}$$

For the present analysis, a cone radius of $R = 0.5$ has been used throughout, and jets are required to have a total E_T above a threshold, which is set to 8 GeV.

3.5.2 Jet Energy Corrections

Ideally, one would like the measured jet energy (E_{jet}^{meas}) to be equal to the energy of the original parton (E_{parton}) which formed the jet. However, there are systematic biases in jet measurements which need corrections. In addition to having to determine the energy scale (just as for electrons), there are several other effects which become important due to the extended, multiparticle nature of jets:

- Many of the particles in even a high-E_T jet will be fairly soft ($\lesssim 2$ GeV). However, the response of the calorimeter becomes non-linear in this region and hence a simple sum of the calorimeter responses to each particle will not give the correct total energy.

- Since the hadronic shower is an extended object, some portion of the shower may extend beyond the jet cone radius of $R = 0.5$.

- A jet will pick up some extra energy due to the underlying event[4], as well as noise due to the natural radioactivity of the uranium absorber. Both of these sources affect jets much more than electrons due to the fact that hadronic showers have a larger spread than electromagnetic showers.

- Some of the particles radiated by the initial parton may fall outside the jet cone of specific radius.

- Any uninstrumented region in the calorimeter will also result in a mismeasurement of the jet energy.

To correct for some of the above effects, we apply the jet corrections in three steps: standard corrections, parton-level corrections, and η-dependent corrections. The first of these corrections is done before event selection (chapter 4) and is used by most DØ analyses; the other two corrections are applied during the kinematic fit (chapter 5) and are specific to the top quark analyses.

Standard corrections

These are mainly intended to correct the measured jet energy (E_{jet}^{meas}) to the particle jet energy (E_{jet}^{ptcl}). First, the electromagnetic objects are scaled as

[4]An underlying event is usually caused by interactions between the 'spectator' quarks, and interactions between the spectator quark and the hard scattering quark.

discussed in Section 3.3.3. Next, jet energies are corrected using the formula

$$E_{jet}^{ptcl} = \frac{E_{jet}^{meas} - O}{R(1-S)}. \tag{3.17}$$

Here, R is the calorimeter response; it is obtained using E_T balance (as determined from the total $\not\!\!E_T$) in γ + jets events [30]. O is the offset due to the underlying event, multiple interactions, and noise from the natural radioactivity of the uranium absorber. It is determined by comparing data with and without the requirement of a hard interaction, and also by comparing data taken at different luminosities. The term S is the fractional shower leakage outside the jet cone in the calorimeter. It is determined by using single particle showers measured in the test beam to construct simulated showers from Monte Carlo jets; this leakage is approximately 3% for a 50 GeV jet in the central calorimeter. Further details about these corrections may be found in Ref. [31].

Parton-level corrections

These are done mainly to correct for energies of particles radiated by the initial parton that may fall outside the jet cone. In other words, parton-level corrections are applied to correct the particle jet energy (E_{jet}^{ptcl}) to the initial parton energy (E_{parton}). To derive this correction, standard $t\bar{t}$ events are generated using HERWIG [32] Monte Carlo and reconstructed jets are matched to the partons from top quark decay. Their energies are then plotted against each other. As seen in Figure 3.2, this relation is observed to be nearly linear. Separate fits are made for light quark jets and for untagged b quark jets. The

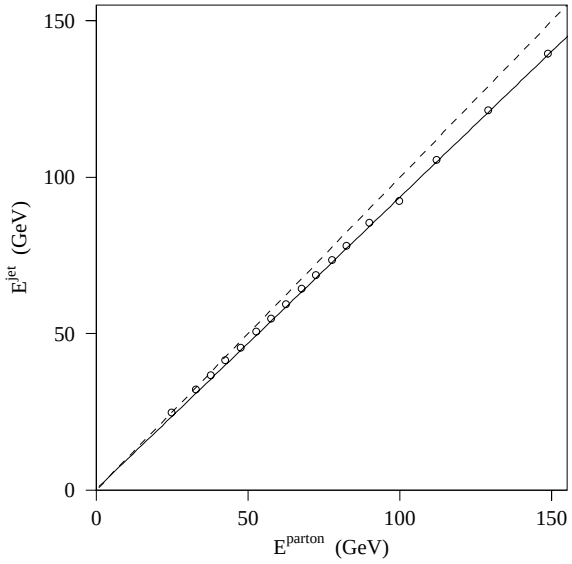

Figure 3.2: The measured jet energies for quarks from $W \to q\bar{q}$ in $t\bar{t}$ Monte Carlo events are plotted against the corresponding parton energies. Radiation outside the jet cone causes the measured jet energy to be lower than the energy at the parton level. The dashed line is drawn along the diagonal, and the solid line is a linear fit to the points. This plot is based on HERWIG fragmentation with $|\eta^{\rm jet}_{det}| < 0.2$.

results are given in Table 3.3 for different regions in η_{det} [30]. For tagged b quark jets, or jets that contain a muon, indicative of a semileptonic b quark decay, additional corrections are applied to compensate on average for the energy carried away by the undetected neutrino. The jet itself is corrected using the light quark corrections; the measured momentum of the tagging muon is scaled to account for the unobserved neutrino, and the estimated *leptonic* energy is then added to the corrected jet energy [33].

η-dependent corrections

These are made to correct the mis-measurement of jet energy due to the uninstrumented region in the calorimeter. For this, we study the response

Table 3.3: Parameters for parton-level jet corrections. $E(\text{corr.}) = (\text{E}_{\text{jet}}^{\text{ptcl}} - \text{A})/\text{B}$.

	Light quark jets		Untagged b jets	
η region	A (GeV)	B	A (GeV)	B
$0.0 < \lvert\eta_{det}\rvert < 0.2$	0.322	0.933	-0.672	0.907
$0.2 < \lvert\eta_{det}\rvert < 0.6$	0.635	0.930	-1.34	0.914
$0.6 < \lvert\eta_{det}\rvert < 0.9$	1.86	0.883	0.002	0.868
$0.9 < \lvert\eta_{det}\rvert < 1.3$	1.70	0.933	-0.548	0.904
$1.3 < \lvert\eta_{det}\rvert$	4.50	0.882	2.46	0.859

of the detector to $\gamma + 1$ jet events, using both data and Monte Carlo. We select events containing exactly one photon with $E_T^\gamma > 20\,\text{GeV}$, $|\eta_{det}^\gamma| < 1.0$ or $1.6 < |\eta_{det}^\gamma| < 2.5$, and exactly one reconstructed jet (excluding the photon) with $E_T^j > 15\,\text{GeV}$, $|\eta_{det}^j| < 2$, and $|\pi - \Delta\phi(j,\gamma)| < 0.2$ rad. We reject events with Main Ring activity and those which are likely to be multiple interactions. To reject W boson decays, we further require that $\not\!\!E_T/E_T^\gamma < 1.2$ if $E_T^\gamma < 25\,\text{GeV}$, or $\not\!\!E_T/E_T^\gamma < 0.65$ otherwise. With this selection, we compute

$$\Delta S = \left\langle \frac{E_T^j - E_T^\gamma}{E_T^\gamma} \right\rangle \tag{3.18}$$

and plot it as a function of η_{det}^j. The result is shown in Figure 3.3 [33]. This reveals detector inhomogeneities in the transition region between the central and end calorimeters. The curve from Monte Carlo is also seen to have a somewhat different shape than that from data. To remove these effects, we smooth the ΔS distributions by fitting them to the sum of several Gaussians, and scale each jet by $1/(1 + \Delta S(\eta_{det}^j))$. This is done separately for data and for Monte Carlo.

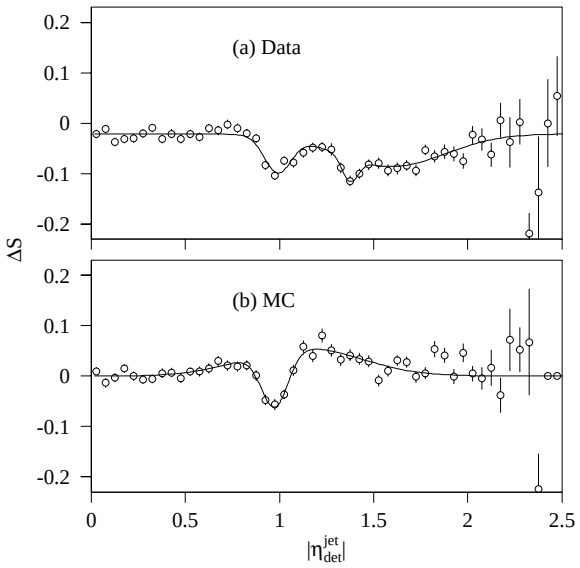

Figure 3.3: The energy scale deviation ΔS as a function of η^j_{det} for (a) data and (b) Monte Carlo (MC). The curves are empirical multi-Gaussian fits to the points.

To estimate the uncertainty in the relative scale between data and Monte Carlo, we derive ΔS as a function of E_T^γ (averaging over η^j_{det}) for both data and MC after all corrections have been applied. The difference of the two is plotted in Figure 3.4 [33], along with a band corresponding to $\pm(2.5\% + 0.5\,\mathrm{GeV})$ of the jet energy, which we use as our estimate of the systematic uncertainty of the jet energy calibration. (It is the relative data-Monte Carlo difference that is relevant, rather than the absolute uncertainty, since simulated events using Monte Carlo are compared with data to extract the results.)

An important check of the validity of these corrections is provided by the transverse energy balance in $(Z \to ee)$+jets events. As shown in Figure 3.5, the corrected jets satisfactorily balance the Z boson. We also show in Figure 3.6 the $W \to q\bar{q}$ and $t \to bq\bar{q}$ masses from $t\bar{t}$ Monte Carlo before and after the final two corrections. It is seen that the proper masses are recovered.

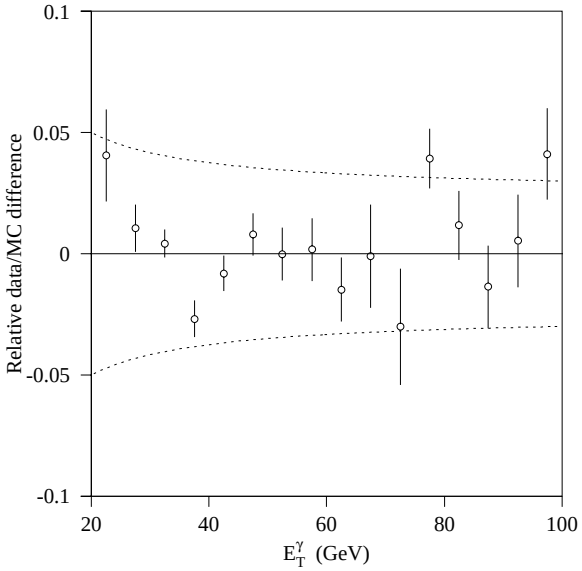

Figure 3.4: The relative energy scale difference between data and Monte Carlo as a function of photon E_T after all jet corrections are applied. The curves indicate an error band of $\pm(2.5\% + 0.5\,\mathrm{GeV})$ of the jet energy.

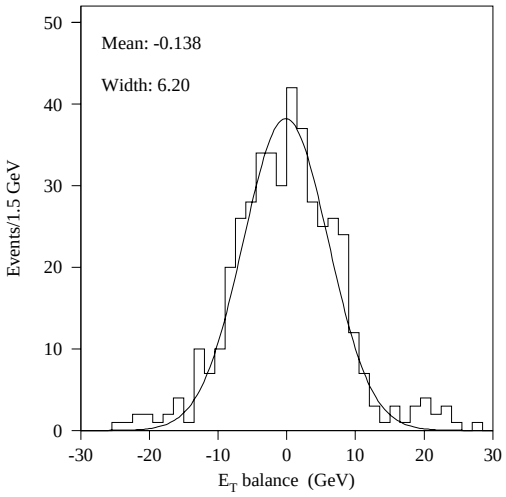

Figure 3.5: Transverse energy balance for $(Z \to ee) + \text{jets}$ events. All jet corrections are applied. The curve is a Gaussian fit to the histogram.

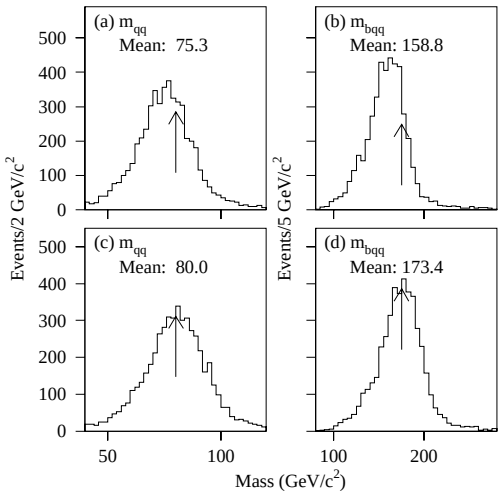

Figure 3.6: Masses of $W \to q\bar{q}$ and $t \to bq\bar{q}$ in standard $t\bar{t}$ Monte Carlo with $m_t = 175\,\mathrm{GeV}/c^2$, both (a), (b) with standard corrections only and (c), (d) with all jet corrections. The arrows locate the input W boson and top quark masses.

3.6 Missing Energy Reconstruction

From momentum conservation and the fact that the colliding proton and antiproton have nearly opposite momenta, it follows that the total vector sum of the momenta of all final-state particles in the event must be zero. However, one cannot usefully apply total momentum conservation in the direction along the beam, since many particles will escape detection by going down the beam pipe. But the very fact that they do escape implies that they have very small transverse momenta; thus, one can apply momentum conservation in the plane perpendicular to the beam. If the sum of the transverse momenta of the detected particles is significantly different from zero, the discrepancy is attributed to one or more neutrinos which escaped detection, and which

must have transverse momentum opposite to the total detected transverse momentum.

3.6.1 Definition of Missing Transverse Energy

Each cell in the calorimeter is given a four-vector, with an energy equal to the measured energy in the cell, a direction pointing from the interaction vertex to the center of the cell, and a mass of zero. The transverse (x and y) components of these vectors are summed over all the calorimeter cells (including the ICD). We define the 'calorimeter missing-E_T' or $\not\!\!E_T^{\rm cal}$ as the negation of this vector as follows

$$\not\!\!E_T^{\rm cal} = \sqrt{\not\!\!E_{T\ x}^{\rm cal\,2} + \not\!\!E_{T\ y}^{\rm cal\,2}} \tag{3.19}$$

where,

$$\not\!\!E_{T\ x}^{\rm cal} = -\sum_i E_x^i - \sum_j \Delta E_x^j \tag{3.20}$$

$$\not\!\!E_{T\ y}^{\rm cal} = -\sum_i E_y^i - \sum_j \Delta E_y^j. \tag{3.21}$$

The first sum is over all cells in the calorimeter and ICD, and the second sum takes into account the corrections in E_T applied to all EM objects and jets in the event.

This does not yet take into account muons, which (in case of high-p_T muons) deposit only a small portion of their energy in the calorimeter. The 'total missing E_T', or just $\not\!\!E_T$, is then obtained by subtracting the transverse momenta of all good muon tracks from $\vec{\not\!\!E}_T^{\rm cal}$.

Chapter 4

Data sample and Event Selection.

As discussed in chapter 1, we consider the production of $t\bar{t}$ pairs in $p\bar{p}$ collisions at a center of mass energy of $\sqrt{s} = 1.8$ TeV, and assume that each top quark decays into a W boson and a bottom quark. We then consider the 'lepton + jets' decay mode of the $t\bar{t}$ pair, in which one W boson decays leptonically and the other W boson decays hadronically (see Figure 4.1). We consider here only the electron and muon modes of the leptonic decay of the W boson since the tau leptons are difficult to identify. This leads to the following modes for the production and subsequent decay of the $t\bar{t}$ pairs, which has an overall branching fraction of $\approx 30\%$:

$$p\bar{p} \rightarrow t\bar{t} \rightarrow (W^+b)(W^-\bar{b}) \rightarrow (e/\mu)\ (\nu)\ (q\bar{q}'\ b\bar{b}). \tag{4.1}$$

Due to the large mass of the top quark, the signature of a $t\bar{t}$ event is a high-p_T isolated lepton (e or μ), large missing transverse energy, $\not\!\!E_T$, due to the undetected neutrino from the leptonic W boson decay, and at least 4

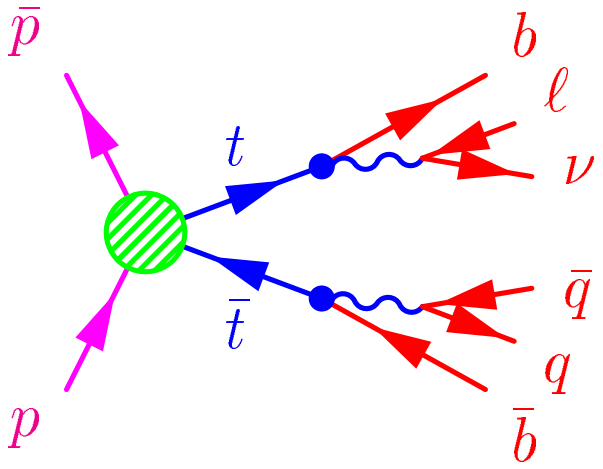

Figure 4.1: A $t\bar{t} \rightarrow l$ + jets decay.

jets: one from each of the two b-quarks, and two from the hadronic W boson decay. There can be additional jets due to initial state and final state (QCD) radiation. Additional soft muons (μ tags) may also be present due to the semileptonic decays of the b-quarks via the processes:

$$b \rightarrow c\mu\nu,\ b \rightarrow c \rightarrow s\mu\nu. \tag{4.2}$$

In the present analysis, we consider two orthogonal classes of events, whose selection is based on: a) a purely topological selection of lepton+jets events which we denote as $e + jets$ and $\mu + jets$, and b) a selection based primarily on the presence of a non-isolated muon (μ tag) with additional selections on the topology of the event. These events are denoted as $e + jets/\mu$ and $\mu + jets/\mu$.

4.1 Data sample

We use the lepton+jets data sample that was also used in the extraction of the mass of top quark [33] at DØ. The trigger requirements used for this data sample at Level 1 and Level 2 are summarized in Tables 4.1–4.3 [23]. These tables are divided according to the three major running periods: run Ia was from 1992–1993, run Ib was from 1994–1995, and run Ic was during the winter of 1995–1996. The total integrated luminosity for Run I was about 130 pb^{-1}.

The instantaneous luminosity L was determined from the counting rate in the Level 0 hodoscopes ($\mathcal{R}_{L0}$) as:

$$L = \frac{-ln(1 - \tau\mathcal{R}_{L0})}{\tau\sigma_{L0}} \tag{4.3}$$

where $\tau = 3.5\ \mu s$ is the time interval between beam crossings and σ_{L0} is the effective $p\bar{p}$ cross section subtended by the Level 0 counters, and was obtained to be 43.1 ± 1.9 mb, as described in detail in Ref. [34].

The integrated luminosity seen by each of the triggers is given in the second column, labelled 'exposure', of Tables 4.1–4.3. At high luminosity, some of the triggers were scaled down by a pre-determined factor, in order to maintain a sensible data recording rate. Differing requirements were also used to veto possible Main Ring events, details of which can be found in Ref. [23]. The 'exposure' column in the tables takes into account the prescale factors (if appropriate) as well as the losses due to Main Ring vetos.

After triggering (filtering) the events in the $e + jets$, $\mu + jets$, $e + jets/\mu$,

Table 4.1: Triggers used during run Ia (1992–1993). "Exposure" gives the effective integrated luminosity for each trigger, taking into account any prescaling.

Name	Exposure (pb^{-1})	Level 1	Level 2	Used by
ELE-HIGH	11.0	1 EM tower, $E_T > 10$ GeV	1 isolated e, $E_T > 20$ GeV	$e +$ jets
ELE-JET	14.4	1 EM tower, $E_T > 10$ GeV, $\|\eta\| < 2.6$ 2 jet towers, $E_T > 5$ GeV	1 e, $E_T > 15$ GeV, $\|\eta\| < 2.5$ 2 jets ($\Delta R = 0.3$), $E_T > 10$ GeV, $\|\eta\| < 2.5$ $\not\!\!E_T^{\rm cal} > 10$ GeV	$e +$ jets $e +$ jets/μ
MU-JET-HIGH	10.2	1 μ, $\|\eta\| < 2.4$ 1 jet tower, $E_T > 5$ GeV	1 μ, $p_T > 8$ GeV/c 1 jet ($\Delta R = 0.7$), $E_T > 15$ GeV	$\mu +$ jets $\mu +$ jets/μ

and $\mu + jets/\mu$ channels, the identification of electrons, muons, neutrinos, and jets is improved by applying the criteria discussed in Sections 3.3-3.6.

4.2 Principal sources of background

In our search for $X \to t\bar{t}$ with lepton plus jets in the final state, the 'background' sources that could result in the same final state, are (a) Standard Model $t\bar{t}$ production, and (b) non–$t\bar{t}$ sources, of which the following two sources would make a substantial contribution:

- Production of a W boson[1] in association with the requisite number of jets with the W boson decaying into a lepton and its corresponding neutrino.

- Production of multijets ($N_j \sim 5$), in which one of the jets is misidentified as a lepton, and instrumental effects simulate sufficient $\not\!\!E_T$ that satisfies the neutrino requirement.

[1] W boson production proceeds mainly through $q\bar{q}$ annihilation.

Table 4.2: Same as Table 4.1 for run Ib (1994–1995).

Name	Exposure (pb^{-1})	Level 1	Level 2	Used by
EM1-EISTRKCC-MS	93.4	1 EM tower, $E_T > 10$ GeV 1 EX tower, $E_T > 15$ GeV	1 isolated e w/track, $E_T > 20$ GeV $\not\!\!E_T^{\rm cal} > 15$ GeV	e + jets
ELE-JET-HIGH	98.0	1 EM tower, $E_T > 12$ GeV, $\|\eta\| < 2.6$ 2 jet towers, $E_T > 5$ GeV, $\|\eta\| < 2.0$	1 e, $E_T > 15$ GeV, $\|\eta\| < 2.5$ 2 jets ($\Delta R = 0.3$), $E_T > 10$ GeV, $\|\eta\| < 2.5$ $\not\!\!E_T^{\rm cal} > 14$ GeV	e + jets e + jets/μ
MU-JET-HIGH	66.4	1 μ, $p_T > 7$ GeV/c, $\|\eta\| < 1.7$ 1 jet tower, $E_T > 5$ GeV, $\|\eta\| < 2.0$	1 μ, $p_T > 10$ GeV/c, $\|\eta\| < 1.7$ 1 jet ($\Delta R = 0.7$), $E_T > 15$ GeV, $\|\eta\| < 2.5$	μ + jets μ + jets/μ
MU-JET-CAL	88.0	1 μ, $p_T > 7$ GeV/c, $\|\eta\| < 1.7$ 1 jet tower, $E_T > 5$ GeV, $\|\eta\| < 2.0$	1 μ, $p_T > 10$ GeV/c, $\|\eta\| < 1.7$ cal confirm, scint 1 jet ($\Delta R = 0.7$), $E_T > 15$ GeV, $\|\eta\| < 2.5$	μ + jets μ + jets/μ
MU-JET-CENT	48.5	1 μ, $\|\eta\| < 1.0$ 1 jet tower, $E_T > 5$ GeV, $\|\eta\| < 2.0$	1 μ, $p_T > 10$ GeV/c, $\|\eta\| < 1.0$, scint 1 jet ($\Delta R = 0.7$), $E_T > 15$ GeV, $\|\eta\| < 2.5$	μ + jets μ + jets/μ
MU-JET-CENCAL	51.2	1 μ, $\|\eta\| < 1.0$ 1 jet tower, $E_T > 5$ GeV, $\|\eta\| < 2.0$	1 μ, $p_T > 10$ GeV/c, $\|\eta\| < 1.0$ cal confirm, scint 1 jet ($\Delta R = 0.7$), $E_T > 15$ GeV, $\|\eta\| < 2.5$	μ + jets μ + jets/μ
JET-3-MU	11.9	3 jet towers, $E_T > 5$ GeV $\not\!\!E_T^{\rm cal} > 20$ GeV	3 jets ($\Delta R = 0.7$), $E_T > 15$ GeV, $\|\eta\| < 2.5$ $\not\!\!E_T^{\rm cal} > 17$ GeV	μ + jets μ + jets/μ
JET-3-MISS-LOW	57.8	3 large tiles, $E_T > 15$, $\|\eta\| < 2.4$ 3 jet towers, $E_T > 7$ GeV, $\|\eta\| < 2.6$	3 jets ($\Delta R = 0.5$), $E_T > 15$ GeV, $\|\eta\| < 2.5$ $\not\!\!E_T^{\rm cal} > 17$ GeV	μ + jets μ + jets/μ
JET-3-L2MU	25.8	3 large tiles, $E_T > 15$, $\|\eta\| < 2.4$ 3 jet towers, $E_T > 7$ GeV, $\|\eta\| < 2.6$	1 μ, $p_T > 6$ GeV/c, $\|\eta\| < 1.7$ cal confirm, scint 3 jets ($\Delta R = 0.5$), $E_T > 15$ GeV, $\|\eta\| < 2.5$ $\not\!\!E_T^{\rm cal} > 17$ GeV	μ + jets μ + jets/μ

Monte Carlo simulation is used to model the final states expected from the signal ($X \to t\bar{t}$) and the principal physics backgrounds. The simulation of signal events will be discussed in chapter 6. For the background sources, we use the samples that were generated for the measurement of the top quark mass at DØ. A brief discussion of these samples is given below; further details can be found in Ref. [33].

The Standard Model $t\bar{t}$ production was modelled using the HERWIG Monte Carlo generator (version 5.7) with CTEQ3M [35] parton distribution functions. Events were generated with a top quark mass of 175 GeV/c^2. Initial and final state gluon emission, and underlying spectator interactions were included in the model. To increase the efficiency in the processing of lepton plus jets

Table 4.3: Same as Table 4.1 for run Ic (1995–1996).

Name	Exposure (pb^{-1})	Level 1	Level 2	Used by
ELE-JET-HIGH	1.9	1 EM tower, $E_T > 12\,\text{GeV}$, $\lvert\eta\rvert < 2.6$ 2 jet towers, $E_T > 5\,\text{GeV}$, $\lvert\eta\rvert < 2.0$	1 e, $E_T > 15\,\text{GeV}$, $\lvert\eta\rvert < 2.5$ 2 jets ($\Delta R = 0.3$), $E_T > 10\,\text{GeV}$, $\lvert\eta\rvert < 2.5$ $\not\!\!E_T^{\text{cal}} > 14\,\text{GeV}$	$e + \text{jets}/\mu$
ELE-JET-HIGHA	11.0	1 EM tower, $E_T > 12\,\text{GeV}$, $\lvert\eta\rvert < 2.6$ 2 jet towers, $E_T > 5\,\text{GeV}$, $\lvert\eta\rvert < 2.0$ 1 EX tower, $E_T > 15\,\text{GeV}$	1 e, $E_T > 17\,\text{GeV}$, $\lvert\eta\rvert < 2.5$ 2 jets ($\Delta R = 0.3$), $E_T > 10\,\text{GeV}$, $\lvert\eta\rvert < 2.5$ $\not\!\!E_T^{\text{cal}} > 14\,\text{GeV}$	$e + \text{jets}/\mu$

events, one of the W bosons was forced to decay to one of the three lepton families. Events with no final state electrons or muons were vetoed, and half of the events in which both W bosons decayed leptonically were discarded in order to preserve the proper branching ratios. The generated events were run through the DØGEANT detector simulation and the DØ event reconstruction program.

The background due to the production of a W boson with multiple jets was modelled using the VECBOS [36] event generator, also with CTEQ3M parton distribution functions. The dynamical scale of the process was set to be the average jet p_T. To include the effects of additional radiation and underlying processes, and to model the hadronization of final state partons, the output of VECBOS was passed through the HERWIG QCD evolution and fragmentation stages. The generated events were run through detector simulation and event reconstruction in the same manner as for the Standard Model $t\bar{t}$ production.

The (QCD) multijet background was estimated using background-enriched data samples. In the electron channels, the sample consisted of events containing highly electromagnetic clusters that satisfied electron trigger requirements, but failed the offline electron identification criteria. In the muon channels,

events containing a muon that failed the isolation requirement, but which passed all other muon identification requirements, were selected for background study.

The energy corrections to electromagnetic objects and the 'standard' corrections to the jet energies were applied using a standard DØ program: CAFIX 5.0. This program also recalculates $\not\!\!E_T$ using the corrected energies of jets and electromagnetic objects.

For the measurement of the top quark mass using Standard Model $t\bar{t}$ production as the source of signal, most selections were optimized to reduce the contribution from non-$t\bar{t}$ sources. We use similar selections in the present analysis also. A brief discussion of these criteria is given below.

4.3 Selection Criteria

4.3.1 Topological analysis

The purely topological analysis relies on the following requirements ('preselections') to separate $t\bar{t}$ events from the non–$t\bar{t}$ background:

- An event must contain either an electron with $E_T > 20$ GeV within $|\eta| < 2.0$, or an isolated muon[2] with $p_T > 20$ GeV/c within $|\eta| < 1.7$.

- It must have significant missing transverse energy: $\not\!\!E_T > 20$ GeV. The missing transverse energy based purely on the calorimeter ($\not\!\!E_T^{\rm cal}$) should

[2]A muon is called "isolated" if its distance $\Delta R(\mu, j) \equiv ((\Delta\phi)^2 + (\Delta\eta)^2)^{\frac{1}{2}} > 0.5$ from every jet in the event.

be > 25 GeV for e+jets and should be > 20 GeV for μ+jets events.

- It must have at least 4 jets with $E_T > 15$ GeV, all within $|\eta| < 2.0$.
- None of the jets in the event must have a muon tag.
- The W boson reconstructed from the lepton and the missing transverse energy must be contained within the central pseudorapidity region of $|\eta^W| < 2.0$, and the scalar sum of the lepton transverse momentum and the missing transverse energy must exceed 60 GeV ($E_T^W \equiv p_T^{lep} + \not\!\!E_T > 60$ GeV).

The cut on E_T^W removes a portion of the QCD multijet background. Figure 4.2 compares the E_T^W distribution for this background to that from Monte Carlo $W +$ jets events.

In Figure 4.3, we show the distributions of $|\eta^W|$ [33] for data and for the Monte Carlo prediction. The data are seen to significantly exceed the prediction of the VECBOS Monte Carlo in the far forward region. We note that the VECBOS Monte Carlo, while the best currently available, is only a tree-level calculation of the $W +$ jets process. Particularly in the forward direction, one would expect higher order corrections to play a larger role. To mitigate the effects of this discrepancy, and to further reduce the non–$t\bar{t}$ background (since the amount of $t\bar{t}$ signal with $|\eta^W| > 2$ is only $\approx 3\%$ for $m_t = 175\,\mathrm{GeV}/c^2$), we require $|\eta^W| < 2$.

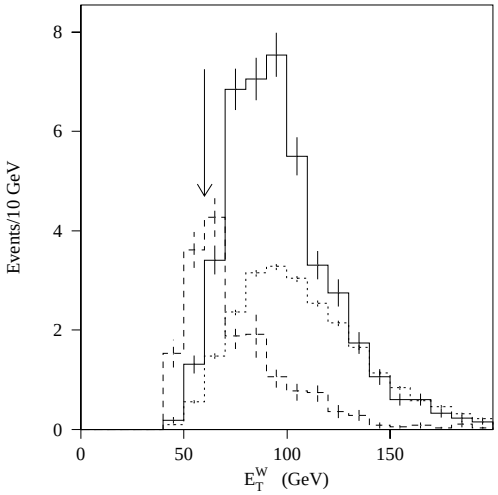

Figure 4.2: E_T^W distribution for Monte Carlo W+jets events (solid histogram), QCD multijet background data (dashed histogram), and $t\bar{t}$ signal with $m_t = 175\,\mathrm{GeV}/c^2$ (dotted histogram) [33]. All preselections are applied except for the E_T^W cut. The arrow shows the cut value.

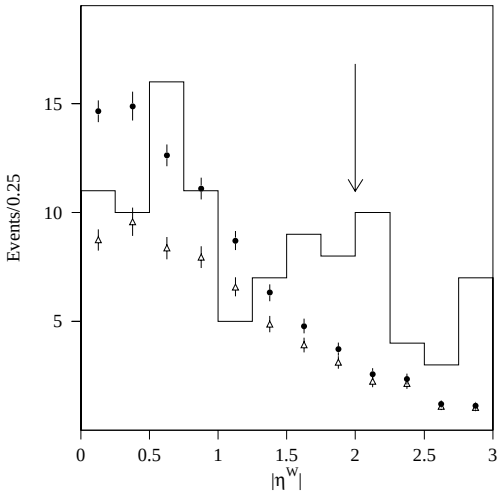

Figure 4.3: $|\eta^W|$ distribution for data (histogram), predicted Standard Model $t\bar{t}$ plus non–$t\bar{t}$ background (filled circles), and non–$t\bar{t}$ background alone (open triangles). All preselections are applied except for the η^W cut. The arrow shows the cut value.

4.3.2 Tag analysis

The probability that a $t\bar{t}$ event contains at least one tagging muon from the semi-leptonic decay of the b-jet is about 44%. These tag muons can be detected at DØ with an efficiency of about 45%. So the probability for observing a muon-tagged b-jet in a $t\bar{t}$ event at DØ is about 20%. Since the principal source of non-$t\bar{t}$ background is due to W + jets production, and the fraction of $W + \geq 3$ jets events with a muon passing the tagging criterion is only about 2% [37], the tagging requirement offers about an order of magnitude reduction in the non–$t\bar{t}$ background. An event must meet the following requirements in order to be accepted in the tagged channels:

- It must contain either an electron with $E_T > 20$ GeV within $|\eta| < 2.0$, or an isolated muon with $p_T > 20$ GeV/c within $|\eta| < 1.7$.

- It must have significant missing transverse energy: $\not\!\!E_T > 20$ GeV, and $\not\!\!E_T^{\rm cal} > 20$ GeV for μ+jets/μ events.

- It must have at least 4 jets with $E_T > 15$ GeV within $|\eta| < 2.0$.

- At least one of the jets must have a muon tag. A jet is "μ-tagged" if there is an associated non-isolated muon[3] with $p_T > 4$ GeV/c.

- For e+jets/μ events, $\not\!\!E_T$ must be > 35 GeV, if $\Delta\phi(\not\!\!E_T, \mu) < 25°$. For μ+jets/μ events, $\Delta\phi(\not\!\!E_T, \mu)$ must be $< 170°$, and $|\Delta\phi(\not\!\!E_T, \mu)$ - 90°| /

[3]A muon is called "non-isolated" if the distance $\Delta R(\mu, j) \equiv ((\Delta\phi)^2 + (\Delta\eta)^2)^{\frac{1}{2}} < 0.5$ for any jet in the event.

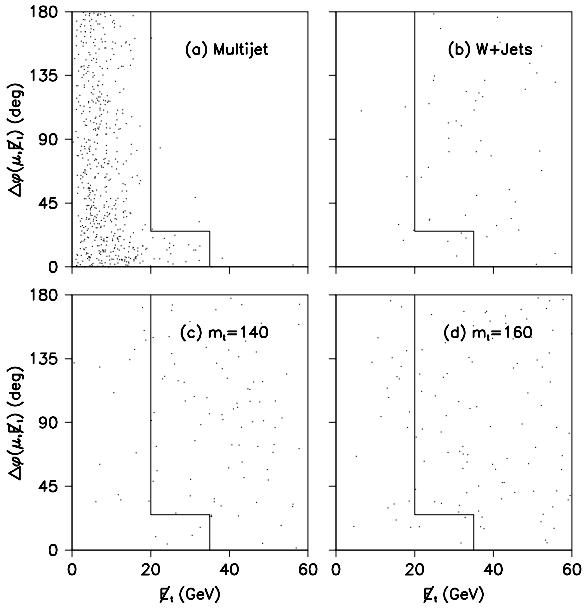

Figure 4.4: Distribution of $\Delta\phi(\not\!\!E_T, \mu)$ vs. $\not\!\!E_T$ for e + jets/μ events for (a) multijet background sample; (b) W + jets sample (VECBOS Monte Carlo); (c) Standard Model (SM) $t\bar{t}$ Monte Carlo (ISAJET, m_t = 140 GeV/c^2); (d) SM $t\bar{t}$ Monte Carlo (ISAJET, m_t = 160 GeV/c^2). The contour shows the cut values.

$90° < \not\!\!E_T/(45\text{ GeV})$. Here $\Delta\phi(\not\!\!E_T, \mu)$ is the difference in the azimuthal angle between the $\not\!\!E_T$ and the highest-p_T muon.

The motivation for the complicated missing $\not\!\!E_T$ criteria is to obtain good rejection of the QCD multijet background. This can be seen from Figs. 4.4 and 4.5, in which the correlation between $\not\!\!E_T$ and $\Delta\phi(\not\!\!E_T,\mu)$ for the non-$t\bar{t}$ background and Standard Model $t\bar{t}$ production, is shown for the e+jets/μ and μ+jets/μ events, respectively [30]. The Standard Model $t\bar{t}$ events for this study were generated using the ISAJET [38] Monte Carlo event generator.

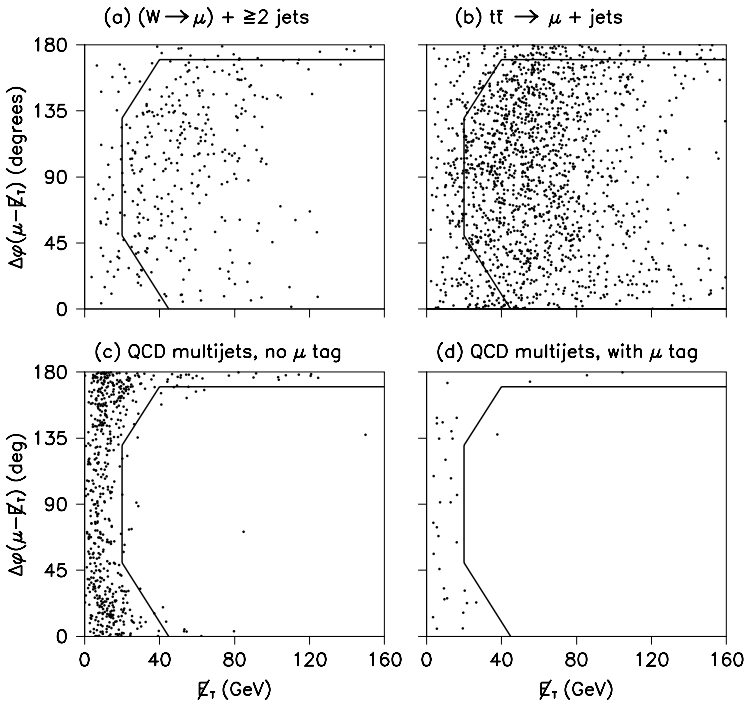

Figure 4.5: The correlation between $\not\!\!E_T$ and the azimuthal angle between $\not\!\!E_T$ and the highest-p_T muon for μ + jets/μ events for (a) VECBOS W + jets Monte Carlo ($\int \mathcal{L}dt$ = 80 pb^{-1}); (b) ISAJET SM $t\bar{t}$ Monte Carlo (m_t = 160 GeV/c^2, 3240 pb^{-1}); (c) multijet events with a non-isolated high-p_T muon with no μ–tag; (d) multijet events with a non-isolated high-p_T muon with an additional tagging muon.

Table 4.4: Summary of event selections ('preselections')

	e+jets	μ+jets	e+jets/μ	μ+jets/μ
Lepton	E_T >20 GeV	p_T >20 GeV/c	E_T >20 GeV	p_T >20 GeV/c
(l)	$\|\eta\|$ <2	$\|\eta\|$ <1.7	$\|\eta\|$ <2	$\|\eta\|$ <1.7
$\not\!\!E_T$	$\not\!\!E_T$ >20 GeV	$\not\!\!E_T$ >20 GeV	$\not\!\!E_T$ >20 GeV	$\not\!\!E_T$ >20 GeV
	$\not\!\!E_T^{cal}$ >25 GeV	$\not\!\!E_T^{cal}$ >20 GeV		$\not\!\!E_T^{cal}$ >20 GeV
Jets	$\geq$ 4 jets	$\geq$ 4 jets	$\geq$ 4 jets	$\geq$ 4 jets
	E_T >15 GeV	E_T >15 GeV	E_T >15 GeV	E_T >15 GeV
	$\|\eta\|$ <2	$\|\eta\|$ <2	$\|\eta\|$ <2	$\|\eta\|$ <2
μ tag	No	No	Yes	Yes
Other	E_T^W >60 GeV	E_T^W >60 GeV	$\not\!\!E_T$ >35 GeV	$\Delta\phi(\not\!\!E_T, \mu) < 170°$,
	$\|\eta^W\|$ <2	$\|\eta^W\|$ <2	if $\Delta\phi(\not\!\!E_T, \mu) < 25°$	$\frac{\|\Delta\phi(\not\!\!E_T,\mu)-90°\|}{90°} < \frac{\not\!\!E_T}{45GeV}$
Events passing cuts	42	41	4	3
with $\chi^2 < 10$	16	21	1	3

A summary of the event selections (preselections) for the four channels is given in Table 4.4. When applied to the approximately 130 pb^{-1} of data from the 1992-1996 Tevatron runs, the preselections yield 90 events, seven of which have a tagging muon[4].

[4]An additional requirement is made to define the final sample. This is based on the χ^2 of a kinematic fit to the $t\bar{t}$ decay hypothesis discussed in chapter 5.

Chapter 5

Kinematic fit

After applying the preselections discussed in chapter 4, and reducing the contamination from non-$t\bar{t}$ sources in the lepton + jets final state, we next reconstruct the invariant mass ($m_{t\bar{t}}$) of the $t\bar{t}$ pair in a $t\bar{t} \rightarrow l$ + jets decay. Unfortunately there is not a unique prescription for accomplishing this.

If the correspondence between jets and partons were known, one could simply sum them up in the appropriate combinations to obtain the invariant mass of the $t\bar{t}$ pair. But, in general, this is not known. For example, in case of four jets in the final state, there are twelve possible jet-parton assignments: there are twenty-four permutations of four objects, but the two jets which are assigned to the hadronic W boson can be interchanged without changing the solution, so only twelve of them are distinct. There can be additional jets due to initial state and final state QCD radiation, and as the number of jets in the final state increases, the number of possible jet-parton assignments shows a sharp increase (see appendix A for details).

Even if the jet-parton assignment were known, the measurement uncertainties in the kinematic parameters of the final-state objects may give significant error in the determination of $m_{t\bar{t}}$. We therefore perform a kinematic fit to constrain the measured variables in the event to the hypothesis:

$$p\bar{p} \to t\bar{t} + ... \to (W^+b)(W^-\bar{b}) + ... \to (l\nu b)(q\bar{q}\bar{b}) + ... \tag{5.1}$$

(or the charge conjugate). We define a χ^2 which tells us how far the kinematic parameters of the event must be pulled from their measured values in order for certain constraint equations to be satisfied. Each of the possible jet-parton assignments can be tried, and the permutation which results in the lowest value for the χ^2 can be used as an estimate of $m_{t\bar{t}}$. The kinematic parameters used and the method of constrained fit are discussed in the following section.

5.1 Constrained Fit

The first thing to do is to define the variables which will be used in the fit. It is convenient to choose them so that they are as uncorrelated as possible. For the lepton and each jet, there are three measured variables: its energy (or momentum), and its direction (which is a two dimensional quantity). The variables which will be used to describe an electron or jet are its momentum p, azimuthal angle ϕ, and pseudorapidity η. Muons are described in a similar manner, except that instead of p, the inverse momentum $k = 1/p$ is used, since the errors are more nearly Gaussian in that variable. The masses of the jets are fixed to zero, except for the jets which are assigned as b-jets, which are

given masses[1] of $5\,\mathrm{GeV}/c^2$.

To represent the transverse momentum of the neutrino, one could use the x and y components of the missing E_T. However, that is not ideal, since the missing E_T is highly correlated with all the other energy measurements: a fluctuation in jet measurement will show up as an exactly corresponding fluctuation in the missing E_T. A better quantity is k_T, which is defined as

$$\vec{k_T} = \vec{E}_T(\mathrm{lep}) + \vec{\not{E}}_T + \sum_{i \in \mathrm{jets}} \vec{E}_T(\mathrm{jet}_i). \tag{5.2}$$

The sum over jets here includes only jets assumed to be part of the final state. This variable can be interpreted as the transverse momentum of the $t\bar{t}$ system. The x and y components of $\vec{k_T}$ are used as fit variables.

There is one remaining variable, which is taken to be the z-component of the neutrino momentum (p_z^ν). This variable is not measured but is determined from the fit, as will be discussed in Section 5.2. Thus, we have a total of eighteen variables (for $l\nu$ + 4 jets final state). Each measured variable still needs to have an error attached to it; this will be discussed in Section 5.3.

We next form the fit variables into a one-dimensional vector $\mathbf{x}$, and define a χ^2 as

$$\chi^2 = (\mathbf{x} - \mathbf{x}^m)^T \mathbf{G} (\mathbf{x} - \mathbf{x}^m), \tag{5.3}$$

where $\mathbf{x}$ is the vector of fit-variables, $\mathbf{x}^m$ is the vector of the measured values of those variables, and $\mathbf{G}$ is the inverse error matrix. This quantity should be

[1]This is done by taking the momentum components of the jet as the measurement, and changing the energy component of the four-vector to set the desired mass. Since these masses are small compared to the typical jet energies ($> 15\,\mathrm{GeV}$), the exact prescription used doesn't make much difference for the final result.

minimized subject to the constraints

$$m(l\nu) = M_W = 80.2\,\mathrm{GeV}/c^2 \tag{5.4}$$

$$m(q\bar{q}') = M_W \tag{5.5}$$

$$m(t) = 173.3^2\,\mathrm{GeV}/c^2 \tag{5.6}$$

$$m(t \to l\nu b) = m(\bar{t} \to q\bar{q}'\bar{b}). \tag{5.7}$$

The minimization algorithm uses the method of Lagrange multipliers; the non-linear constraint equations are solved using an iterative technique. Details of the minimization algorithm can be found in Ref. [30].

To keep the problem simple, we consider only the four highest E_T jets in the final state. Since we do not know the correspondence between the jets and partons, we try all the twelve[3] distinct assignments of the four jets to the four partons ($b\bar{b}q\bar{q}'$). Once a permutation is chosen, we apply the parton-level and η dependent jet energy corrections, before the fit. We also apply a loose cut on the mass of the hadronically decaying W boson of $40 < \mathrm{m}(q\bar{q}') < 140$ GeV/c^2. Permutations failing this criterion are rejected so as to speed up the computation. For each surviving permutation, we then minimize the χ^2, subject to the constraint equations defined above. If the minimization does not converge, the permutation is rejected. The permutation which results in

[2]The widths of the W boson ($\Gamma_W \sim 2$ GeV/c^2) and the top quark ($\Gamma_t \sim 1.5$ GeV/c^2) are small compared to the experimental resolutions, and hence, neglecting them, does not seriously alter the results of the constrained fit.
The chosen value of m_t is a result of a measurement at DØ using the lepton plus jets final state.

[3]There are six distinct jet-parton assignments in events with a μ–tagged b–jet.

the lowest χ^2 is called the 'best' permutation. We use the fitted values of the variables corresponding to the 'best' permutation, to compute the invariant mass ($m_{t\bar{t}}$) of the $t\bar{t}$ pair.

5.2 Determination of p_z^ν

In order to start the above procedure, one must specify an initial value for *all* variables — not just the measured ones. In particular, a starting value is needed for the z-component of the neutrino momentum, p_z^ν. This is done by choosing it such that the two top quarks have equal mass. This yields the following quadratic equation for p_z^ν:

$$\left((p_z^c)^2 - (E^c)^2\right)(p_z^\nu)^2 + \alpha p_z^c p_z^\nu - (E^c p_T{}^\nu)^2 + \alpha^2/4 = 0, \tag{5.8}$$

where

$$\alpha = m_t^2 - m_c^2 + 2\vec{p_T}{}^\nu \cdot \vec{p_T}{}^c, \tag{5.9}$$

and the four-vector c is the sum of the four-vectors of the lepton and b-jet. If the solutions are complex, the real part is used. Otherwise, there will be two real solutions. Both are tried, and the fit with the lowest χ^2 is retained.

5.3 Error matrix G

The resolutions used for the different final state objects are listed in Table 5.1. These resolutions were derived using Standard Model $t\bar{t}$ Monte Carlo events, by comparing the reconstructed objects (after detector simulation) to

Table 5.1: Object resolutions. The operator $\oplus$ denotes a sum in quadrature.

	Energy resolution	$\sigma(\phi)$	$\sigma(\eta)$
Electrons	$\sigma(E_T)/E_T = 0.0157 \oplus 0.072\,\mathrm{GeV}^{1/2}/\sqrt{E_T} \oplus 0.66\,\mathrm{GeV}/E_T$	$\sim$0	$\sim$0
Muons	$\sigma(1/p) = C^a \oplus 0.2/p$	$\sim$0	$\sim$0
Jets			
$0 < \lvert\eta^{\mathrm{det}}\rvert < 0.8$	$\sigma(E)/E = 0.036 \oplus 1.145\,\mathrm{GeV}^{1/2}/\sqrt{E}$	0.04 rad	0.04
$0.8 < \lvert\eta^{\mathrm{det}}\rvert < 1.4$	$\sigma(E)/E = 0.082 \oplus 1.264\,\mathrm{GeV}^{1/2}/\sqrt{E}$	0.05 rad	0.05
$1.4 < \lvert\eta^{\mathrm{det}}\rvert < 2.0$	$\sigma(E)/E = 0.046 \oplus 1.305\,\mathrm{GeV}^{1/2}/\sqrt{E}$	0.05 rad	0.05
k_T	$\sigma(k_{Tx}) = \sigma(k_{Ty}) = 12\,\mathrm{GeV}$		

[a] C = 0.0045/(GeV/c) if the muon track could be matched with a track in the central detector;
C = 0.01/(GeV/c) otherwise.

generator-level objects [39]. The lepton angular resolutions are much smaller than the other resolutions, and are therefore considered to be zero. All errors are assumed to be uncorrelated (*ie.*, **G** is a diagonal matrix).

5.4 Results from the kinematic fit

In Figure 5.1, the χ^2 distribution for 3 degrees of freedom and the χ^2 (after preselections) for the **correct** jet-parton permutation in the $e + jets$ channel for Standard Model $t\bar{t}$ production, are shown. The χ^2 distributions for the correct jet-parton assignment ($\chi^2_{correct}$) for the $\mu + jets$, $e + jets/\mu$, and $\mu + jets/\mu$ channels have also been studied [33]. The fraction of Standard Model $t\bar{t}$ events in all channels is found to be small for $\chi^2_{correct} > 10$. The χ^2 distributions (after preselections) for the 'best' permutation in case of data,

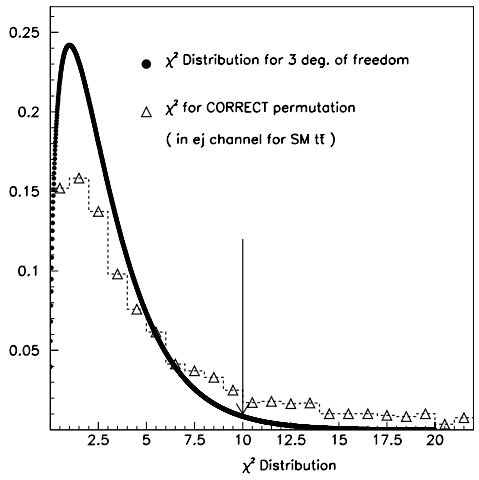

Figure 5.1: χ^2 distribution for 3 degrees of freedom and the χ^2 distribution (normalized to unity after preselections) for the **correct** jet-parton permutation in the $e + jets$ channel for Standard Model $t\bar{t}$ production. It can be seen that there are very few events beyond $\chi^2 = 10$ indicated by the arrow.

Standard Model $t\bar{t}$ production, W+jets, and multijets, are shown in Figure 5.2. The corresponding distributions for the different resonance masses, M_X, are shown in Figs. 5.3-5.7. We observe that the fraction of preselected events that survive the $\chi^2 < 10$ cut, in case of $t\bar{t}$ events, is between 0.7-0.8; the fraction of preselected events that are eliminated by the $\chi^2 < 10$ cut, in case of the non-$t\bar{t}$ background sources, is about 0.6.

Based on the above studies, we apply an additional cut of $\chi^2 < 10$ in order to reduce the chances of picking up a wrong jet-parton assignment as the 'best' permutation, as well as, to enhance the selection of $t\bar{t}$ events (in data) over the non-$t\bar{t}$ background. As a result, 41 events are left in the data sample of which 4 are μ-tagged.

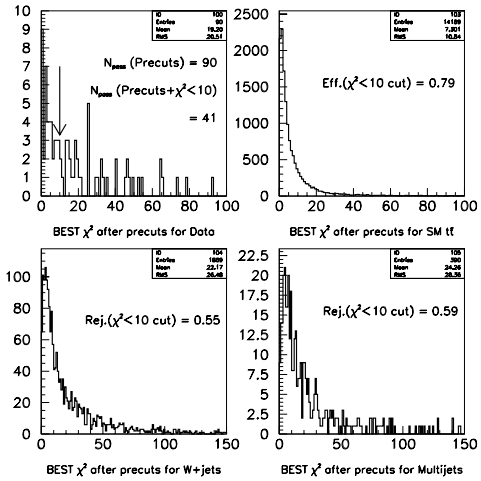

Figure 5.2: χ^2 for the **best** permutation for DØ Run I lepton+jets data, Standard Model $t\bar{t}$ production, W+jets and multijets backgrounds. Preselections are applied and the contents in all four channels (ej, ej/μ, μj, $\mu j/\mu$) are added. *Efficiency* is defined as the fraction of preselected events that remain after the $\chi^2 < 10$ cut. *Rejection* is defined as the fraction of preselected events that are eliminated by the $\chi^2 < 10$ cut.

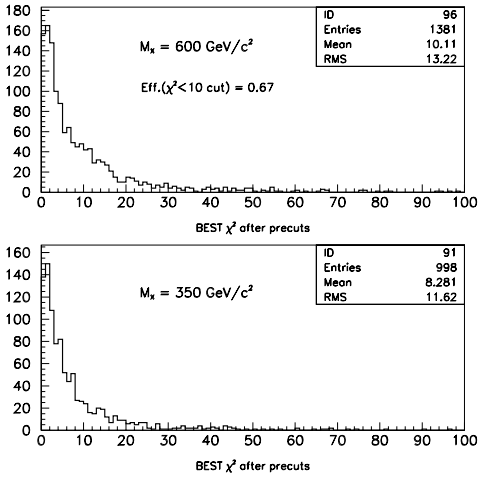

Figure 5.3: χ^2 distribution for X $\rightarrow t\bar{t}$ at $M_X = 600$ GeV/c^2 and 350 GeV/c^2. Preselections are applied and the contents in all four channels (ej, ej/μ, μj, $\mu j/\mu$) are added.

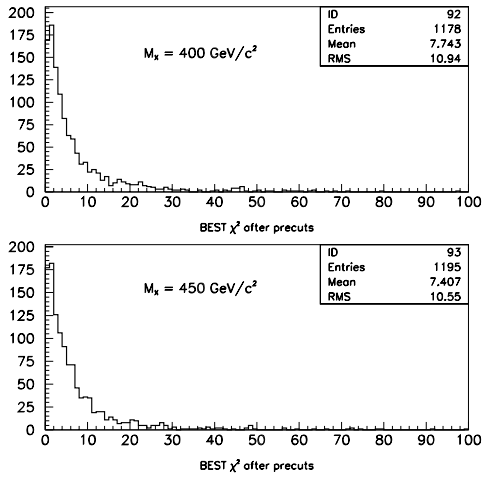

Figure 5.4: χ^2 distribution for X $\rightarrow t\bar{t}$ at $M_X = 400$ GeV/c^2 and 450 GeV/c^2. Pre-selections are applied and the contents in all four channels (ej, ej/μ, μj, $\mu j/\mu$) are added.

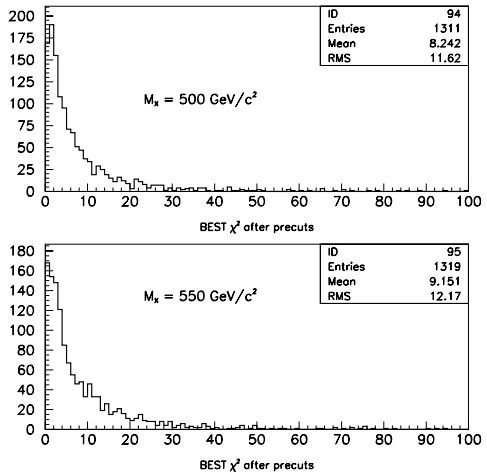

Figure 5.5: χ^2 distribution for X $\rightarrow t\bar{t}$ at $M_X = 500$ GeV/c^2 and 550 GeV/c^2. Pre-selections are applied and the contents in all four channels (ej, ej/μ, μj, $\mu j/\mu$) are added.

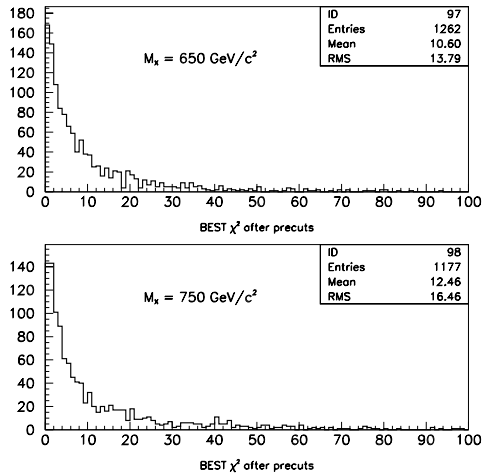

Figure 5.6: χ^2 distribution for X $\rightarrow t\bar{t}$ at $M_X = 650$ GeV/c^2 and 750 GeV/c^2. Pre-selections are applied and the contents in all four channels (ej, ej/μ, μj, $\mu j/\mu$) are added.

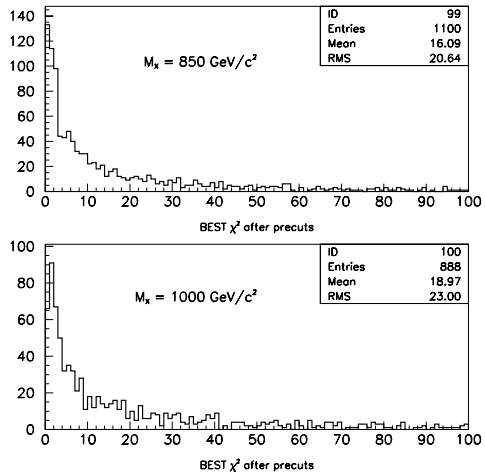

Figure 5.7: χ^2 distribution for X $\rightarrow t\bar{t}$ at $M_X = 850$ GeV/c^2 and 1000 GeV/c^2. Pre-selections applied and the contents in all four channels (ej, ej/μ, μj, $\mu j/\mu$) are added.

Chapter 6

Event simulation

After reconstructing the top-antitop invariant mass, we next need to study the observed $m_{t\bar{t}}$ distribution and see if there is any evidence of a resonance signal $X \to t\bar{t}$. To do this, we simulate the signal ($X \to t\bar{t}$) events at different resonance masses, M_X, and perform a statistical analysis to see which resonance mass M_X (if any), along with the expected background sources, best corresponds to the observed $m_{t\bar{t}}$ spectrum. The expected sources of background in the lepton plus jets final state were discussed in chapter 4. Here we discuss the simulation of signal ($X \to t\bar{t}$) events at different M_X.

We model the resonance signal $X \to t\bar{t}$ using the Pythia Monte Carlo generator (Version 6.1) [40] with CTEQ3M parton distribution functions and a top mass of 175 GeV/c^2. We include the initial and final state QCD radiation, and generate about 10,000 events at ten different masses of X, between 350 GeV/c^2 and 1000 GeV/c^2. We use a width of $\Gamma_X = 0.012\ M_X$ for the resonance X. This qualifies X as a narrow resonance since its width is significantly smaller than the mass resolution of the DØ detector for $t\bar{t}$ systems which

is estimated to be about 4% of M_X [41]. To increase the efficiency in the processing of lepton plus jets events, we force one of the W bosons to decay to one of the three lepton families (e, μ or τ). A list of the main parameters used in Pythia is provided below, for $M_X = 600$ GeV/c^2.

- pmas(6,1)=175 : this sets the top mass to 175 GeV/c^2
- pmas(32,1)=600 : this sets M_X to 600 GeV/c^2
- mstp(51)=2 : the CTEQ3M parton distribution functions are used
- mstp(151)=1, parp(153)=30 : this smears the z-component of the interaction vertex with a resolution of $\pm$30 cm.
- paru(121)=-0.416, paru(122)=-0.6, paru(123)=0.232, paru(124)=0.6, paru(125)=-0.048, paru(126)=-0.6, paru(127)=0.6, paru(128)=0.6 : vector and axial couplings of X to first generation quarks and leptons[1]
- parj(180)=-0.416, parj(181)=-0.6, parj(182)=0.232, parj(183)=0.6, parj(184)=-0.048, parj(185)=-0.6, parj(186)=0.6, parj(187)=0.6 : vector and axial couplings of X to second generation quarks and leptons
- parj(188)=-0.416, parj(189)=-0.6, parj(190)=0.232, parj(191)=0.6, parj(192)=-0.048, parj(193)=-0.6, parj(194)=0.6, parj(195)=0.6D0 : vector and axial couplings of X to third generation quarks and leptons

[1]In Pythia the default setting for the couplings of the X boson to quarks and leptons is the same as that for the Standard Model Z boson. In the present analysis we change these couplings and set them such that the width of the resonance, Γ_X, which depends quadratically on them, is $0.012 M_X$.

- msub(141)= 1 : this selects the process $f_i\bar{f}_i \rightarrow \gamma/Z^0/X$
- mstp(44) = 3 : only the X-boson is considered in the matrix elements
- mstp(111) = 1 : fragmentation and decay is switched on
- mstp(61) = 1 : initial state QCD and QED radiation is switched on
- mstp(71) = 1 : final state QCD and QED radiation is switched on
- mstp(81) = 0 : multiple interactions are switched off
- ckin(1) = 300, ckin(2) = 2000 : the invariant mass of $t\bar{t}$ varies between 300-2000 GeV/c^2
- mdme(294,1) = 1 : **only** the $t\bar{t}$ decay mode is allowed for X boson
- mdme(190,1) = 2, mdme(191,1) = 2, mdme(192,1) =2, mdme(194,1) = 2, mdme(195,1) = 2, mdme(196,1) = 2, mdme(198,1) = 2, mdme(199,1) = 2, mdme(200,1) = 2 : the hadronic decay modes are allowed *only* for W^+, and not for W^-
- mdme(206,1) = 1, mdme(207,1) = 1, mdme(208,1) = 1 : the leptonic decay modes are allowed for **both** W^+ and W^-.

We process the entire set of generated events through the DØGEANT detector simulation package. DØGEANT does not contain an accurate representation of the plane efficiencies for each of the 144 WAMUS proportional drift tubes. We therefore correct the raw Monte Carlo hits in the output of DØGEANT according to the measured muon hit-finding efficiencies. This is done using a software

package called "mu-smear". Details of measurements of the chamber efficiencies can be found in [42, 43]. We finally reconstruct the mu-smeared events using the DØ event reconstruction program. We then apply the standard corrections to electromagnetic objects, jets and $\not\!\!E_T$, and the same preselections as for the data sample to each of the signal and background samples. We next perform the kinematic fit described in chapter 5 to construct the top-antitop invariant mass and apply the $\chi^2 < 10$ selection. The $m_{t\bar{t}}$ distributions for data, Standard Model $t\bar{t}$ production, W + jets and multijets[2], and resonance signal for $M_X = 600$ GeV/c^2 are shown in Figure 6.1. The plots for the $m_{t\bar{t}}$ distributions for the remaining nine resonance masses are shown in Figure 6.2. The bin size shown in Figure 6.2 is different for different M_X, and also non-uniform in $m_{t\bar{t}}$. This represents the bins used for different M_X while comparing the observed $m_{t\bar{t}}$ spectrum to those expected from the different sources, as will be discussed in the next chapter.

[2]We combine the backgrounds due to W+jets and multijets in the ratio 0.78:0.22, based on a measurement of their relative proportions in the standard top mass analysis at DØ [33].

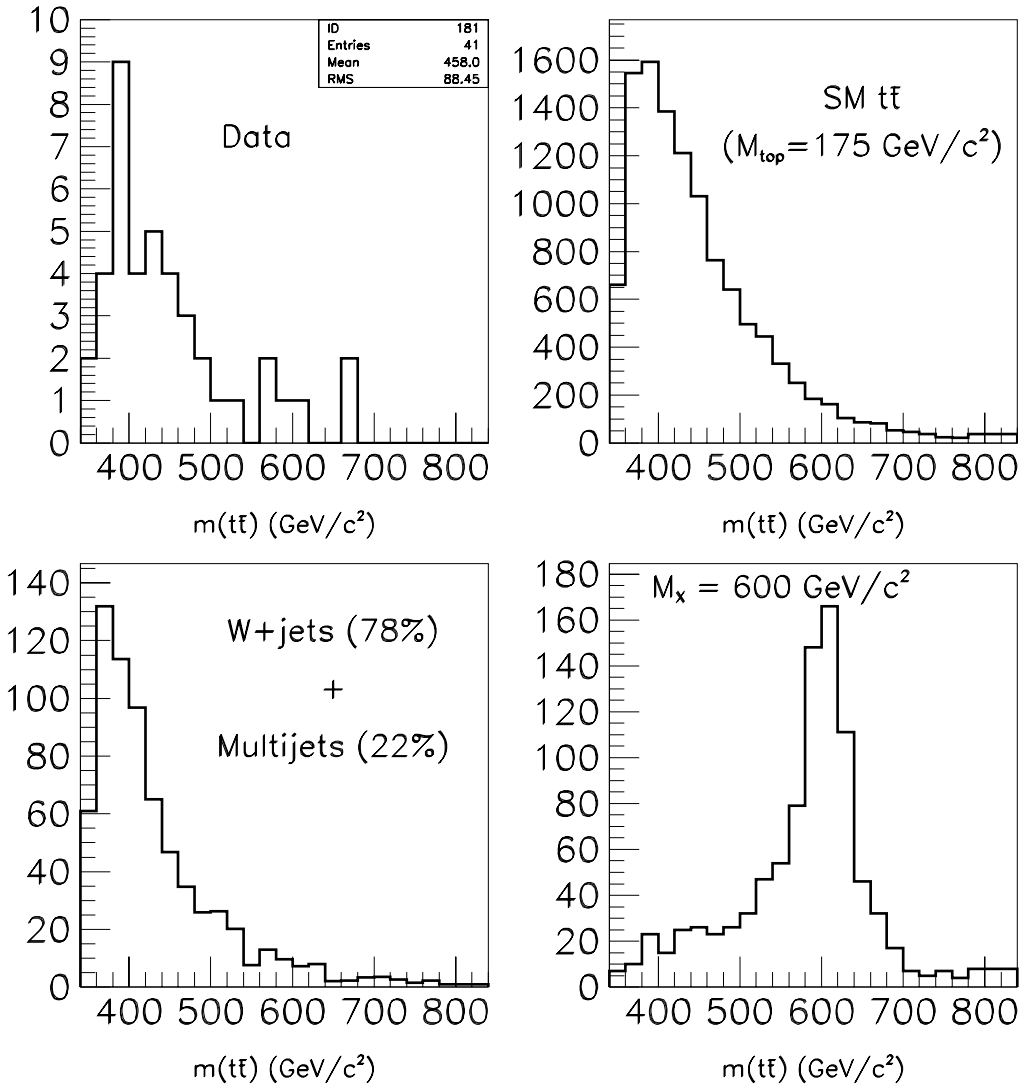

Figure 6.1: Distributions of $m_{t\bar{t}}$ for DØ Run I lepton plus jets data, Standard Model $t\bar{t}$ production, W + jets and multijets combined in the ratio 0.78:0.22, and signal ($X \to t\bar{t}$) for $M_X = 600$ GeV/c^2. The histograms are not normalized.

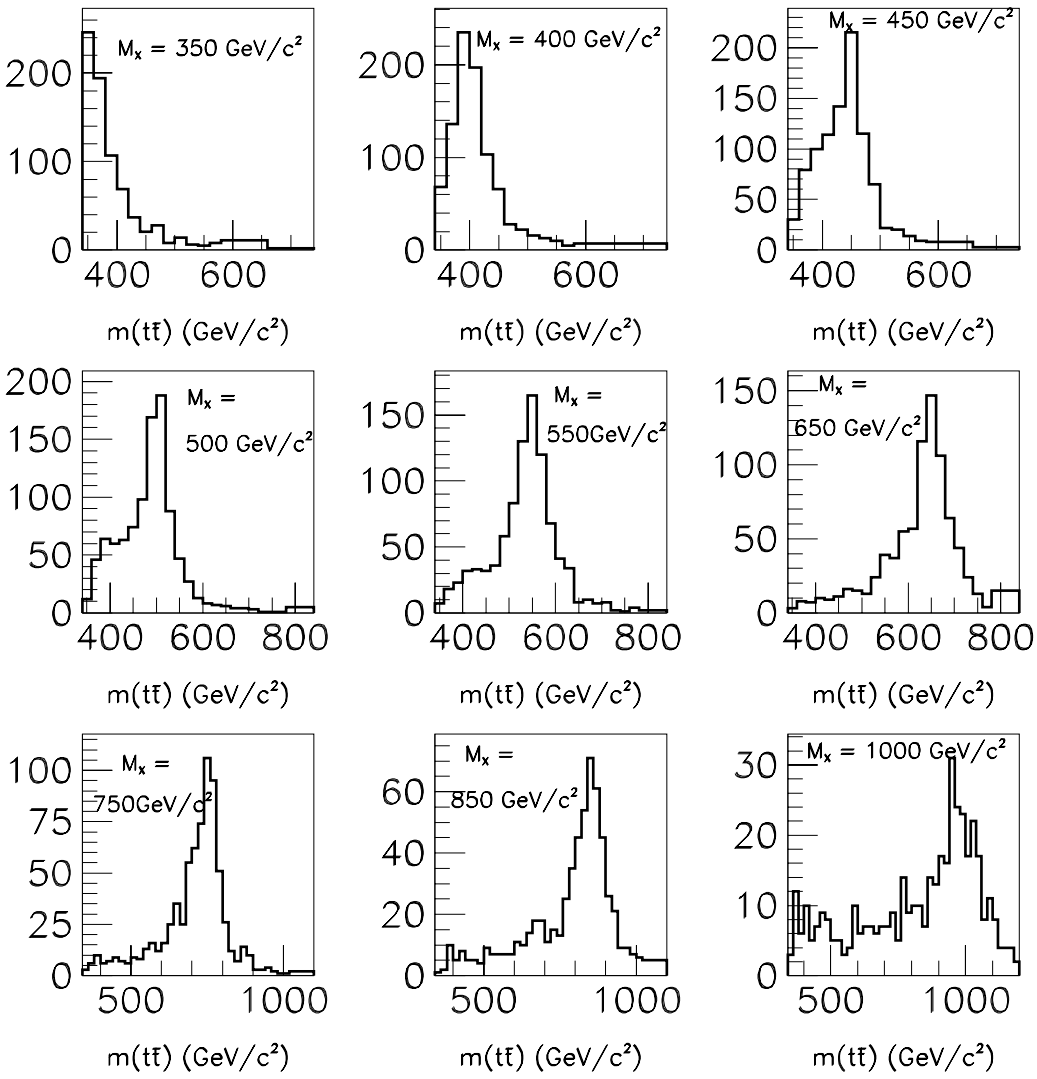

Figure 6.2: Distributions of $m_{t\bar{t}}$ for signal ($X \to t\bar{t}$) for M_X = 350-1000 GeV/c^2. The histograms are not normalized. The bin size is different for different M_X, and also non-uniform in $m_{t\bar{t}}$.

Chapter 7

Data Analysis

Once we reconstruct the top-antitop invariant mass in data, and simulate events due to the resonance signal ($X \rightarrow t\bar{t}$), at a resonance mass, M_X, and the expected sources of background (within Standard Model) contributing to the $t\bar{t} \rightarrow l$ + jets decay, we would like to make an estimate of the relative proportions of the different sources that would best describe the observed $m_{t\bar{t}}$ distribution. To do this, we use Bayesian statistics [44].

7.1 Bayesian fit of data to a three-source model

We fit the observed $m_{t\bar{t}}$ distribution to a three-source model comprising signal ($X \rightarrow t\bar{t}$) and backgrounds due to Standard Model $t\bar{t}$ production, as well as W+jets and multijets. The method is briefly discussed below.

- Consider the observed $m_{t\bar{t}}$ distribution. Suppose D_i is the observed number of events in bin i (i = 1 to M) such that the total number of

observed events is:

$$D = \sum_{i=1}^{M} D_i. \tag{7.1}$$

- Define the expected number of events in the given data sample from the different sources, at a resonance mass, M_X, as: n_1 due to $X \to t\bar{t}$, n_2 due to Standard Model $t\bar{t}$ production, and n_3 due to W+jets and multijets. Then the total number of expected events is:

$$n_{exp} = \sum_{j=1}^{3} n_j. \tag{7.2}$$

- Define a Poisson likelihood for data D, with the expected number of events, n_{exp}, at resonance mass, M_X, as:

$$L(D|n_{exp}, M_X) = \prod_{i=1}^{M} e^{(-n^i_{exp})} \ (n^i_{exp})^{D_i} \ / \ D_i!. \tag{7.3}$$

- Use Bayes' theorem to invert the likelihood function and define the 'posterior' probability of the expected number of events at M_X, given the observed data D:

$$P(n_{exp}|D, M_X) = \frac{L(D|n_{exp}, M_X)P(n_{exp}, M_X)}{\mathcal{N}}. \tag{7.4}$$

  In the above expression, $P(n_{exp}, M_X)$ represents a 'prior' probability of the expected number of events at a given value of M_X. $\mathcal{N}$ is a normalization constant obtained using the condition $\int P(n_{exp}|D, M_X)\, dn_{exp} = 1$.

- Consider the 'prior' probability, $P(n_{exp}, M_X)$. The prior probability represents any *a priori* information that one has regarding the expected

source counts n_j ($j = 1, 2, 3$). As a first guess, one can consider the expected number of events from source j as a fraction (f) of the simulated events for that source; that is, for bin i

$$n_j^i \sim f_j A_{ji}, \tag{7.5}$$

where A_{ji} is the number of simulated events for source j in bin i after all selections. Therefore one can consider

$$n_{exp}^i \sim \sum_{j=1}^{3} f_j A_{ji} \tag{7.6}$$

for each bin i. The fraction f_j represents the 'strength', or, the relative proportion of the j^{th} source in the observed data. If it were possible to repeat the process of event simulation a number of times, one could, in principle, get a 'mean' number (say, a_{ji}) of simulated events for source j in bin i. It would be more appropriate, then, to write n_{exp}^i in terms of the mean source counts (a_{ji}) as

$$n_{exp}^i = \sum_{j=1}^{3} f_j a_{ji}. \tag{7.7}$$

Since the fractions f_j are uncorrelated with the mean simulated source counts a_{ji}, the prior probability, $P(n_{exp}, M_X)$, can be written as a product of two independent prior probabilities as

$$P(n_{exp}, M_X) = P(f_1, f_2, f_3, M_X) P(a_1, a_2, a_3, M_X). \tag{7.8}$$

Since the three sources are also independent of each other, we can further write

$$\begin{aligned} P(n_{exp}, M_X) &= P(f_1, M_X) P(f_2, M_X) P(f_3, M_X) \\ &\quad \times P(a_1, M_X) P(a_2, M_X) P(a_3, M_X). \end{aligned} \tag{7.9}$$

$P(f_j, M_X)$ represents the prior probability of the 'strength' of source j. Since *a priori* we do not know which source is more favored than the other, we may assume that each source is equally likely. We can therefore consider a 'flat' prior for each source, or

$$P(f_j, M_X) = \text{constant}, j = 1, 2, 3. \tag{7.10}$$

$P(a_j, M_X)$ represents the prior probability for the mean number of simulated events for source j. We assume it to be a Poisson distribution, given the number of simulated events A_{ji} that we actually have by performing the simulation once:

$$P(a_j, M_X) = \prod_{i=1}^{M} e^{(-a_{ji})} \ (a_{ji})^{(A_{ji})} \ / \ A_{ji}!. \tag{7.11}$$

Substituting Eq. (7.10) and Eq. (7.11) in Eq. (7.9), we get

$$P(n_{exp}, M_X) \propto \prod_{j=1}^{3} \prod_{i=1}^{M} e^{(-a_{ji})} \ (a_{ji})^{(A_{ji})} \ / \ A_{ji}!. \tag{7.12}$$

Substituting Eq. (7.12) in Eq. (7.4), we get

$$P(n_{exp}|D, M_X) \propto \prod_{i=1}^{M} \frac{e^{(-n^i_{exp})} \ (n^i_{exp})^{D_i}}{D_i!} \prod_{j=1}^{3} \prod_{i=1}^{M} \frac{e^{(-a_{ji})} \ (a_{ji})^{(A_{ji})}}{A_{ji}!}, \tag{7.13}$$

where we get the overall normalization (say, $\mathcal{N}''$) by requiring $\int P(n_{exp}|D, M_X) dn_{exp} \ = \ 1$.

- It may be noted from Eq. (7.7) that n_{exp} is a function of f_j and a_{ji}. Therefore we can integrate $P(n_{exp}|D, M_X)$ over all the a_{ji}'s to get

$$P(f_1, f_2, f_3|D, M_X) = \frac{1}{\mathcal{N}''} \int P(n_{exp}|D, M_X) da_{11} ..... da_{3M}. \tag{7.14}$$

It is possible to do the above $3M$–dimensional integral exactly, and obtain the formula

$$P(f_1, f_2, f_3|D, M_X) = \prod_{i=1}^{M} \sum_{k_1,k_2,k_3=0}^{D_i} \prod_{j=1}^{3} \binom{A_{ji} + k_j}{k_j} \frac{f_j^{k_j}}{(1+f_j)^{A_{ji}+k_j+1}}, \tag{7.15}$$

where the indices k_j satisfy the multinomial constraint $\sum_{j=1}^{3} k_j = D_i$. The calculation is outlined in appendix B. $P(f_1, f_2, f_3|D, M_X)$ represents the 'posterior' probability of different relative proportions of the three sources in the observed $m_{t\bar{t}}$ distribution.

- The probability of different proportions of any source j in the observed $m_{t\bar{t}}$ distribution can then be obtained by integrating over the other two sources, that is,

$$P(f_j|D, M_X) = \int P(f_1, f_2, f_3|D, M_X) df_{j'} df_{j''}, \tag{7.16}$$

j, j', j'' = 1, 2, 3; $j \neq j' \neq j''$.

- Using Eq. (7.5), one can change variables, and re-write Eq. (7.16) as

$$P(n_j|D, M_X) = \int P(n_1, n_2, n_3|D, M_X) dn_{j'} dn_{j''}. \tag{7.17}$$

A plot of $P(n_j|D, M_X)$ vs. n_j (j = 1, 2, 3) is shown in Figure 7.1 for M_X = 600 GeV/c^2. We consider the mean of the distribution ($< n_j > = \int n_j P(n_1, n_2, n_3|D, M_X) dn_j dn_{j'} dn_{j''}$) as an estimate of the most likely value of the counts expected from each source j in the given data sample. That is, the total number of data counts, D, is

$$D = < n_1 > + < n_2 > + < n_3 > . \tag{7.18}$$

- We repeat the above procedure for each of the ten resonance masses considered between 350-1000 GeV/c^2. The mean number of events expected from each source j for different M_X, are listed in Table 7.1.

Table 7.1: The mean number of signal counts, $< n_1 >$, from $X \to t\bar{t}$, and background counts from Standard Model $t\bar{t}$ production, $< n_2 >$, as well as from W+jets and multijets, $< n_3 >$, for different values of M_X. 41 events are observed in the $m_{t\bar{t}}$ distribution of lepton + jets data after applying all selections.

M_X (GeV/c^2)	350	400	450	500	550	600	650	750	850	1000
$< n_1 >$	4.0±3.6	9.0±7.0	8.7±6.5	4.9±4.2	4.0±3.3	4.2±3.2	3.3±2.5	1.6±1.6	$1.4^{+1.5}_{-1.4}$	$1.4^{+1.5}_{-1.4}$
$< n_2 >$	23.6±11.5	20.5±10.8	18.4±11.2	22.2±11.5	24.0±11.7	23.7±11.6	24.3±11.7	26.8±11.7	26.9±11.7	27.9±11.6
$< n_3 >$	15.4±10.8	13.9±10.2	16.3±10.4	15.3±10.5	15.1±10.6	15.4±10.6	15.4±10.7	12.6±9.9	12.5±9.8	11.6±9.4
Total background= $< n_2 >+< n_3 >$	39.0±15.8	34.4±14.9	34.7±15.3	37.5±15.6	39.1±15.7	39.0±15.7	39.7±15.8	39.4±15.3	39.4±15.3	39.5±14.9

From Table 7.1 we see that $< n_1 >$ is consistent with zero within statistical errors which implies that there is no statistically significant evidence of a resonance X decaying to $t\bar{t}$. We use the mean source counts $< n_j >$ to normalize different kinematic distributions of the simulated events for each source j. In Figs. 7.2–7.6, the normalised distributions for $m_{t\bar{t}}$ are shown for different M_X. In Figs. 7.7–7.10, the transverse momentum of the top and antitop quarks (p_T^t and $p_T^{\bar{t}}$), the difference in pseudorapidity of the two top quarks ($|\Delta\eta^{t,\bar{t}}|$), and the difference in azimuthal angle of the two top quarks ($|\Delta\phi^{t,\bar{t}}|$), are shown for M_X = 400, 500, 600 and 750 GeV/c^2. The absence of

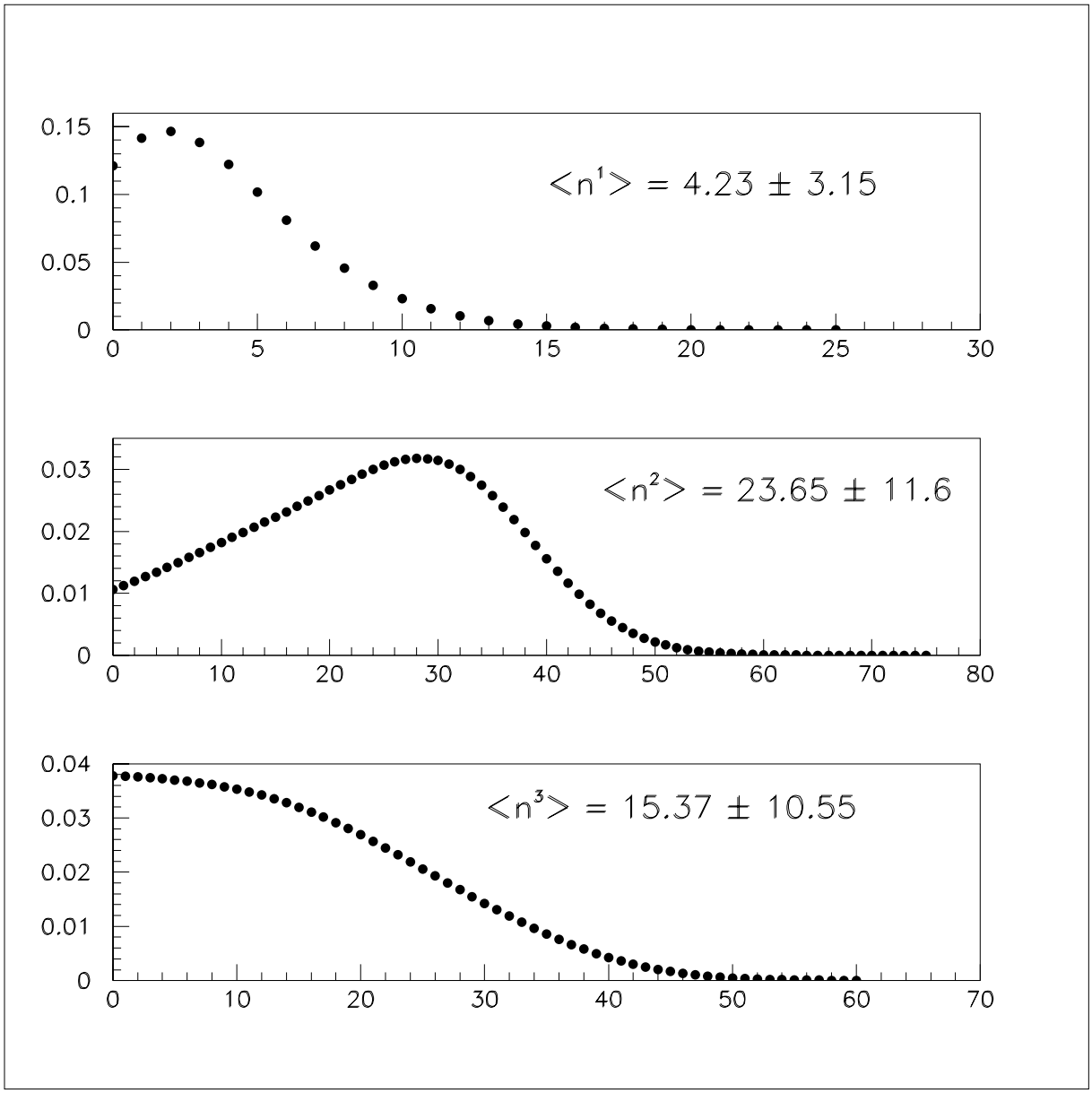

Figure 7.1: P($n_1|D,\ M_X$), P($n_2|D,\ M_X$) and P($n_3|D,\ M_X$) versus n_1, n_2 and n_3 respectively for $M_X = 600$ GeV/c^2.

any statistically significant excess from Standard Model predictions is further evident from these plots.

Therefore we proceed to set upper limits on $\sigma_X B$, the production cross section of the resonance X times its branching fraction to $t\bar{t}$.

7.2 Extraction of upper limits on $\sigma_X B$

The expected number of signal events, n_1, passing the selections discussed in chapter 4, can be expressed as

$$n_1 = \sigma_X B \ \times \ \sum_i \mathcal{A}_i \ \mathcal{L}_i, \tag{7.19}$$

where $\mathcal{A}$ is the acceptance for $X \to t\bar{t}$ events and $\mathcal{L}$ is the integrated luminosity for data, and the sum is over all channels (e+jets, μ+jets, e+jets/μ, and μ+jets/μ). We can, therefore, re-write Eq. (7.17) with $j = 1$, in terms of $\sigma_X B$, as

$$P(\sigma_X B|D, M_X) = \frac{1}{\mathcal{N}'''} \int P(n_1, n_2, n_3|D, M_X) dn_2 dn_3, \tag{7.20}$$

where $\mathcal{N}'''$ is such that $\int P(\sigma_X B|D, M_X) d(\sigma_X B) \ = \ 1$. We then define the upper limits, $(\sigma_X B)_{95}$, on the production cross section of X times its branching fraction to $t\bar{t}$, at 95% confidence, as

$$\int_0^{(\sigma_X B)_{95}} P(\sigma_X B|D, M_X) d(\sigma_X B) = 0.95 \tag{7.21}$$

for every M_X.

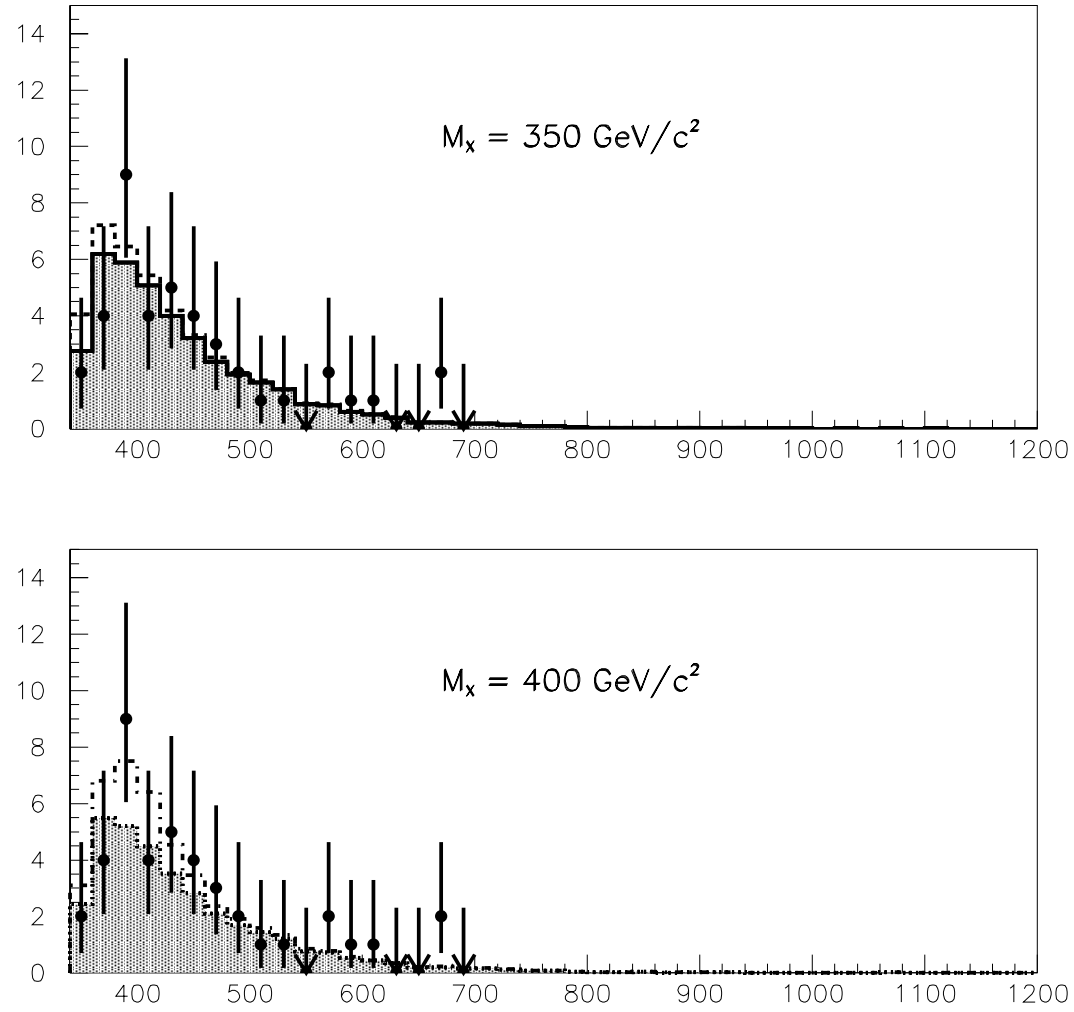

Figure 7.2: Normalized distributions of $m_{t\bar{t}}$ for sum of all Standard Model (SM) backgrounds (shaded histogram) and sum of signal ($X \to t\bar{t}$) and SM backgrounds (unshaded histogram) for $M_X = 350$ and 400 GeV/c^2. The data $m_{t\bar{t}}$ distribution is shown by dots along with the statistical errors.

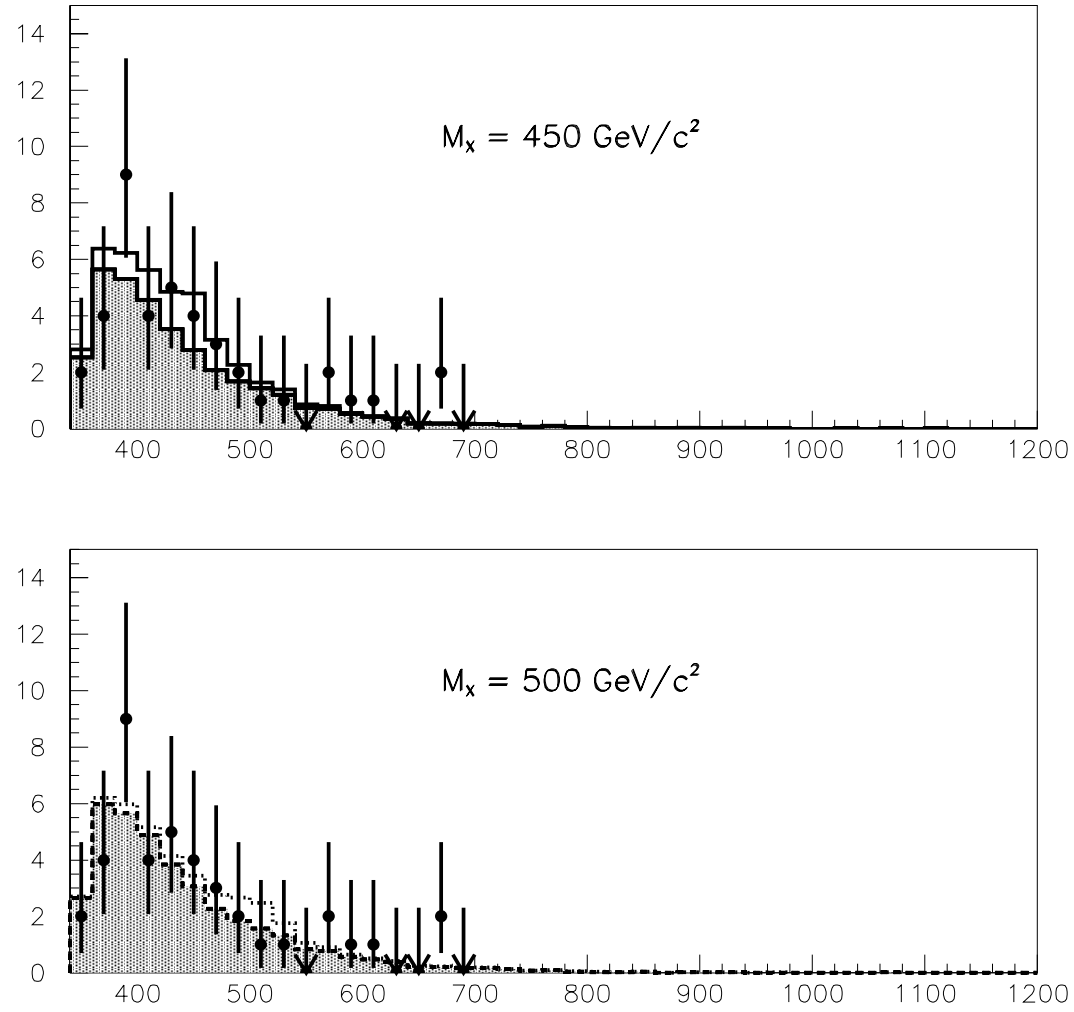

Figure 7.3: Normalized distributions of $m_{t\bar{t}}$ for sum of all SM backgrounds (shaded histogram) and sum of signal ($X \to t\bar{t}$) and SM backgrounds (unshaded histogram) for M_X = 450 GeV/c^2 and 500 GeV/c^2. The data $m_{t\bar{t}}$ distribution is shown by dots.

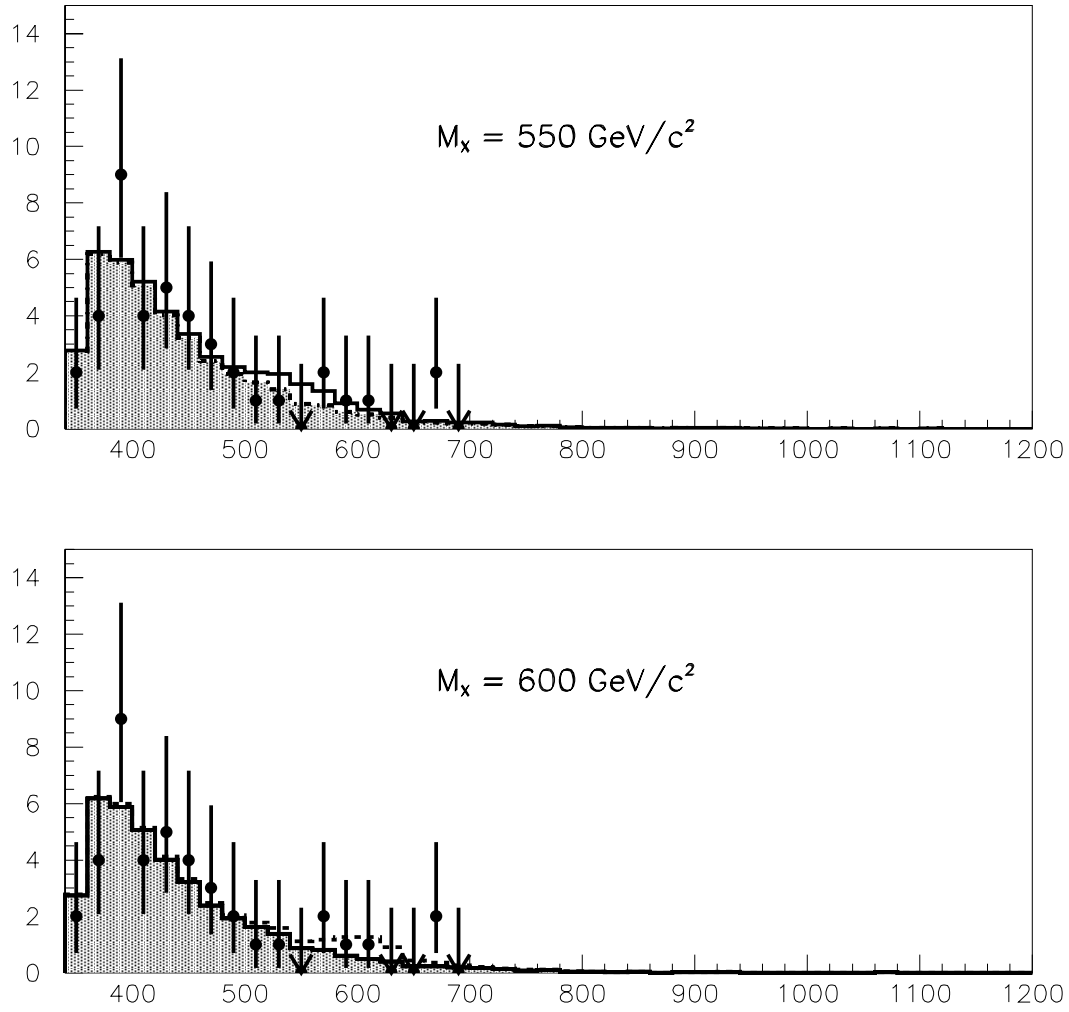

Figure 7.4: Normalized distributions of $m_{t\bar{t}}$ for sum of all SM backgrounds (shaded histogram) and sum of signal ($X \to t\bar{t}$) and SM backgrounds (unshaded histogram) for $M_X = 550$ and 600 GeV/c^2. The data $m_{t\bar{t}}$ distribution is shown by dots.

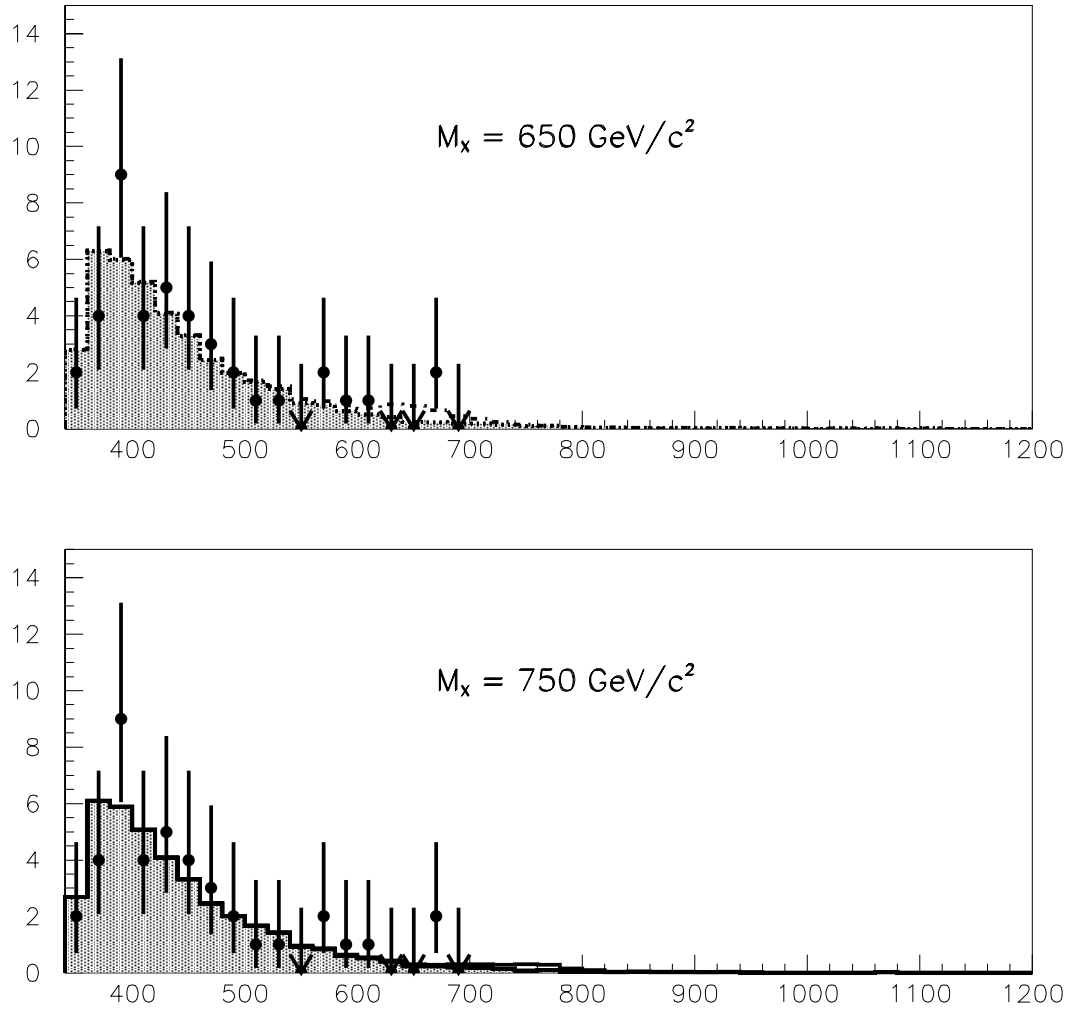

Figure 7.5: Normalized distributions of $m_{t\bar{t}}$ for sum of all SM backgrounds (shaded histogram) and sum of signal ($X \to t\bar{t}$) and SM backgrounds (unshaded histogram) for $M_X = 650$ and 750 GeV/c^2. The data $m_{t\bar{t}}$ distribution is shown by dots.

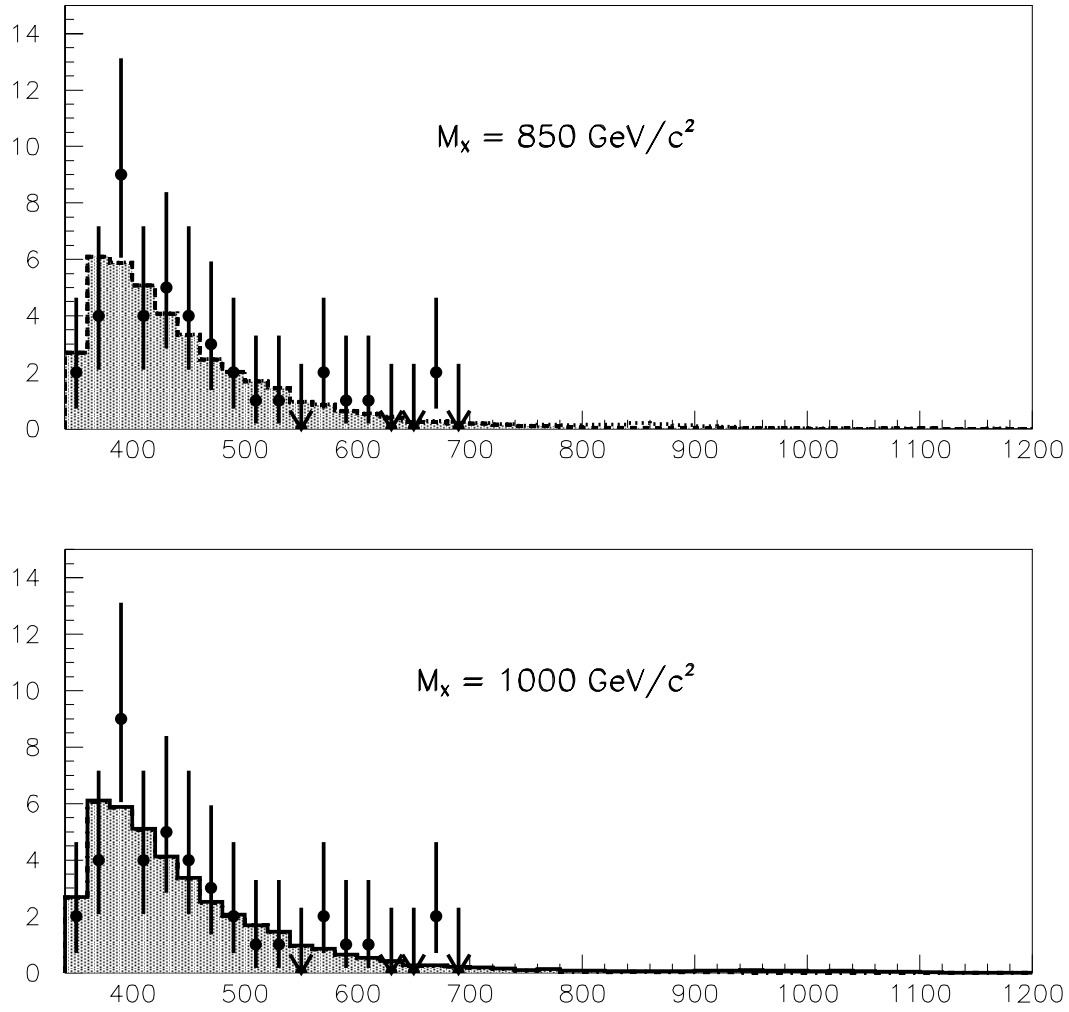

Figure 7.6: Normalized distributions of $m_{t\bar{t}}$ for sum of all SM backgrounds (shaded histogram) and sum of signal ($X \to t\bar{t}$) and SM backgrounds (unshaded histogram) for $M_X = 850$ and 1000 GeV/c^2. The data $m_{t\bar{t}}$ distribution is shown by dots.

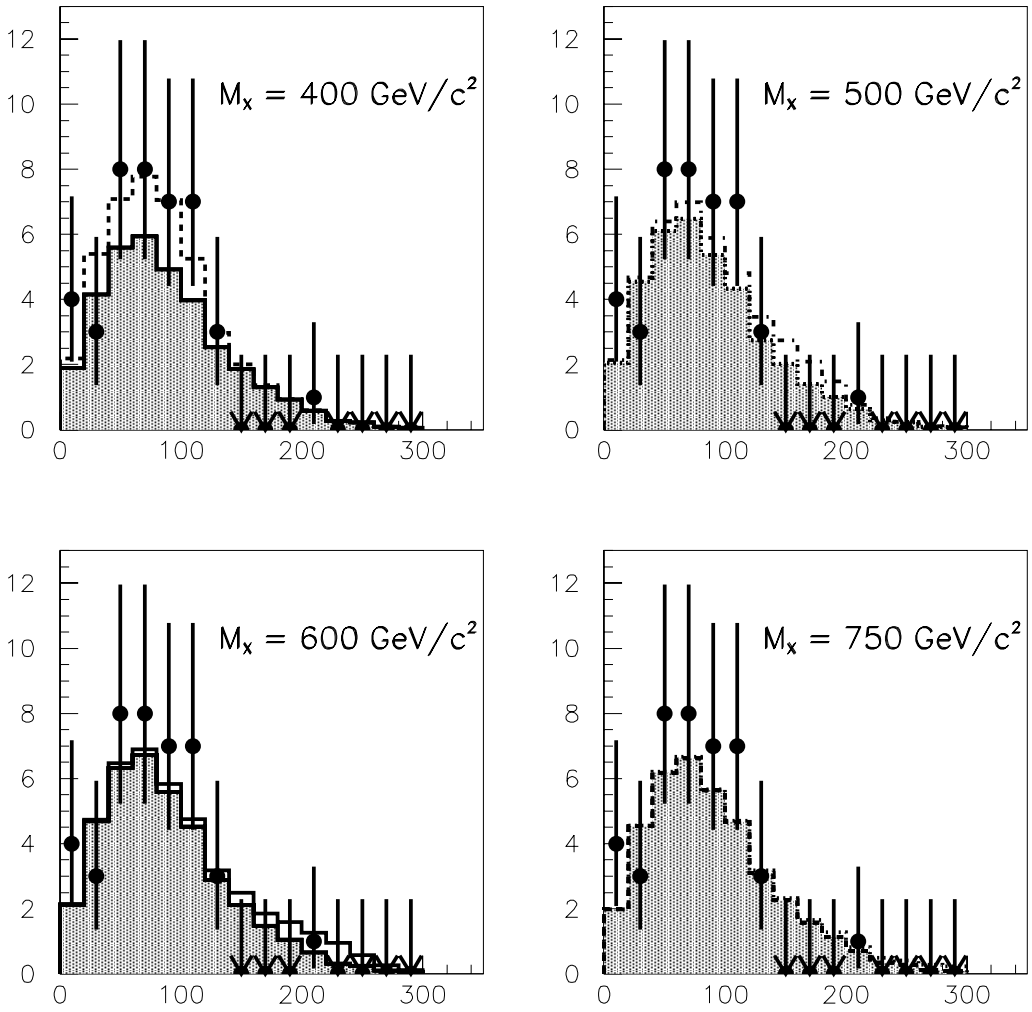

Figure 7.7: Normalized distributions of the transverse momentum of top quark (p_T^t) for sum of all SM backgrounds (shaded histogram) and sum of signal ($X \to t\bar{t}$) and SM backgrounds (unshaded histogram) for $M_X = 400$, 500, 600 and 750 GeV/c^2. The data p_T^t distribution is shown by dots.

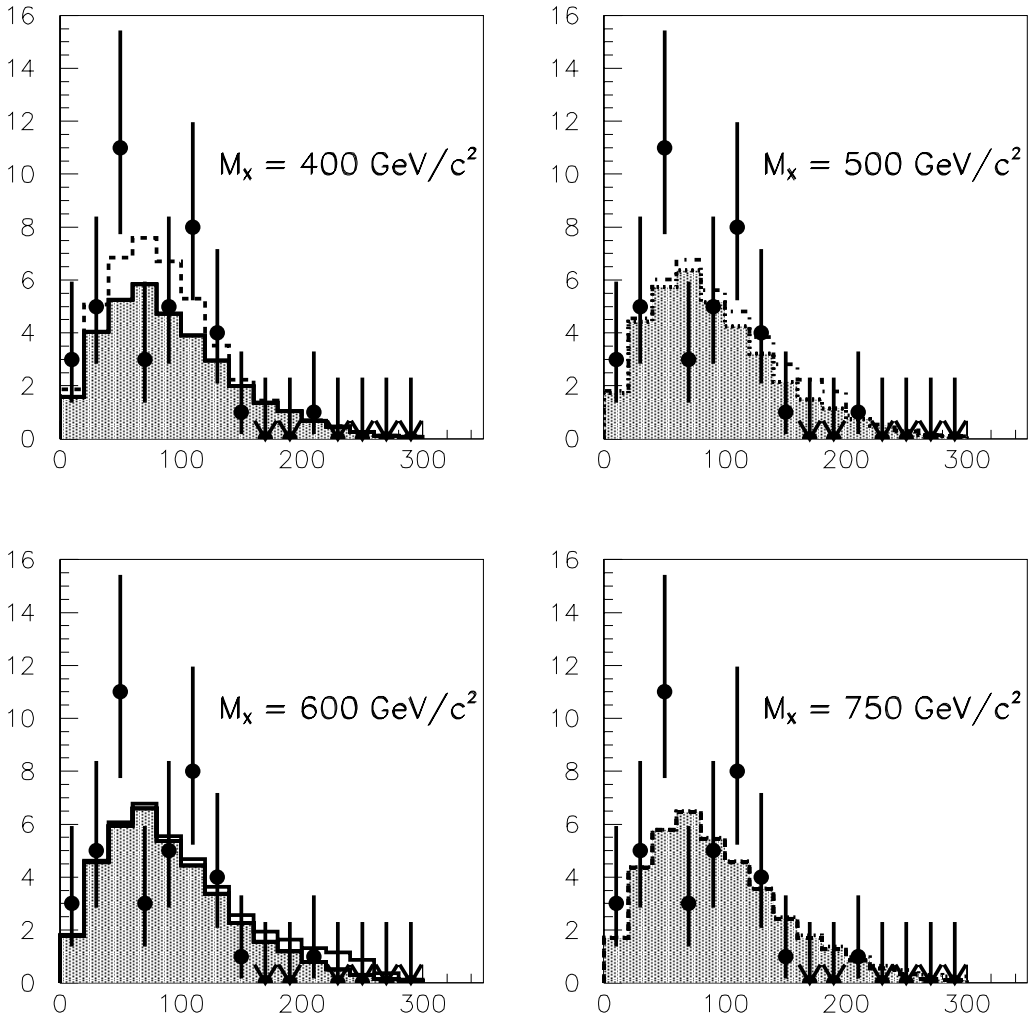

Figure 7.8: Normalized distributions of the transverse momentum of anti-top quark ($p_T^{\bar{t}}$) for sum of all SM backgrounds (shaded histogram) and sum of signal ($X \to t\bar{t}$) and SM backgrounds (unshaded histogram) for M_X = 400, 500, 600 and 750 GeV/c^2. The data $p_T^{\bar{t}}$ distribution is shown by dots.

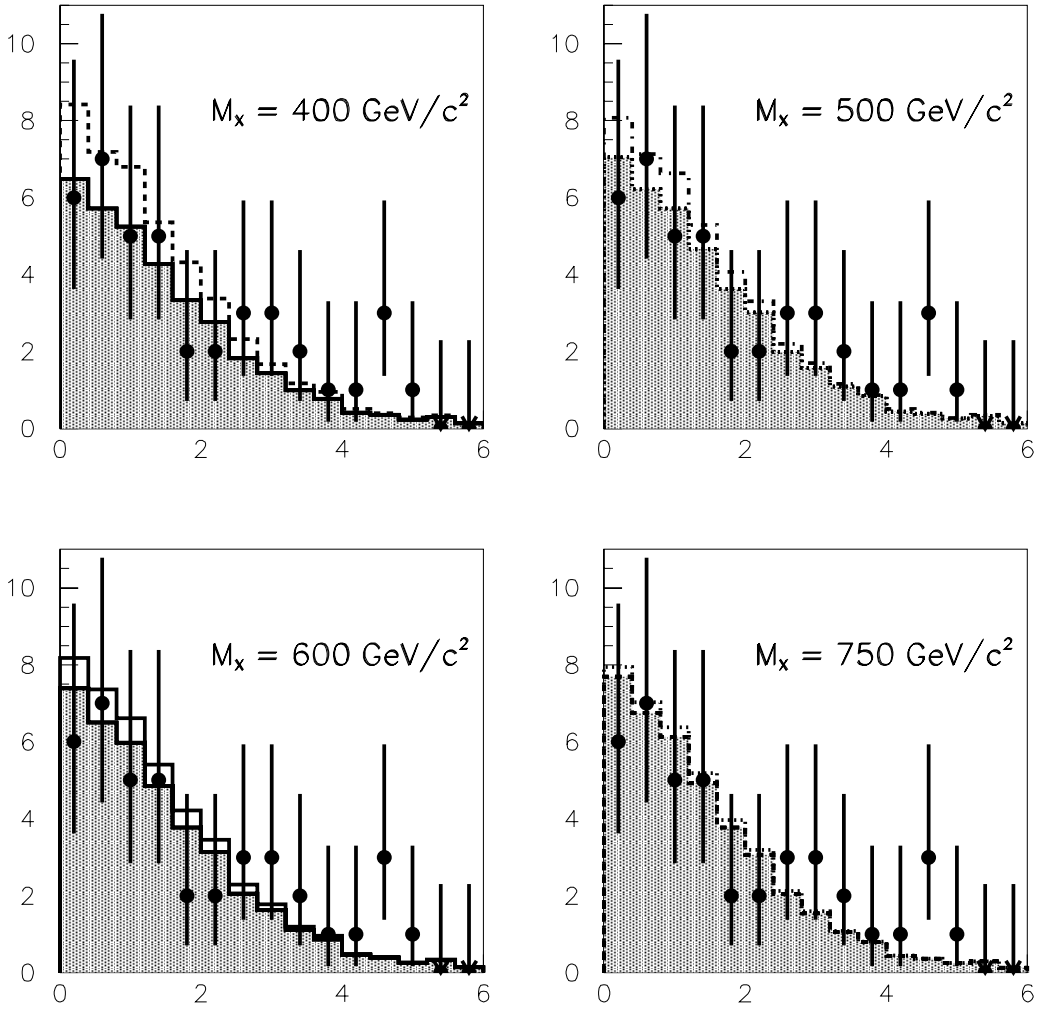

Figure 7.9: Normalized distributions of the difference in pseudorapidity η between the two top quarks ($|\Delta\eta^{t,\bar{t}}|$). The shaded histogram is the sum of all SM backgrounds, and the unshaded histogram is the sum of signal ($X \to t\bar{t}$) and SM backgrounds for M_X = 400, 500, 600 and 750 GeV/c^2. The data $|\Delta\eta^{t,\bar{t}}|$ distribution is shown by dots.

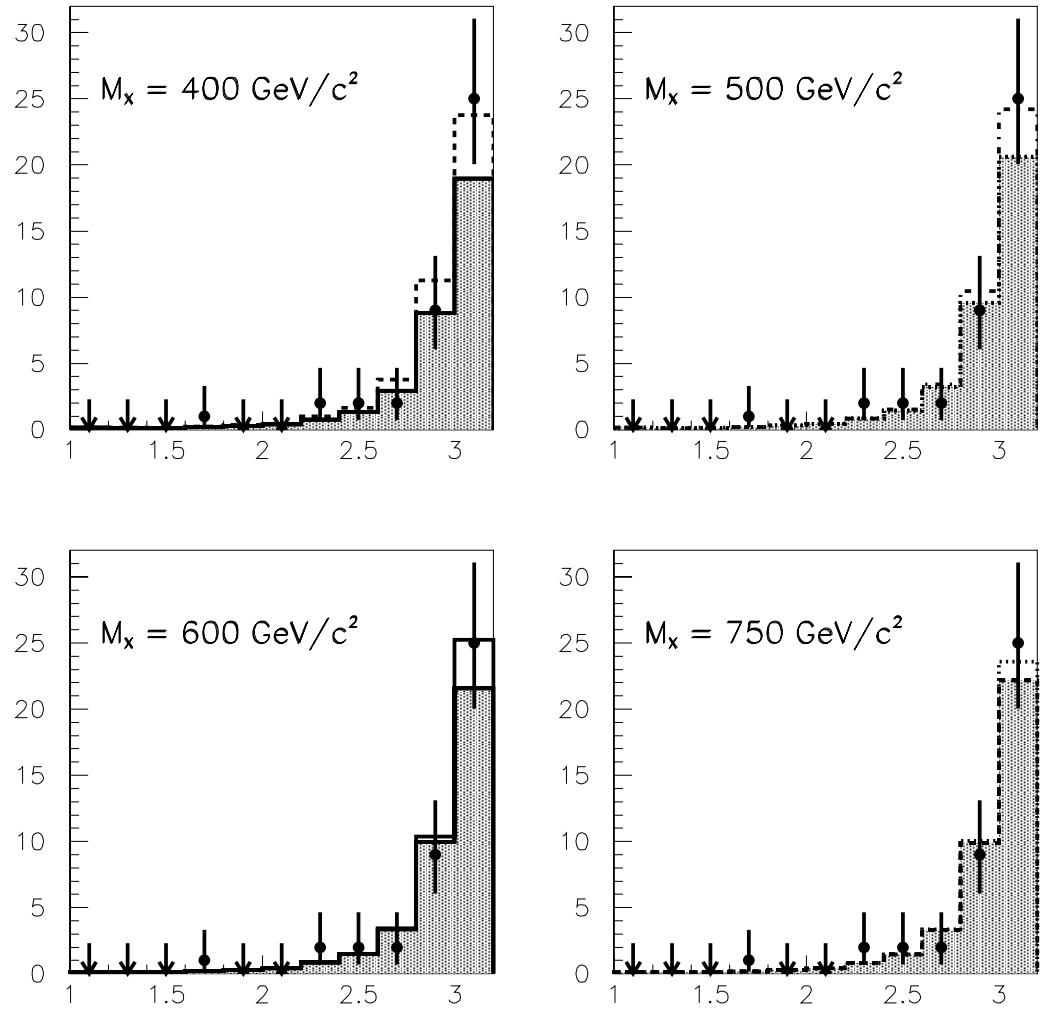

Figure 7.10: Normalized distributions of the difference in azimuthal angle ϕ between the two top quarks ($|\Delta\phi^{t,\bar{t}}|$). The shaded histogram is the sum of all SM backgrounds, and the unshaded histogram is the sum of signal ($X \to t\bar{t}$) and SM backgrounds for M_X = 400, 500, 600 and 750 GeV/c^2. The data $|\Delta\phi^{t,\bar{t}}|$ distribution is shown by dots.

7.2.1 Calculation of acceptance ($\mathcal{A}$)

The acceptance $\mathcal{A}_i$ for any channel i, is defined as:

$$\mathcal{A}_i = \epsilon_i^{trig} \times \epsilon^{pid} \times \epsilon_i^{sel} \times \mathcal{B}, \tag{7.22}$$

where ϵ_i^{trig} is the trigger efficiency for the i^{th} channel, ϵ^{pid} is the identification (ID) efficiency of isolated electrons or muons and any μ-tags, ϵ_i^{sel} is the efficiency of the selection criteria for the i^{th} channel, and $\mathcal{B}$ is the branching fraction of the Monte Carlo signal sample, which takes account of the forced decay of one of the W bosons in the Pythia event generator. Each of these is discussed below in more detail.

Trigger efficiency

Trigger efficiencies are obtained from data or Monte Carlo depending on the channel [23]. For the e+jets channel, it is obtained from W+jets data and determined to be $98.2^{+1.8}_{-4.4}$%. For the μ+jets channel, the trigger efficiency is computed using data-derived trigger turn-on curves applied to $t\bar{t}$ Monte Carlo and is determined to be 89 ± 5%. The trigger efficiencies for the tagged channels is determined in a similar way. For the e+jets/μ channel, it is determined to be 99^{+1}_{-5}% and for the μ+jets/μ channel, it is determined to be 96^{+4}_{-5}%. These values are listed in Table 7.2.

Table 7.2: Trigger efficiencies (in %) for the four lepton+jets channels

ϵ_{ej}^{trig}	$\epsilon_{ej/\mu}^{trig}$	$\epsilon_{\mu j}^{trig}$	$\epsilon_{\mu j/\mu}^{trig}$
$98.2^{+1.8}_{-4.4}$	99^{+1}_{-5}	89^{+5}_{-5}	96^{+4}_{-5}

Particle identification efficiency

The identification efficiency of electrons and muons in data events is discussed in Sections 3.3 and 3.4. In case of signal ($X \rightarrow t\bar{t}$) events which are generated using Monte Carlo, and processed through a detailed detector simulation, the identification criteria for electrons and muons discussed in chapter 3 are applied by the DØ reconstruction program. But these identification criteria are somewhat over-estimated for the Monte Carlo sample. We therefore need to correct for the relative data to Monte Carlo identification efficiencies for both electrons and muons. These corrections are described below.

Electron identification

In case of data events as mentioned in chapter 3, tight identification criteria are used for electrons, whereas, for the Monte Carlo signal sample, loose identification criteria are used for electrons. Therefore, we determine the overall Monte Carlo electron-identification efficiency (including the efficiency for tracking done during the reconstruction of objects) by taking the ratio of the

number of reconstructed electrons to the number of electrons at generator–level. The method is described in detail in appendix C. Here we list the overall correction factors that need to be applied for electron identification in the Monte Carlo signal sample, in different regions of the detector. These are:

$$f_{CC}^{e-ID} = \frac{\epsilon_{CC}^{e-id}(data)}{\epsilon_{CC}^{e-id}(MC)} = \frac{0.588 \pm 0.011}{0.630 \pm 0.018} \quad (7.23)$$

$$= 0.933 \pm 0.032, \quad \text{in the CC, } (|\eta_{det}| < 1.0) \quad (7.24)$$

$$f_{EC}^{e-ID} = \frac{\epsilon_{EC}^{e-id}(data)}{\epsilon_{EC}^{e-id}(MC)} = \frac{0.347 \pm 0.014}{0.468 \pm 0.027} \quad (7.25)$$

$$= 0.741 \pm 0.052, \quad \text{in the EC, } (1.0 \leq |\eta_{det}| < 2.0) \quad (7.26)$$

Muon identification

The identification criteria discussed in Section 3.4 for the muons are also applied to the signal Monte Carlo events during event reconstruction. But the identification efficiency is somewhat over–estimated in the Monte Carlo sample compared to the data muon identification efficiency. We therefore need to apply a multiplicative correction factor to correct for the differences between the data and Monte Carlo efficiencies. We consider the following terms for calculating the overall multiplicative data to Monte Carlo correction factor for muon identification:

- Eye Scan: For a given muon track the DØ reconstruction program will reconstruct a muon a certain fraction of the time. The corresponding "reconstruction efficiency" is close to 100% for Monte Carlo muons, whereas it is typically between 90-95% in case of real data. Thus a correction is needed for the output from the full detector simulator, DØGEANT. This is determined from scanned samples of muon tracks, which are free from reconstruction biases [45, 46], and is called the "eye-scan" correction term. This correction applicable for all run periods is 94.1 ± 1.5 % in the central muon region (CF), and 91.1 ± 2.2 % in the forward muon region (EF). The CF is defined by $|\eta_{det}| < 1.0$, and the EF is defined by $|\eta_{det}| \geq 1.0$. For this correction, we require only the basic quality cuts of IFW4 ≤ 1 in the CF and IFW4 $= 0$ in the EF. Hence the results are the same for both isolated and tag muons.

- Mu-Smear: The decay products from the $t\bar{t}$ pair are emitted at central rapidities and the muon identification is therefore restricted to the central (WAMUS) portion of the DØ muon system, $|\eta_{det}| < 1.7$. Due to inefficiencies caused by radiation damage, the forward muon region (EF) was not used in this analysis for Run Ia ($\approx 10\ pb^{-1}$) or the early part of Run Ib ($\approx 49\ pb^{-1}$). The chambers were subsequently cleaned and returned to full efficiency for the remainder of Run Ib and Run Ic. The pre–cleaning period of Run Ib is denoted as "prezap" and the post–cleaning period as "postzap". The corrections to these time dependent detector inefficiencies are applied using a software "mu-smear".

These corrections are a function of the track identification requirements (the identification requirements for muons listed in Table 3.2 except the kinematic (p_T) and ΔR requirements) and are different for different run periods. Cleaning the chambers increased the efficiency in the EF region appreciably but had no significant effect on the efficiencies in the CF region [42]. The corrections for the effect of chamber cleaning, applied to the Monte Carlo signal sample, are somewhat over–estimated compared to the corresponding corrections in data. We therefore consider the relative data to Monte Carlo correction factors for this effect, for all run periods, as applied to a Monte Carlo sample to which the Run Ib postzap mu-smear corrections have been applied [47].

- ϕ-hole : This is an additional localized inefficiency. For data taken prior to chamber cleaning (prezap) there was a well-defined inefficient region in the vicinity of the main ring pipe. This covered the azimuthal (ϕ) region of $80 < \phi < 120$. Because of the poor efficiency of the EF regions before cleaning, this region is normally excluded, so that this only affects the analysis of the Run Ia and Run Ib prezap CF data. This effect is usually referred to as the ϕ-hole. The inefficiency is believed to be the result of deposition on the proportional drift tube signal wires closest to the main ring. The inefficiency due to this effect in the data from Run Ia is less than that from Run Ib (prezap) because the effects of wire deposition on signal response are cumulative. After the chambers were cleaned the effect went away and was not visible in Run Ib (postzap)

data. The ϕ-hole inefficiency is not seen in case of tag muons since the low p_T muons require lesser number of hits compared to the high p_T isolated muons.

The multiplicative correction factors for the above terms are given below in Table 7.3 for isolated muons and in Table 7.4 for tag muons. The errors shown include both the statistical and systematic components.

Table 7.3: The multiplicative correction factors for the isolated muon to account for differences between data and Monte Carlo muon identification efficiencies. The Monte Carlo is assumed to be processed through Run Ib post-zap mu-smear package.

	mu-smear CF	ϕ holes CF	EyeScan CF	mu-smear EF	ϕ holes EF	EyeScan EF
RunIa	1.063	0.95±0.050	0.941±0.015	0	0	0.911±0.022
RunIb ("prezap")	1.04	0.90±0.050	0.941±0.015	0	0	0.911±0.022
RunIb ("postzap")	1.0	*	0.941±0.015	1.0	*	0.911±0.022

"*" corresponds to a value of one in the above entries.

The overall correction factors for the identification of isolated muons and tag muons in the CF and EF for the different run periods are given in Table 7.5.

We finally use a luminosity-weighted correction to make the acceptance of the Monte Carlo signal events represent that of the full Run I data. The break-up for the luminosity fractions for different run periods is given in Table 7.6 [47]. In the beginning of run I most triggers were disabled when a Main Ring beam was present in the detector as discussed in Section 2.8.5.

Table 7.4: The multiplicative correction factors for the tag muon to account for differences between data and Monte Carlo muon identification efficiencies. The Monte Carlo is assumed to be processed through Run Ib post-zap mu-smear package.

	mu-smear CF	ϕ holes CF	EyeScan CF	mu-smear EF	ϕ holes EF	EyeScan EF
RunIa	0.998	*	0.941±0.015	0.0	0	0.911±0.022
RunIb ("prezap")	0.994	*	0.941±0.015	0.0	0	0.911±0.022
RunIb ("postzap")	1.0	*	0.941±0.015	1.0	*	0.911±0.022

Table 7.5: The overall multiplicative correction factors for the identification of isolated muons and the tag muons for the different run periods.

	Isol. muon, CF	Isol. muon, EF	Tag muon, CF	Tag muon, EF
RunIa	0.95 ± 0.053	0.0	0.939 ± 0.015	0.0
RunIb ("prezap")	0.881 ± 0.051	0.0	0.935 ± 0.015	0.0
RunIb ("postzap")	0.941 ± 0.015	0.911 ± 0.022	0.941 ± 0.015	0.911 ± 0.022

The official luminosity assumed no data was taken during this time and only the so-called GOODBEAM luminosity was reported. However as the run progressed, data was taken during the Main Ring cycles also and a procedure was developed to correct the data for this. This data was called the MRBS_LOSS data. The total luminosity for the μ+jets channels is the sum of the GOODBEAM luminosity and the recovered MRBS_LOSS luminosity. If the recovered data is also used then the GOODBEAM fractions must be corrected by the active recovery multiplication factors as indicated in Table 7.6.

Table 7.6: The break-up for the luminosity fractions for different run periods.

Period i	Goodbeam (a_i)	Active Recovery factor (f_i)	$a_i f_i$	Overall fraction ($a_i f_i$ / $\sum_i a_i f_i$)
RunIa	0.111	1.000	0.111	0.101
RunIb ("prezap"): (μ-jet triggers)	0.207	1.063	0.220	0.201
RunIb ("prezap"): (μ-jet + $\not\!\!E_T$ triggers)	0.326	1.137	0.371	0.338
RunIb ("postzap")	0.356	1.110	0.395	0.360

The overall luminosity weighted relative data to Monte Carlo correction factors for the identification of muons are listed in Table 7.7[1].

Table 7.7: The overall luminosity weighted relative data to Monte Carlo correction factors for the identification of isolated muons and tag muons.

Isol. muon, CF ($f_{CF}^{isol.\mu-ID}$)	Isol. muon, EF ($f_{EF}^{isol.\mu-ID}$)	Tag muon, CF ($f_{CF}^{tag\mu-ID}$)	Tag muon, EF ($f_{EF}^{tag\mu-ID}$)
0.91 $\pm$ 0.075	0.33 $\pm$ 0.022	0.94 $\pm$ 0.026	0.33 $\pm$ 0.022

Selection efficiency

The selection efficiency (ϵ^{sel}) is a function of M_X, and is defined as the fraction of events that pass the selections listed in Table 4.4. The number of events that pass these criteria in different fiducial regions of the detector, for

[1]For this table, we have combined the luminosity fractions for the two sub-periods of runIb (prezap) corresponding to the two different triggers used.

the 10 chosen values of M_X, and for the four channels, are listed in Table 7.8.

Table 7.8: Total number of generated events (N_{gen}), and the number remaining (N_{sel}) in the four lepton+jets channels in different η regions for different M_X, after applying all selection criteria.

M_X (GeV/c^2)		350	400	450	500	550	600	650	750	850	1000
N_{gen}		10k	10k	9994	10k	10k	9996	9996	10k	10k	9998
N_{sel}											
ej	isol. e (CC)	308	395	392	415	395	360	342	255	208	175
	isol. e (EC)	62	73	82	91	87	74	54	81	65	46
μj	isol. μ (CF)	212	246	264	237	232	250	203	209	152	95
	isol. μ (EF)	48	57	63	79	62	79	74	62	67	38
ej/μ	isol. e (CC) & tag μ (CF)	50	62	63	68	64	71	68	65	53	33
	isol. e (CC) & tag μ (EF)	11	13	14	15	16	14	14	10	14	11
	isol. e (EC) & tag μ (CF)	11	16	14	21	14	11	12	16	11	6
	isol. e (EC) & tag μ (EF)	2	2	2	2	6	3	3	3	4	4
μj/μ	isol. μ (CF) & tag μ (CF)	35	32	31	43	33	38	47	27	24	11
	isol. μ (CF) & tag μ (EF)	10	7	7	9	7	7	12	8	2	5
	isol. μ (EF) & tag μ (CF)	6	9	9	8	8	11	6	6	11	6
	isol. μ (EF) & tag μ (EF)	1	2	0	2	1	5	7	1	1	3

The overall $\epsilon^{pid} \times \epsilon^{sel}$ values for the four lepton+jets channels are then determined as follows:

- Topological channels

  For e+jets:

$$\epsilon^{pid} \times \epsilon^{sel} = f_{CC}^{e-ID} \times \epsilon_{CC}^{sel} + f_{EC}^{e-ID} \times \epsilon_{EC}^{sel} \tag{7.27}$$

where ϵ^{sel}_{CC} (ϵ^{sel}_{EC}) is the fraction of events that pass the selections in the CC (EC).

For μ+jets:

$$\epsilon^{pid} \times \epsilon^{sel} = f^{isol.\mu-ID}_{CF} \times \epsilon^{sel}_{CF} + f^{isol.\mu-ID}_{EF} \times \epsilon^{sel}_{EF} \tag{7.28}$$

where ϵ^{sel}_{CF} (ϵ^{sel}_{EF}) is the fraction of events that pass the selections in the CF (EF).

- μ-tagging channels

  For e+jets/μ:

$$\begin{aligned} \epsilon^{pid} \times \epsilon^{sel} \;=\; & f^{e-ID}_{CC} \times f^{tag\mu-id}_{CF} \times N_1/N_{gen} \\ & + f^{e-id}_{CC} \times f^{tag\mu-ID}_{EF} \times N_2/N_{gen} \\ & + f^{e-id}_{EC} \times f^{tag\mu-ID}_{CF} \times N_3/N_{gen} \\ & + f^{e-id}_{EC} \times f^{tag\mu-ID}_{EF} \times N_4/N_{gen} \end{aligned} \tag{7.29}$$

where N_1 is the number of events selected with the electron in the CC and the tagging muon in the CF, N_2 is the number of events selected with the electron in the CC and the tagging muon in the EF, N_3 is the number of events selected with the electron in the EC and the tagging

muon in the CF, N_4 is the number of events selected with the electron in the EC and the tagging muon in the EF, and N_{gen} is the total number of events generated using Pythia.

For μ+jets/μ:

$$\begin{aligned} \epsilon^{pid} \times \epsilon^{sel} &= f_{CF}^{isol.\mu-ID} \times f_{CF}^{tag\mu-id} \times N_1'/N_{gen} \\ &+ f_{CF}^{isol.\mu-id} \times f_{EF}^{tag\mu-ID} \times N_2'/N_{gen} \\ &+ f_{EF}^{isol.\mu-id} \times f_{CF}^{tag\mu-ID} \times N_3'/N_{gen} \\ &+ f_{EF}^{isol.\mu-id} \times f_{EF}^{tag\mu-ID} \times N_4'/N_{gen} \end{aligned} \tag{7.30}$$

where N_1' is the number of events selected with the isolated muon in the CF and the tagging muon in the CF, N_2' is the number of events selected with the isolated muon in the CF and the tagging muon in the EF, N_3' is the number of events selected with the isolated muon in the EF and the tagging muon in the CF, and N_4' is the number of events selected with the isolated muon in the EF and the tagging muon in the EF.

Branching fraction $\mathcal{B}$

As indicated previously, while generating the signal events using Pythia, one of the W bosons is forced to decay leptonically in order to have at least

one lepton (e, μ or τ) in the final state. To correct for this forced decay, we use a branching fraction of 5/9, which is the probability of getting at least one lepton in $t\bar{t}$ decay. But since only one of the W bosons is always forced to decay leptonically, the ratio of dilepton events to single lepton events from Pythia in the present case is twice than what it would be in a sample of unconstrained $t\bar{t}$ decays. We can correct for this effect by randomly removing half of the dilepton Pythia events before processing them through DØGEANT. In the present analysis we have instead processed all the Monte Carlo events through DØGEANT, and, based upon Monte Carlo studies, corrected for the double-counted dilepton events by using a factor of 1.2. We therefore use an overall branching fraction of $5/9 \times 1.2$ for $\mathcal{B}$. Details of the study done to determine the correction factor of 1.2 are given in Appendix D.

Finally we use Eqs. (7.22)-(7.30) to calculate the acceptance A_i for the four lepton+jets channels. These values are listed in Table 7.9. The integrated luminosities for the individual channels are given in Table 7.10 [23]. The values of $\sum_i A_i \mathcal{L}_i$, with the statistical errors and the systematic errors from various sources, are tabulated in Table 7.11, for different M_X. The statistical errors in the different channels are added in quadrature. For the total systematic uncertainty from any source, the corresponding errors in the different channels are added in quadrature if there is no correlation between them, else they are added linearly following the procedure described in Ref. [48].

With all the information in hand, Eq. (7.19) can now be used to determine the expected number of lepton+jets events, n_1, from the decay of $X \to t\bar{t}$ for different values of $\sigma_X B$, at any resonance mass, M_X.

Table 7.9: Acceptance A_i (in %) for the four lepton+jets channels for different M_X.

M_X (GeV/c^2)	350	400	450	500	550	600	650	750	850	1000
ej	2.20	2.80	2.80	2.90	2.80	2.60	2.40	2.00	1.60	1.30
μj	1.20	1.40	1.60	1.40	1.40	1.50	1.20	1.24	0.95	0.57
ej/μ	0.37	0.46	0.45	0.53	0.50	0.50	0.50	0.50	0.40	0.26
μj/μ	0.20	0.20	0.20	0.26	0.22	0.24	0.30	0.17	0.16	0.08

7.2.2 Upper limits on $\sigma_X B$

We next use Eq. (7.20) to determine the posterior probability density, $P(\sigma_X B|D, M_X)$, for different values of $\sigma_X B$, for any mass M_X, given the observed $m_{t\bar{t}}$ distribution (D). Figs. 7.11-7.15 show plots of the posterior probability density and the cumulative probability versus $\sigma_X B$, for different values of M_X. The 95% confidence level upper limits on $\sigma_X B$ at each M_X, defined by Eq. (7.21), are tabulated in Table 7.12.

We finally use a model of topcolor-assisted technicolor [11] to set a lower limit on the mass of the $t\bar{t}$ resonance M_X. A point on the M_X axis is excluded if the expected value of $\sigma_X B$ in the topcolor-assisted technicolor model for that mass M_X is larger than the measured 95% C.L. upper limit on $\sigma_X B$. The expected values of $\sigma_X B$ using the above model, and the measured 95% C.L. upper limits on $\sigma_X B$ (with W+jets and multijets combined in the ratio

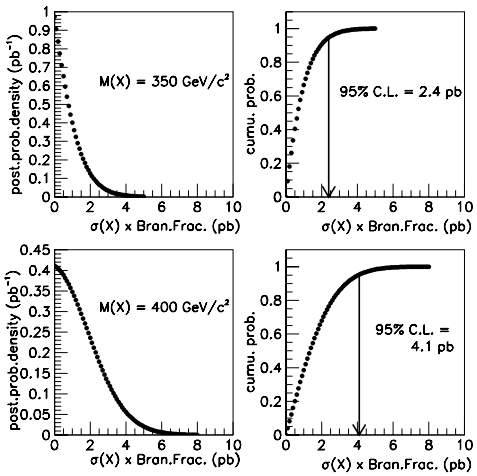

Figure 7.11: The posterior probability density and the cumulative probability vs. $\sigma_X B$ for $M_X = 350$ and 400 GeV/c^2. The arrow shows the 95% confidence level upper limit on $\sigma_X B$.

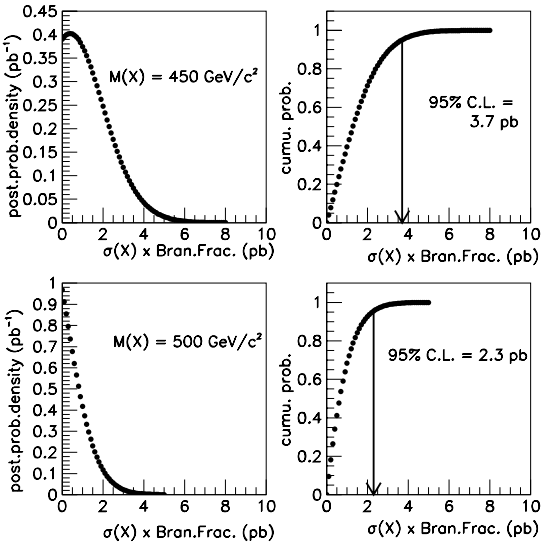

Figure 7.12: The posterior probability density and the cumulative probability vs. $\sigma_X B$ for $M_X = 450$ and 500 GeV/c^2. The arrow shows the 95% confidence level upper limit on $\sigma_X B$.

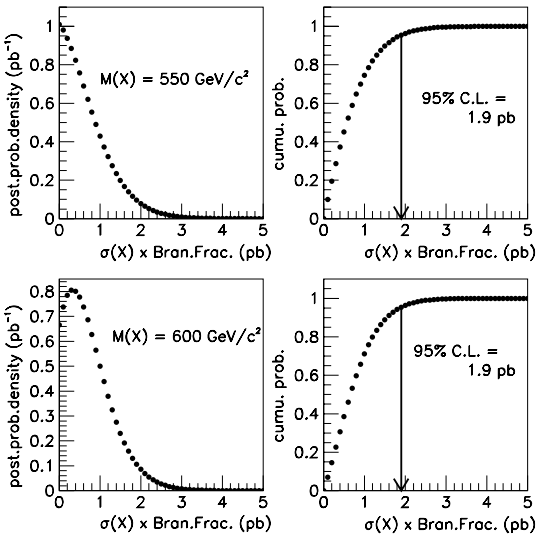

Figure 7.13: The posterior probability density and the cumulative probability vs. $\sigma_X B$ for $M_X = 550$ and 600 GeV/c^2. The arrow shows the 95% confidence level upper limit on $\sigma_X B$.

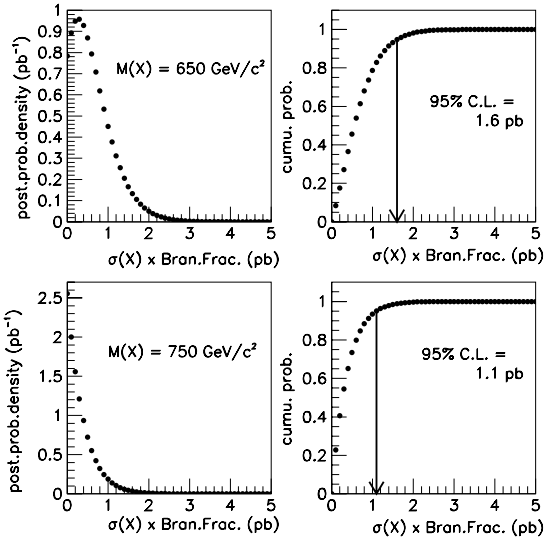

Figure 7.14: The posterior probability density and the cumulative probability vs. $\sigma_X B$ for $M_X = 650$ and 750 GeV/c^2. The arrow shows the 95% confidence level upper limit on $\sigma_X B$.

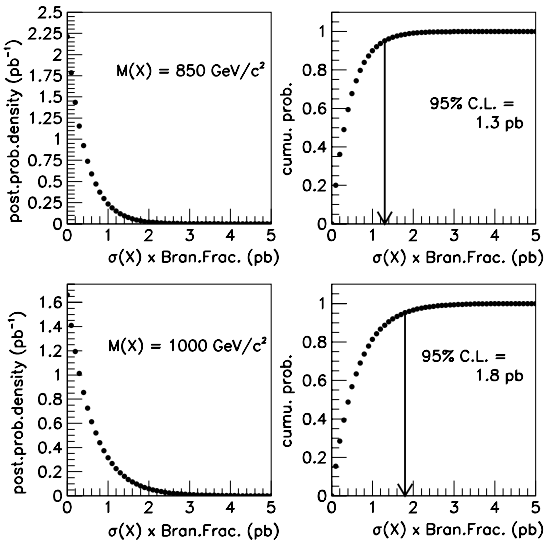

Figure 7.15: The posterior probability density and the cumulative probability vs. $\sigma_X B$ for $M_X = 850$ and 1000 GeV/c^2. The arrow shows the 95% confidence level upper limit on $\sigma_X B$.

Table 7.10: Integrated luminosity for the four lepton+jets channels.

	$\int Ldt\ (pb^{-1})$
e + jets	119.5 ± 5.1
μ + jets	107.7 ± 4.6
e + jets/μ	112.6 ± 4.8
μ + jets/μ	108.0 ± 4.6

0.78:0.22) are shown in Figure 7.16 as a function of M_X. We thus exclude at 95% C.L., the existence of a leptophobic X boson with $M_X < 580$ GeV/c^2.

We also conduct a study to obtain the 95% C.L. limits on $\sigma_X B$ for different values of M_X using a non-Bayesian approach. The definition for the likelihood function and the method employed to calculate the 95% C.L. upper limits on $\sigma_X B$ are discussed in Appendix E. It may be noted that the results obtained using the alternate approach are comparable to those obtained using Bayesian statistics.

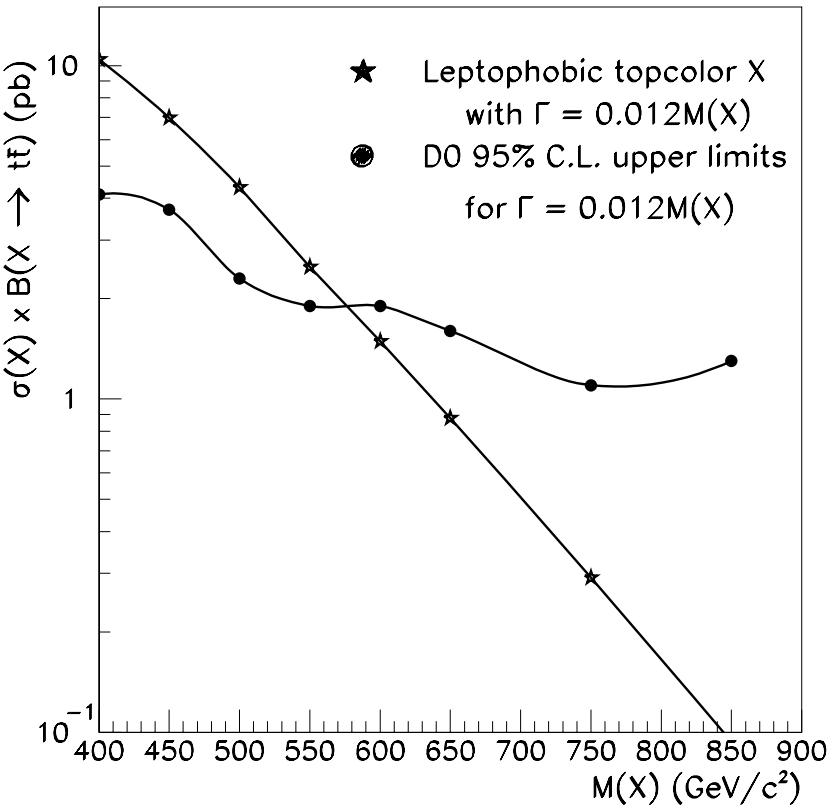

Figure 7.16: The DØ Run I 95% confidence level upper limits on $\sigma_X B$ as a function of resonance mass M_X. W+jets and multijets are combined in the ratio 0.78:0.22. Included for reference are the predicted topcolor assisted technicolor cross sections for a width, $\Gamma_X = 1.2\%\ M_X$.

Table 7.11: $\sum_i A_i \mathcal{L}_i$ for different M_X, with the statistical errors and the systematic errors from various sources.

M_X (GeV/c^2)	350	400	450	500	550	600	650	750	850	1000
$\sum_i A_i \mathcal{L}_i$	4.59	5.55	5.75	5.99	5.63	5.51	5.01	4.41	3.54	2.53
Statistical (ϵ^{sel})	0.167	0.184	0.187	0.192	0.192	0.190	0.176	0.167	0.145	0.126
Trigger	0.161	0.200	0.205	0.212	0.200	0.195	0.179	0.158	0.125	0.095
Electron-id	0.110	0.148	0.152	0.164	0.155	0.141	0.130	0.118	0.096	0.073
Isol.μ-id	0.130	0.145	0.152	0.148	0.138	0.152	0.134	0.126	0.096	0.057
Tag μ-id	0.020	0.022	0.022	0.026	0.024	0.025	0.026	0.022	0.019	0.012
Int. luminosity	0.176	0.239	0.243	0.255	0.239	0.237	0.214	0.195	0.155	0.110
Total quad. error	0.338	0.418	0.427	0.443	0.421	0.417	0.380	0.349	0.282	0.214

Table 7.12: The 95% C.L. upper limits on $\sigma_X B$ for narrow resonances of mass M_X and natural width $\Gamma_X = 0.012 M_X$ decaying into $t\bar{t}$. The top quark mass is chosen to be 175 GeV/c^2 and flat priors are assumed for the expected sources of signal and background.

M_X GeV/c^2	95% C.L. upper limits on $\sigma_X B$ (pb)
350	2.4
400	4.1
450	3.7
500	2.3
550	1.9
600	1.9
650	1.6
750	1.1
850	1.3
1000	1.8

Chapter 8

Systematic uncertainties and Results

The expected shapes of distributions for signal and background, and the acceptance of $X \to t\bar{t}$ events are subject to several sources of systematic uncertainty. Some of the major sources of systematic uncertainty are the following:

- uncertainty from jet energy scale
- initial–state and final–state radiation
- choice of parton distribution functions
- Monte Carlo generators
- scale used in Vecbos while modeling the W+jets background
- mass of top quark, m_t.

In this analysis, we study in detail (see below), the systematic uncertainties due to the jet energy scale, the effect of initial–state and final–state radiation, and the choice of parton distribution functions. As for the Monte

Carlo generators, only Isajet and Pythia have the process $X \to t\bar{t}$ included in them. For the present analysis we use Pythia for generating $X \to t\bar{t}$ and do not consider the systematic uncertainty due to the Monte Carlo generator, in detail, owing to limited support in accessing the Run I software. Regarding the choice of the Q^2 scale in Vecbos and fragmentation method, a comparison was made in the standard analysis to extract the top quark mass, to obtain the fitted top mass with the Q^2 set to the average jet p_T scale and the W mass, followed by both Isajet fragmentation as well as Herwig fragmentation. Since the choice of the average jet p_T with Herwig fragmentation was found to give intermediate results, we consider only the average jet p_T scale in Vecbos followed by fragmentation using Herwig, in the present analysis, and do not consider the effect of other choices in detail. Regarding the mass of the top quark, we consider it a parameter in the Monte Carlo event generators and choose a value of 175 GeV/c^2.

Jet energy scale

For the systematics due to jet energy scale, rather than considering the uncertainty in the absolute jet energy scale, we consider the uncertainty in the relative scale between data and Monte Carlo. This is estimated to be $\pm$(2.5% + 0.5 GeV) for each jet as discussed in Section 3.5.2. We therefore re-scale the jet energies by $\pm$(2.5% + 0.5 GeV) for the signal source ($X \to t\bar{t}$) for each M_X. The selection criteria discussed in Section 4.3 are then applied to the $m_{t\bar{t}}$ distributions for different M_X. The systematic uncertainty on the selection efficiency for any channel i due to the jet energy scale is then determined as

$\max(a_i,\ b_i)$, with $a_i = |\frac{\epsilon_i^{'sel} - \epsilon_i^{''sel}}{2}|$, and $b_i = |\epsilon_i^{'sel}(\epsilon_i^{''sel}) - \epsilon_i^{sel}|$. Here ϵ_i^{sel} is the selection efficiency with the nominal jet energy, and $\epsilon_i^{'sel}$ and $\epsilon_i^{''sel}$ are the selection efficiencies obtained after re-scaling the jet energies by +(2.5% + 0.5 GeV) and –(2.5% + 0.5 GeV) respectively. The errors for the different channels are added linearly to give the total systematic error due to the jet energy scale ($\delta\epsilon^{sel}(jetE)$) for any mass M_X. The values of $\delta\epsilon^{sel}(jetE)$ for different M_X are tabulated in Table 8.1.

Initial–state and final–state radiation (ISR/FSR)

For the systematics due to initial–state and final–state radiation (ISR/FSR), we consider a representative resonance mass $M_X = 500$ GeV/c^2. Using Pythia, we generate 1000 events for $X \to t\bar{t}$ using the parameters discussed in chapter 6, but with initial–state and final–state radiation switched off. The generated events are processed through the DØGEANT detector simulation package, musmear package and the DØ reconstruction package. Selections described earlier are then applied and the difference in the selection efficiencies with and without initial and final–state radiation is used to determine the systematic error from ISR/FSR. The errors for the different channels are added linearly to give the total systematic error $\delta\epsilon^{sel}(ISR/FSR)$. We observe that $\delta\epsilon^{sel}(ISR/FSR)$ is about 16% of $\sum_i A_i\mathcal{L}_i$ for $M_X = 500$ GeV/c^2. For all other M_X we then consider $\delta\epsilon^{sel}(ISR/FSR)$ to be 16% of $\sum_i A_i\mathcal{L}_i$. The values of $\delta\epsilon^{sel}(ISR/FSR)$ thus obtained are also tabulated in Table 8.1.

Parton distribution functions (pdf)

Regarding the choice of the parton distribution functions used, as mentioned in Section 6, we use CTEQ3M parton distribution functions in the present analysis. But for the study of systematic errors, we also consider the GRV94L parton distribution functions and recalculate the selection efficiency for 1000 events generated at $M_X = 500$ GeV/c^2. The difference in selection efficiencies for the two choices is used to estimate the systematic error due to the choice of parton distribution functions. The errors for the different channels are added linearly to give the total systematic error due to the choice of parton distribution functions. This is found to be 15% of $\sum_i A_i\mathcal{L}_i$ for $M_X = 500$ GeV/c^2. For all other M_X also, we consider $\delta\epsilon^{sel}(pdf)$ to be 15% of $\sum_i A_i\mathcal{L}_i$. The values of $\delta\epsilon^{sel}(pdf)$ are also tabulated in Table 8.1.

The total error on $\sum_i A_i\mathcal{L}_i$ (after combining the different error components listed in Table 7.11) is listed in Table 8.1 for different M_X.

8.1 Upper limits on $\sigma_X B$ including errors on $\mathcal{AL}$

The 95% C.L. upper limits on $\sigma_X B$ are re-computed for each M_X following the procedure discussed in Section 7.2 but with a Gaussian function incorporated for the acceptance times integrated luminosity ($\sum_i A_i\mathcal{L}_i$) as follows:

Table 8.1: The systematic uncertainty on ϵ^{sel} due to the jet energy scale, the initial–state/final–state radiation, and the choice of the parton distribution functions, as well as the total error on $\sum_i A_i\mathcal{L}_i$ for different M_X.

M_X (GeV/c^2)	350	400	450	500	550	600	650	750	850	1000
$\delta\epsilon^{sel}(jetE)$	0.324	0.411	0.322	0.255	0.282	0.283	0.232	0.192	0.221	0.159
$\delta\epsilon^{sel}(ISR/FSR)$	0.734	0.888	0.920	0.958	0.900	0.882	0.802	0.706	0.566	0.405
$\delta\epsilon^{sel}(pdf)$	0.689	0.832	0.863	0.899	0.845	0.827	0.752	0.662	0.531	0.380
Total quadratic error, $\delta(\sum_i A_i\mathcal{L}_i)$	1.11	1.35	1.37	1.41	1.34	1.31	1.26	1.05	0.855	0.61

$$P(\sigma_X B|D,M_X) = \frac{1}{\mathcal{N}'''}\int_{A\mathcal{L}}\int_{n_2}\int_{n_3} P(n_1,n_2,n_3|D,M_X) \times e^{-\frac{1}{2}\left(\frac{A\mathcal{L}-<\sum_i A_i\mathcal{L}_i>}{\delta(\sum_i A_i\mathcal{L}_i)}\right)^2} d(A\mathcal{L})dn_2dn_3, \quad (8.1)$$

where $<\sum_i A_i\mathcal{L}_i>$ is the measured value of $\sum_i A_i\mathcal{L}_i$ and $\delta(\sum_i A_i\mathcal{L}_i)$ is the error on it as listed in Table 7.11 and Table 8.1 respectively. The integration over $A\mathcal{L}$ in Eq. (8.1) is done using Monte Carlo techniques by defining $A\mathcal{L}$ as:

$$A\mathcal{L} = A\mathcal{L}_{min} + (A\mathcal{L}_{max} - A\mathcal{L}_{min}) \times x_c, \quad (8.2)$$

where x_c is a pseudo random number in [0,1] and $A\mathcal{L}_{min}$ and $A\mathcal{L}_{max}$ are chosen to be $\pm$ 5 $\times$ $\delta(\sum_i A_i\mathcal{L}_i)$ away from the mean value.

8.2 Results

The 95% C.L. upper limits on $\sigma_X B$ obtained after including all errors on $\mathcal{AL}$, the product of the acceptance of $X \to t\bar{t}$ events and the integrated luminosity of Run I data, are listed in Table 8.2 for different values of M_X. Upon comparing Tables 7.12 and 8.2 we observe that the errors on $\sum_i A_i \mathcal{L}_i$ do not have appreciable effect on the upper limits of $\sigma_X B$. The lower limit on M_X also shows a small change from a value of 580 GeV/c^2 to about 560 GeV/c^2 as seen from Figure 8.1. This result is not surprising since the statistical error due to only 41 events (after all selections) in the observed $m_{t\bar{t}}$ distribution dominates over the uncertainty in $\sum_i A_i \mathcal{L}_i$.

As discussed in Section 7.1, we consider flat prior probabilities for the signal and the two background sources. We also study the effect of Gaussian prior distributions for the two background sources, details of which can be found in Appendix F, but we do not find any significant change in the 95% C.L. upper limits of $\sigma_X B$.

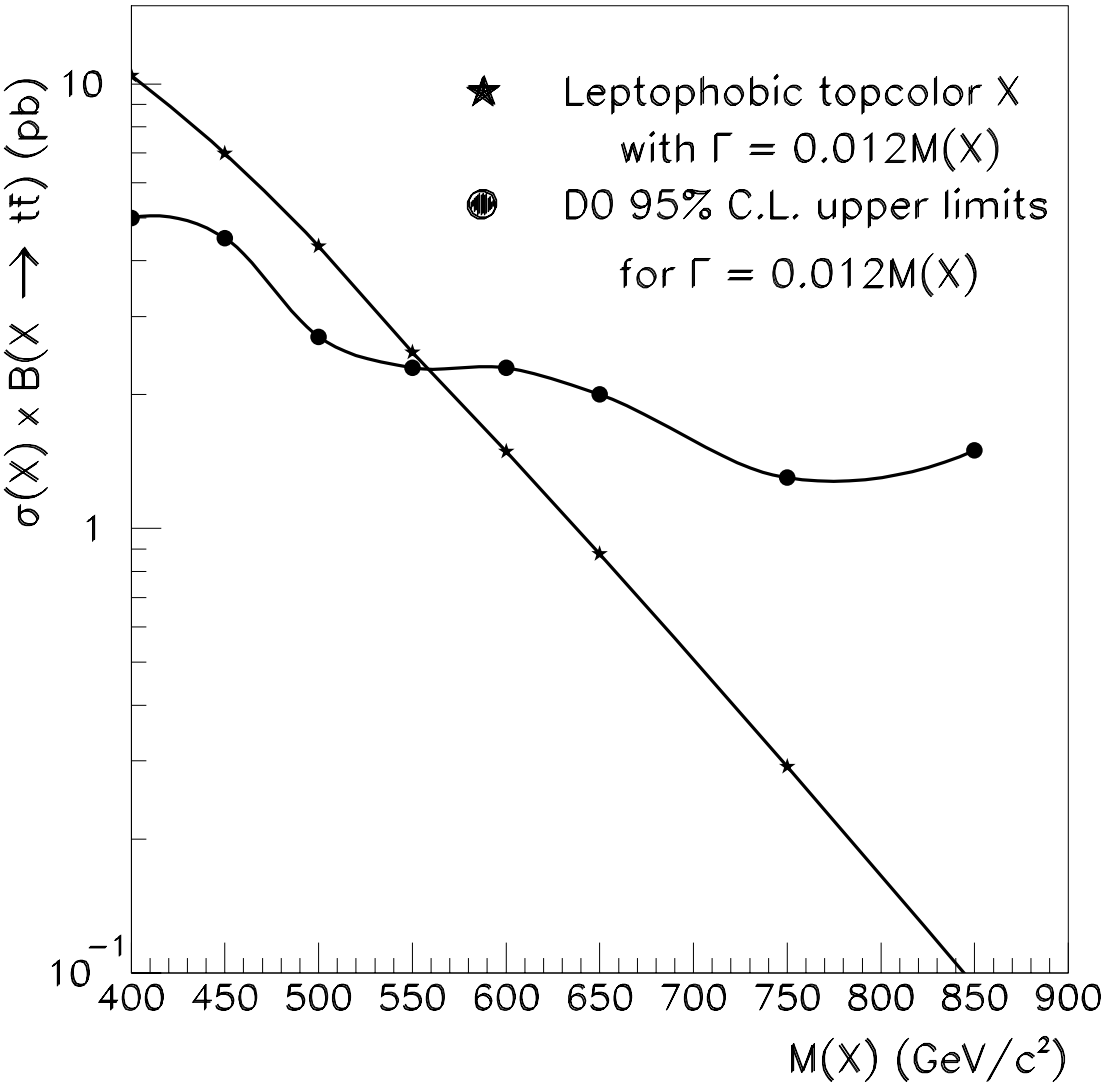

Figure 8.1: The DØ Run I 95% confidence level upper limits on $\sigma_X B$ as a function of resonance mass M_X. W+jets and multijets are combined in the ratio 0.78:0.22. The error on $\sum_i A_i \mathcal{L}_i$ is included as a Gaussian in the expression for the posterior probability density for $\sigma_X B$. Included for reference are the predicted topcolor assisted technicolor cross sections for a width, $\Gamma_X = 1.2\%\ M_X$.

Table 8.2: The 95% C.L. upper limits on $\sigma_X B$ for narrow resonances of mass M_X and width $\Gamma_X = 0.012 M_X$ decaying into $t\bar{t}$. Error on $\sum_i A_i \mathcal{L}_i$ is included as a Gaussian function. W+jets and multijets are combined in the ratio 0.78:0.22.

M_X (GeV/c^2)	95% C.L. upper limits on $\sigma_X B$ (pb)
350	3.0
400	5.0
450	4.5
500	2.7
550	2.3
600	2.3
650	2.0
750	1.3
850	1.5
1000	2.0

Chapter 9

Conclusions

In conclusion, we investigate the top-antitop invariant mass distribution in the lepton+jets channel using 130 pb^{-1} of Run I data recorded by the DØ detector from 1992–1996. We find that the $t\bar{t}$ invariant mass distribution agrees well with the Standard Model prediction, and there is no statistically significant evidence of an excess or a $t\bar{t}$ resonance in any observable range of $m_{t\bar{t}}$. We therefore establish upper limits, at 95 % confidence level (CL), on $\sigma_X B$, the product of the cross section of the heavy vector boson X and its branching fraction to $t\bar{t}$. Using a model of topcolor-assisted technicolor we also exclude at 95% CL the existence of a leptophobic X boson with $M_X < 560$ GeV/c^2 and width $\Gamma_X = 0.012 M_X$. The corresponding limits from the Collider Detector at Fermilab [12] are 480 GeV/c^2 for $\Gamma_X = 0.012 M_X$ at $\sqrt{s} = 1.8$ TeV.

With the onset of Run II at Tevatron, with a center of mass energy $\sqrt{s} =$ 1.96 TeV, we expect to collect about 20 times more integrated luminosity of data than was possible in Run I. We therefore expect that the $m_{t\bar{t}}$ spectrum will be understood at a deeper level in Run II, likely providing answers to

questions regarding any potential non–Standard Model excess and concerns about the behaviour near the $t\bar{t}$ threshold. Also, while the analysis presented in this thesis sets a lower limit on the mass of an X boson that is leptophobic and decays preferentially to $t\bar{t}$, it is not sensitive to the additional topcolor models presented in Ref. [11]. But the prospects for probing these and other non–Standard Model theories are promising for the Run II search for $X \rightarrow t\bar{t}$.

Appendix A

Jet-parton permutations

Consider the problem of jet permutations for more than four jets. There are two possibilities for dealing with an extra jet: it can be considered initial state radiation (ISR) and dropped from the problem, or it can be considered to have been radiated from one of the final state partons (final-state radiation, or FSR), in which case it should be merged with the appropriate jet. Let us assume that any additional jet is due to initial state radiation, and determine the number of possible jet-parton assignments for different numbers of jets in the final state.

In combinatorial terms, the problem can be stated as follows. Find all distinct ways of tagging N objects with the labels

- b_l, for the leptonic-side b,
- b_h, for the hadronic-side b,
- w, for the decay products of the hadronic W, and
- i, for initial state radiation,

subject to the conditions that there be at least one b_l, one b_h, and two w's. The number of such permutations grows extremely rapidly with N; the first few values are as follows:

$$\begin{array}{ll} N = 4 & 12 \\ N = 5 & 140 \\ N = 6 & 1020 \\ N = 7 & 5992 \end{array}$$

This combinatorial explosion is one of the main motivations for restricting the kinematic fit to just the four highest-E_T jets.

Appendix B

Simplification for $P(f_1, f_2, f_3|D, M_X)$

Substituting Eq. (7.13) in Eq. (7.14), we can re-write $P(f_1, f_2, f_3|D, M_X)$ as:

$$\begin{aligned} P(f_1, f_2, f_3|D, M_X) &= \prod_{i=1}^{M} \frac{1}{D_i!} \int_0^\infty da_{1i} \frac{exp[-(1+f_1)a_{1i}]a_{1i}^{A_{1i}}}{A_{1i}!} \int_0^\infty da_{2i} \frac{exp[-(1+f_2)a_{2i}]a_{2i}^{A_{2i}}}{A_{2i}!} \\ &\quad \times \int_0^\infty da_{3i} \frac{exp[-(1+f_3)a_{3i}]a_{3i}^{A_{3i}}}{A_{3i}!} (\sum_{j=1}^{3} f_j a_{ji})^{D_i} \end{aligned} \tag{B.1}$$

Expanding the sum over sources gives

$$(\sum_{j=1}^{3} f_j a_{ji})^{D_i} = D_i! \sum_{k_1,k_2,k_3=0}^{D_i} \frac{f_1^{k_1} a_{1i}^{k_1}}{k_1!} \frac{f_2^{k_2} a_{2i}^{k_2}}{k_2!} \frac{f_3^{k_3} a_{3i}^{k_3}}{k_3!} \tag{B.2}$$

where, for each count D_i, the indices k_j satisfy the multinomial constraint $\sum_{j=1}^{3} k_j = D_i$. Substituting Eq. (B.2) in Eq. (B.1) yields

$$P(f_1, f_2, f_3|D, M_X) = \prod_{i=1}^{M} \sum_{k1,k2,k3=0}^{D_i} \prod_{j=1}^{3} \frac{f_j^{k_j}}{A_{ji}! k_j!} \int_0^\infty da_{ji} exp[-(1+f_j)a_{ji}]a_{ji}^{A_{ji}+k_j}. \tag{B.3}$$

Thus the $(3M)$–dimensional integral separates into 3M one–dimensional integrals that can be evaluated in terms of Gamma functions. Upon doing so we get Eq. (7.15).

Appendix C

Electron ID efficiency for Monte Carlo events

We determine the overall MC electron identification efficiency (including the efficiency for tracking done during the reconstruction) by taking the ratio of the number of matched reconstructed electrons to the number of electrons at generator level with $p_T > 18$ GeV/c[1]. The algorithm used to determine the Monte Carlo electron identification efficiency at any resonance mass, M_X, is described below:

- We initialize the number of generator-level electrons, N_{gen}, and the number of matched reconstructed electrons, N_{reco}, to 0.
- We loop over all generator-level electrons in an event and find the highest p_T electron ("leading" electron).
- If in an event, the leading electron has $p_T > 18$ GeV/c, then

[1]The electron identification efficiencies for data are obtained for high p_T electrons with $p_T > 20$ GeV/c. In order to allow for a three standard deviation fluctuation in the electron p_T we consider a lower cut-off of 18 GeV/c on the electron p_T while determining the Monte Carlo electron identification efficiency.

  - We increment the number of generator-level electrons by one:
    $N_{gen} = N_{gen} + 1$
  - We loop over all reconstructed electrons in that event and compute the distance, ΔR, in η-ϕ space between the leading generator-level electron and the reconstructed electron.
  - We retain the reconstructed electron for which the distance ΔR is minimum.
  - If $\Delta R_{min} \leq 0.1$, then we call it a "matched" reconstructed electron and increment the number of matched reconstructed electrons by one:
    $N_{reco} = N_{reco} + 1$

- We repeat steps 2 and 3 for all events in the sample.
- We then define the Monte Carlo electron identification efficiency, $\epsilon^{e-ID}(\mathrm{MC})$, as:
  $\epsilon^{e-ID}(\mathrm{MC}) = \frac{N_{reco}}{N_{gen}}$.

Comparisons of the p_T distributions of the matched reconstructed electrons and the leading electrons at generator-level for Standard Model $t\bar{t}$ production[2] are shown in Figs. C.1-C.2. The values obtained for the Monte Carlo electron identification efficiency, $\epsilon^{e-ID}(\mathrm{MC})$, for the 10 different masses of X and also for Standard Model $t\bar{t}$ production are listed in Table C.1 below. The errors

[2]Along with the Monte Carlo samples generated at the 10 different masses of X, we also generated 10000 events for Standard Model $t\bar{t}$ production in a similar way using Pythia.

shown on ϵ^{e-ID}(MC) are statistical[3].

Table C.1: The Monte Carlo electron identification efficiency, ϵ^{e-ID}(MC), for different M_X and for Standard Model (SM) $t\bar{t}$ production in the CC and EC. The errors shown are statistical.

	ϵ^{e-ID}_{CC}(MC)	ϵ^{e-ID}_{EC}(MC)
$M_X = 350$	0.628 ± 0.018	0.461 ± 0.027
$M_X = 400$	0.648 ± 0.019	0.459 ± 0.026
$M_X = 450$	0.625 ± 0.018	0.451 ± 0.027
$M_X = 500$	0.636 ± 0.018	0.474 ± 0.027
$M_X = 550$	0.624 ± 0.018	0.465 ± 0.027
$M_X = 600$	0.618 ± 0.018	0.450 ± 0.026
$M_X = 650$	0.601 ± 0.018	0.440 ± 0.025
$M_X = 750$	0.557 ± 0.018	0.457 ± 0.025
$M_X = 850$	0.547 ± 0.018	0.446 ± 0.025
$M_X = 1000$	0.491 ± 0.018	0.435 ± 0.024
SM $t\bar{t}$ production	0.630 ± 0.018	0.468 ± 0.027

In order to make the acceptance of the Monte Carlo signal events represent that of Run I data, we now need to multiply the signal acceptance by the data electron identification efficiency, ϵ^{e-ID}(data), and divide it by the Monte Carlo electron identification efficiency, ϵ^{e-ID}(MC). But from Table C.1 we see that, whereas ϵ^{e-ID}(MC) is fairly stable with increasing M_X in the EC, that is not the case in the CC. The Monte Carlo identification efficiency for electrons in the CC is fairly stable for values of M_X between 350-600 GeV/c^2

[3]We define the error $\delta\epsilon^{e-ID}$(MC) as:

$(\frac{\delta\epsilon^{e-ID}(\mathrm{MC})}{\epsilon^{e-ID}(\mathrm{MC})})^2 = (\frac{\delta N_{\mathrm{reco}}}{N_{\mathrm{reco}}})^2 + (\frac{\delta N_{\mathrm{gen}}}{N_{\mathrm{gen}}})^2$,

where $\delta N_{\mathrm{reco(gen)}} = \sqrt{N_{\mathrm{reco(gen)}}}$.

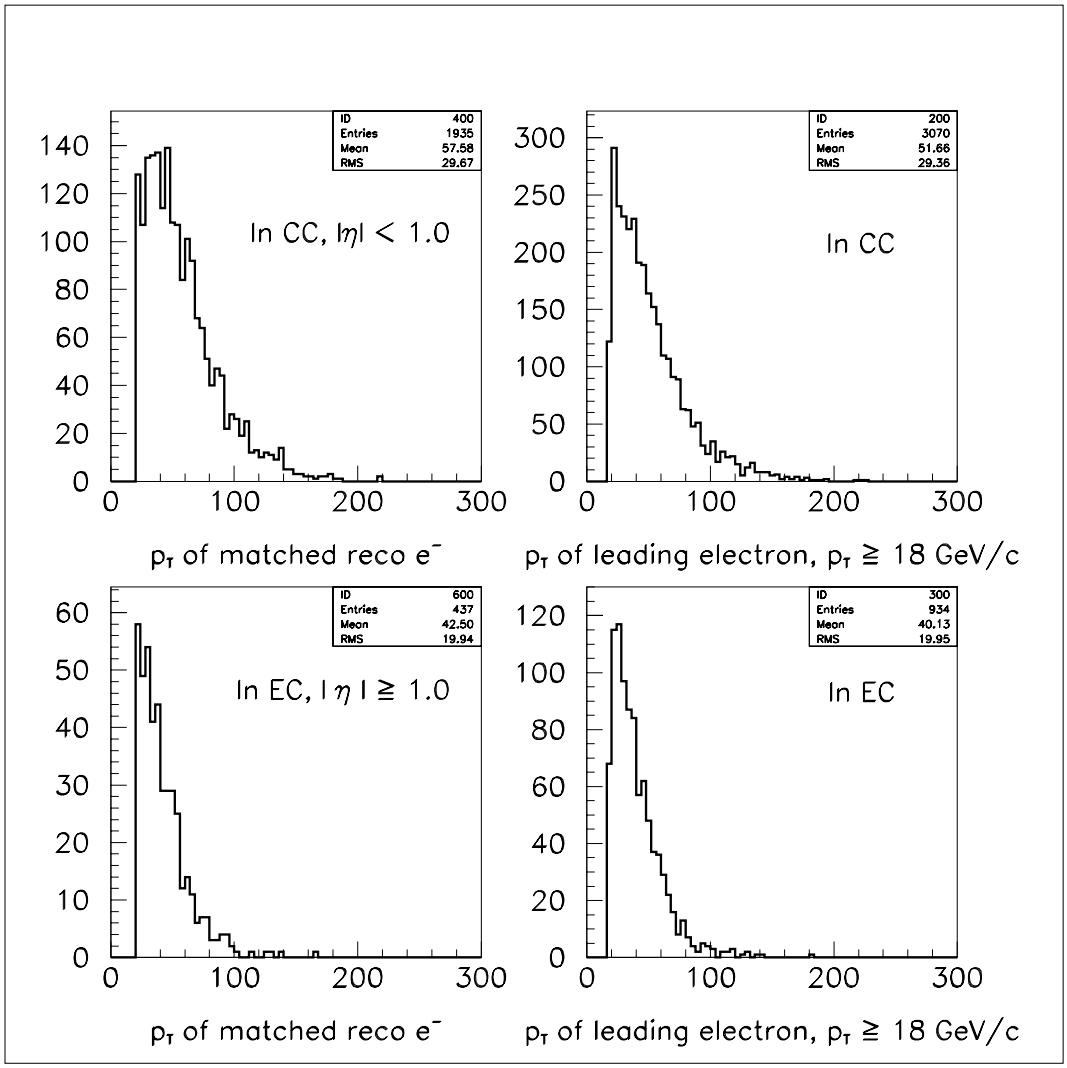

Figure C.1: The transverse momentum, p_T, of the matched reconstructed electron and the leading electron at generator-level with $p_T > 18$ GeV/c, in the **CC** and the **EC**, for a sample of Standard Model $t\bar{t}$ production generated using Pythia.

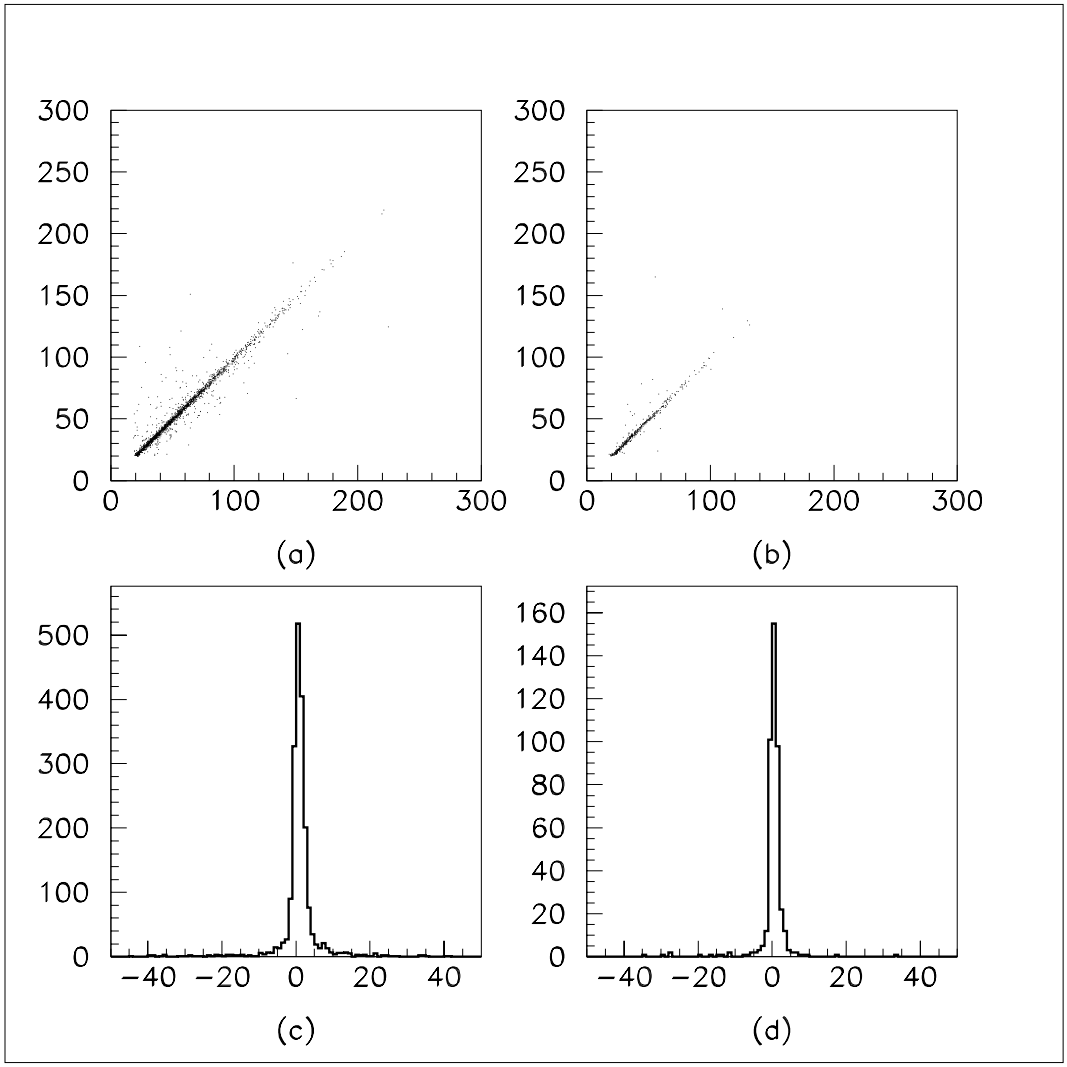

Figure C.2: Plots (a) and (b) show the p_T of the matched reconstructed electron versus the p_T of the leading electron at generator-level, in the CC and EC respectively, for a sample of Standard Model $t\bar{t}$ production generated using Pythia. Plots (c) and (d) show the histograms for the difference between the p_T of the matched reconstructed electron and that of the leading electron at generator-level, in the CC and EC respectively.

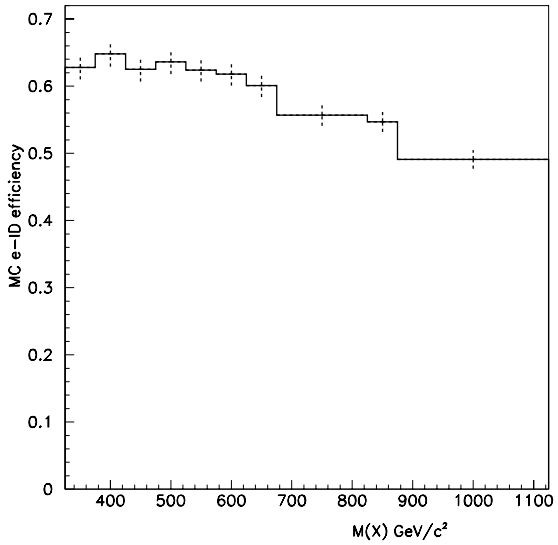

Figure C.3: The Monte Carlo electron identification efficiency in the CC versus M_X. The errors shown are statistical.

but decreases rapidly for higher M_X. This may be a physics effect due to the mass of the resonance. We do not understand it exactly yet. Therefore to correctly account for the Monte Carlo electron identification in our calculation of the acceptance we consider the values obtained in the CC and EC from the Monte Carlo sample of Standard Model $t\bar{t}$ production generated using Pythia. We do this since the value of ϵ_{CC}^{e-ID}(MC) from this sample is similar to that in the plateau region in the plot of ϵ_{CC}^{e-ID}(MC) versus M_X as seen in Figure C.3. We therefore consider the electron identification efficiency for Monte Carlo events as:

$$\epsilon_{CC}^{e-ID}(MC) \;=\; 0.630 \pm 0.018, \text{ in the CC} \tag{C.1}$$

$$\epsilon_{EC}^{e-ID}(MC) \;=\; 0.468 \pm 0.027, \text{in the EC.} \tag{C.2}$$

Appendix D

Correction for the branching fraction ($\mathcal{B}$)

In order to increase the efficiency in the processing of lepton plus jets events, while modelling the resonance signal $X \rightarrow t\bar{t}$ using Pythia Monte Carlo generator, one of the W bosons is forced to decay to one of the three lepton families (e, μ or τ). The decay modes for the other W boson are left unconstrained. While calculating the acceptance for the signal we therefore need to correct for the forced decay of one of the W bosons. We do this by considering a branching fraction, $\mathcal{B}$, in the acceptance A defined as:

$$A = \epsilon^{trig} \times \epsilon^{pid} \times \epsilon^{sel} \times \mathcal{B}, \tag{D.1}$$

where ϵ^{trig} is the trigger efficiency, ϵ^{pid} is the efficiency for lepton identification (isolated leptons (e or μ) and tag-muon), and ϵ^{sel} is the efficiency of offline selection cuts.

With the above prescription for W boson decays, we always have at least one lepton in the final state; therefore we use a factor of 5/9 for the branching fraction which is the probability of getting at least one lepton in a $t\bar{t}$ decay.

This can be seen from Table D.1 which displays the W^+W^- decay branching fractions and the resulting $t\bar{t}$ final state combinations.

Table D.1: $t\bar{t}$ branching fractions can be read off from the table which displays the W^+W^- decay branching fractions, and the resulting $t\bar{t}$ final state combinations. It can be seen that the total branching fraction for $t\bar{t}$ to lepton plus jets is 36/81 and to dileptons is 9/81.

W^+W^- decay modes	$W^+ \to c\bar{s}$, $u\bar{d}$ (6/9)	$W^+ \to e^+\nu_e$ (1/9)	$W^+ \to \mu^+\nu_\mu$ (1/9)	$W^+ \to \tau^+\nu_\tau$ (1/9)
$W^- \to \bar{c}s$, $\bar{u}d$ (6/9)	36/81	6/81	6/81	6/81
$W^- \to e^-\bar{\nu}_e$ (1/9)	6/81	1/81	1/81	1/81
$W^- \to \mu^-\bar{\nu}_\mu$ (1/9)	6/81	1/81	1/81	1/81
$W^- \to \tau^-\bar{\nu}_\tau$ (1/9)	6/81	1/81	1/81	1/81

But since in our prescription of Monte Carlo generation, the hadronic decay modes of one of the W bosons are not allowed, the ratio of dilepton events to single lepton events is 1/2 as opposed to 1/4 in case of unconstrained decays as seen from Table D.2.

Table D.2: Branching fractions for $t\bar{t}$ decay with leptons in the final state under unconstrained and constrained decay modes for the W bosons.

	Unconstrained $t\bar{t}$ decay	Constrained $t\bar{t}$ decay (used in Pythia)
$\geq$1 lepton	5/9	1
only 1 lepton	4/9	2/3
2 leptons	1/9	1/3

One way to correct for this discrepancy is to randomly remove half the dilepton events before the output events from Pythia are processed through DØGEANT. In that case, the selection efficiency, ϵ^{sel}, defined as:

$$\epsilon^{sel} = N_{pass}/N_{gen}, \tag{D.2}$$

where N_{pass} is the number of events that pass the offline selections and N_{gen} is the number of events generated by Pythia, will be redefined as:

$$\epsilon^{sel} = N_{pass}/N'_{gen}, \tag{D.3}$$

where $N'_{gen} < N_{gen}$ ($N'_{gen} = N_{gen} - N_{dilep}/2$, with N_{dilep} being the number of dilepton events).

Alternatively, if N_{pass} does not have significant contribution from dilepton events, then without removing half the number of dilepton events at the generator level, we can consider the selection efficiency as defined by Eq. (D.2) but with a correction factor of N_{gen}/N'_{gen} in the numerator. We explain below in detail how we determine this correction factor with reference to a sample of Standard Model $t\bar{t}$ production.

We generate 10000 events, for Standard Model $t\bar{t}$ production, using Pythia event generator. One of the W bosons is forced to decay only leptonically whereas the decay modes for the other W boson are left unconstrained. We then count the number of single lepton ($N_{1\ lep}$) and dilepton (N_{dilep}) events, as $N_{1\ lep} = 6689$, and $N_{dilep} = 3311$. With $N_{gen} = 10000$, $N'_{gen} = N_{gen}$ - $N_{dilep}/2$ = 8344.5. The correction factor is then determined as:

$$N_{gen}/N'_{gen} = 10000/8344.5 = 1.2. \tag{D.4}$$

In Table D.3 we list the correction factors determined in a similar way for the 10 different masses of X considered in the present analysis. Therefore while calculating the acceptance of the signal sample (X $\rightarrow t\bar{t}$), using Eq. (D.1), we use Eq. (D.2) for the selection efficiency, ϵ^{sel}, and a value of $5/9 \times 1.2$ for the branching fraction, $\mathcal{B}$, assuming that the number of dilepton events passing our selection criteria is negligible.

Table D.3: The correction factor N_{gen}/N'_{gen} determined using Pythia for different values of M_X.

M_X (GeV/c^2)	N_{gen}/N'_{gen}
350	1.2
400	1.19
450	1.19
500	1.2
550	1.19
600	1.19
650	1.19
750	1.2
850	1.19
1000	1.19

Appendix E

$(\sigma_X B)_{95}$ using an alternate approach

The 95% C.L. upper limits on $\sigma_X B$ for different values of M_X are also obtained using an alternate definition for the likelihood function. We consider the following three sources for fitting the observed lepton+jets data:

- Signal (s): X $\rightarrow t\bar{t}$
- Background 1 (b_1): Standard Model $t\bar{t}$ production generated using Herwig
- Background 2 (b_2): W+jets and multijets combined in the ratio 0.78:0.22.

We define the likelihood function as:

$$L = \prod_i P_i, \tag{E.1}$$

where the product is over different bins in the $m_{t\bar{t}}$ distribution and P_i is the Poisson probability for observing d_i data events in the i^{th} mass bin and is given

by:

$$P_i = \frac{\lambda_i^{d_i} exp(-\lambda_i)}{d_i!}. \tag{E.2}$$

Here, λ_i is the expected number of events in the i^{th} mass bin and is given by:

$$\lambda_i = N_i(s) + \alpha * N_i(b_1) + \beta * N_i(b_2), \tag{E.3}$$

where N(b_1) and N(b_2) are the Monte Carlo (MC) counts for backgrounds 1 and 2 respectively but normalized to unity and N(s) is the MC count for signal normalized to n_1 given by Eq. (7.19).

We vary n_1 by considering different points on the $\sigma_X B$ axis in steps of 0.2 and use the CERN minimization program MINUIT [49] to determine at each point on the $\sigma_X B$ axis, the values of α and β that maximize the likelihood function defined by Eq. (E.1). Since N(b_1) and N(b_2) are normalized to unity, the maximum likelihood estimates of α and β represent the expected number of Standard Model $t\bar{t}$ as well as W+jets and multijet events, respectively. We then set the 95% C.L. upper limits on $\sigma_X B$ by integrating the likelihood as a fuction of $\sigma_X B$ and finding the 95% area under the curve. The limits are determined using two different approaches in MINUIT:

- In the first approach, α and β are constrained to be > 0 in MINUIT to ensure that each of the maximum likelihood estimates from the three sources, $< n_1 >$, $< n(b_1) >$ and $< n(b_2) >$, is always greater than zero. The corresponding 95% C.L. upper limits on $\sigma_X B$ for different values of M_X are listed in Table E.1.

  The plots of the posterior probability density for different values of M_X are shown in Figure E.1. In Figure E.2 the values of $\sigma_X B$ for different

M_X as obtained using a model of topcolor-assisted technicolor and the corresponding 95% C.L. upper limits are shown.

- In the second approach, α and β are unconstrained; but after maximizing the likelihood, we check that the sum of the maximum likelihood estimates from the three sources ($< n_1 > + < n(b_1) > + < n(b_2) >$) is positive. The corresponding 95% C.L. upper limits on $\sigma_X B$ for different values of M_X are also listed in Table E.1.

  The plots of the posterior probability density for different values of M_X are shown in Figure E.3. In Figure E.4 the values of $\sigma_X B$ for different M_X as obtained using a model of topcolor-assisted technicolor and the corresponding 95% C.L. upper limits are shown.

It may be noted that the results in both cases are comparable. The results using an alternate definition for the likelihood function are also comparable to those obtained using the Bayesian approach, as can be seen by comparing Tables 7.12 and E.1.

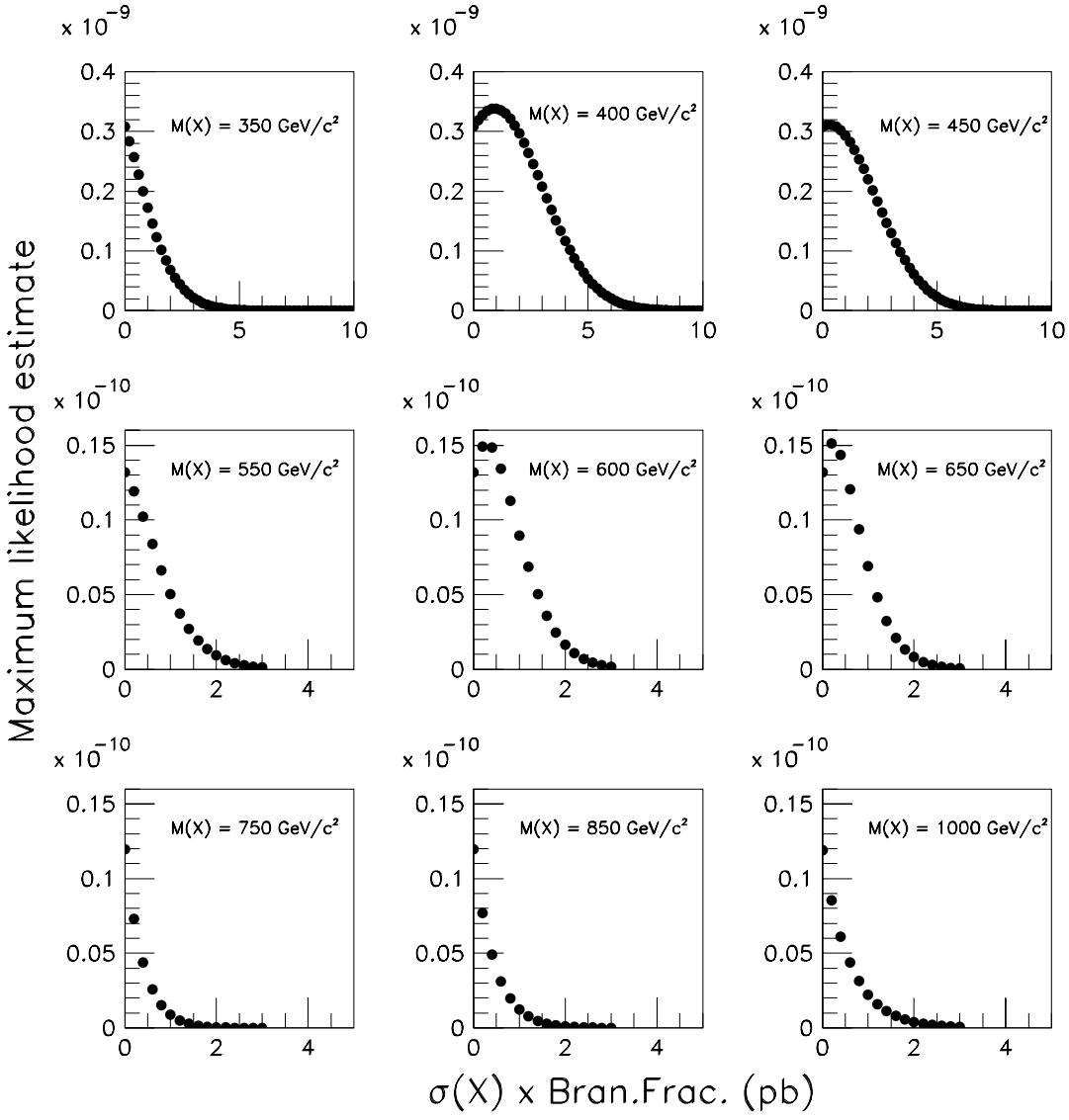

Figure E.1: The maximum likelihood estimate vs. $\sigma_X B$ for different M_X. While maximizing the likelihood, the parameters α and β are constrained to be > 0 in MINUIT.

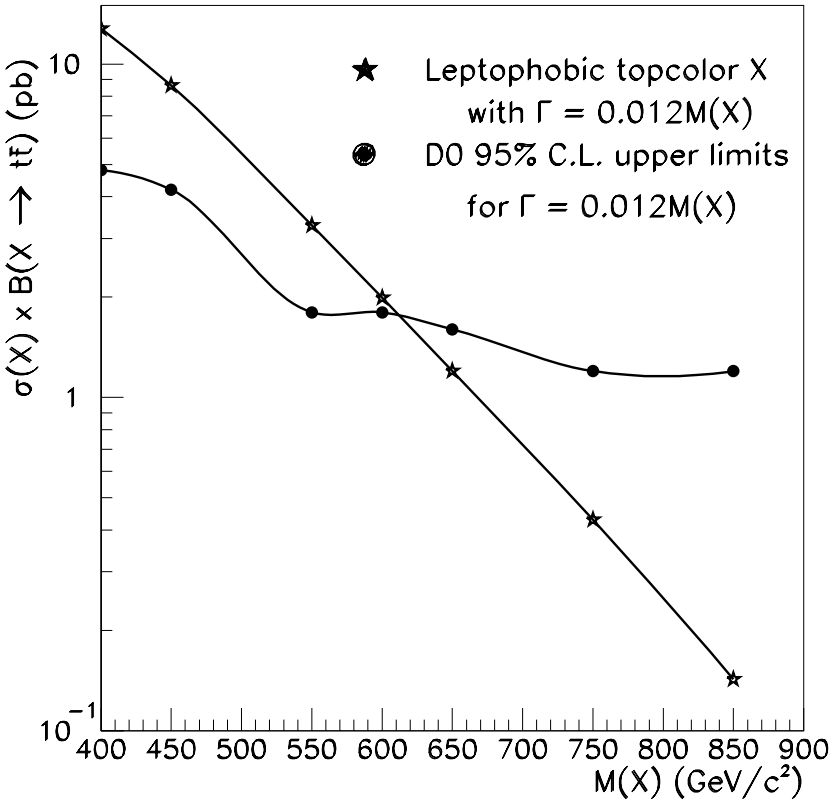

Figure E.2: The DØ Run I 95% confidence level upper limits on $\sigma_X B$ as a function of resonance mass M_X. While maximizing the likelihood, the parameters α and β are constrained to be > 0 in MINUIT. Included for reference are the predicted topcolor assisted technicolor cross sections for a width, $\Gamma_X = 1.2\%\ M_X$.

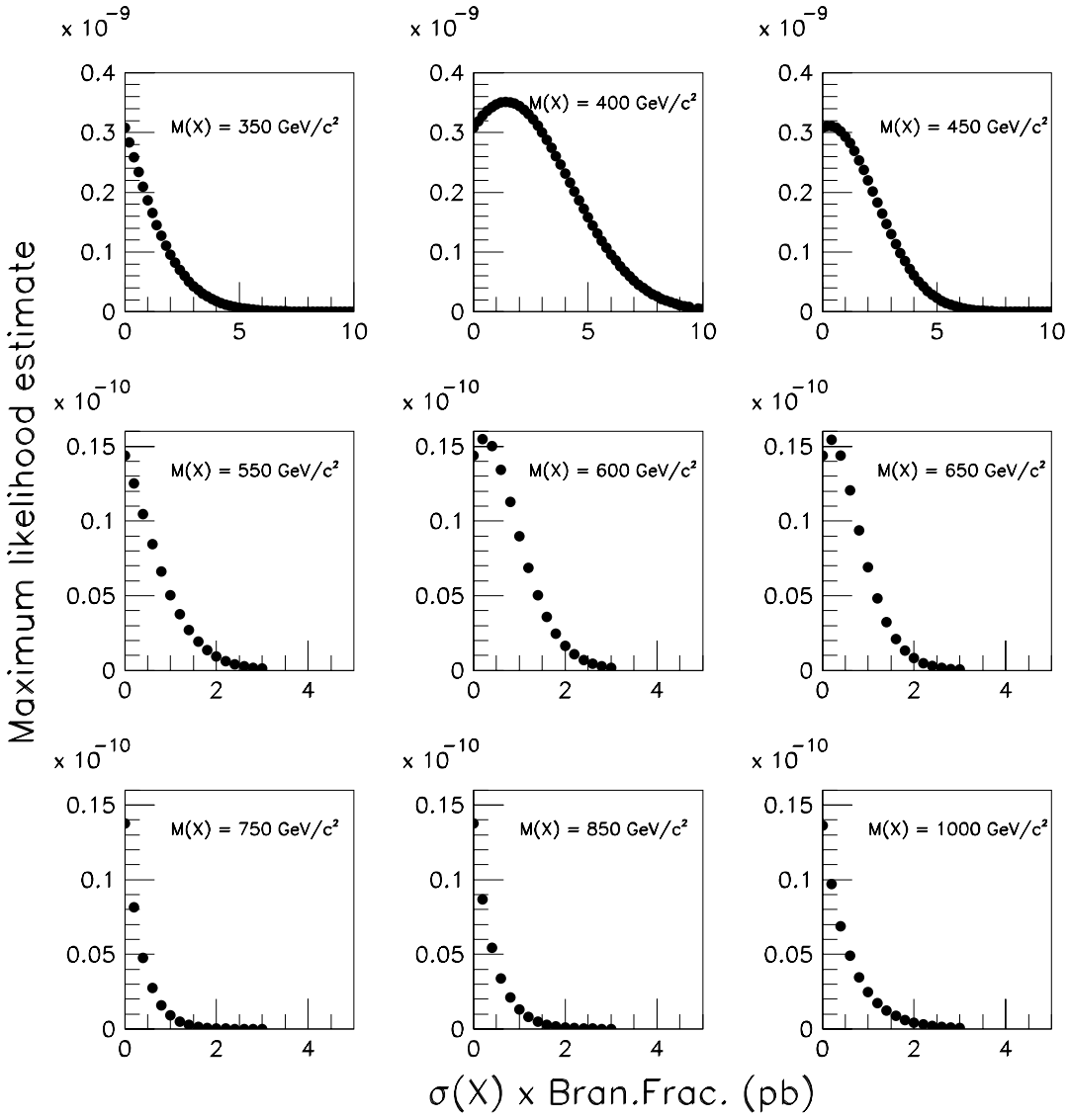

Figure E.3: The maximum likelihood estimate vs. $\sigma_X B$ for different M_X. While maximizing the likelihood, no constraint is applied on the parameters α and β in MINUIT.

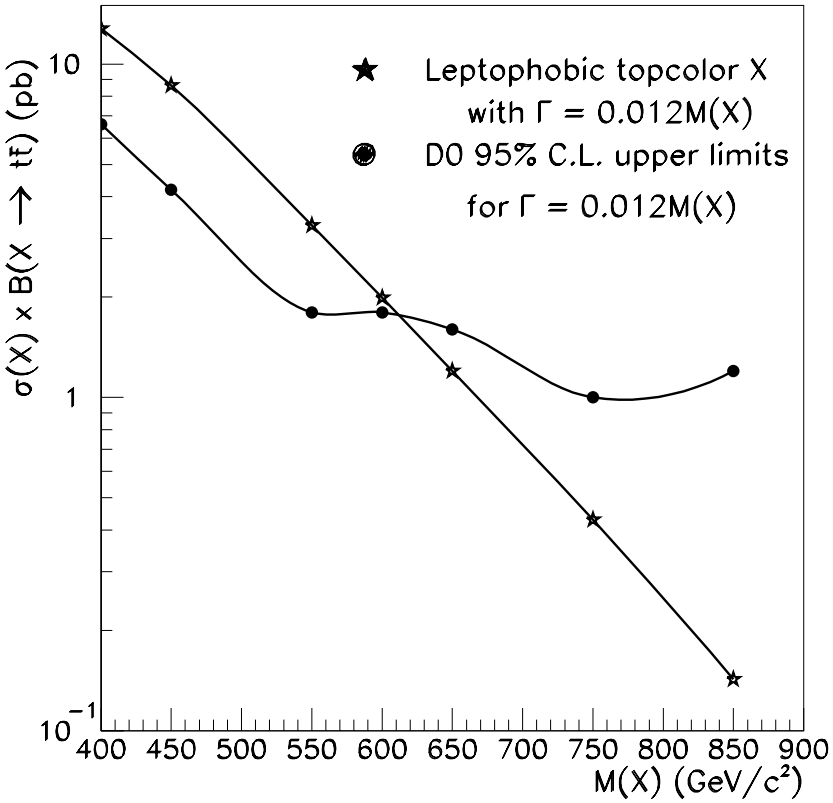

Figure E.4: The DØ Run I 95% confidence level upper limits on $\sigma_X B$ as a function of resonance mass M_X. While maximizing the likelihood, no constraint is applied on the parameters α and β in MINUIT. Included for reference are the predicted topcolor assisted technicolor cross sections for a width, $\Gamma_X = 1.2\%$ M_X.

Table E.1: The 95% C.L. upper limits on $\sigma_X B$ for narrow resonances of mass M_X and width $\Gamma_X = 0.012 M_X$ decaying into $t\bar{t}$.

	95% C.L. upper limits on $\sigma_X B$ (pb)	
$M_X(\mathrm{GeV}/c^2)$	(α, $\beta > 0$ in Minuit)	(α, β unconstrained in Minuit)
350	2.8	3.6
400	4.8	6.6
450	4.2	4.2
550	1.8	1.8
600	1.8	1.8
650	1.6	1.6
750	1.2	1.0
850	1.2	1.2
1000	1.8	1.6

Appendix F

$(\sigma_X B)_{95}$ with Gaussian priors for backgrounds

As discussed in Section 7.1, since we do not know a priori which source of signal or background is more favored than the other, we assume that each of the three sources being fitted to the observed $m_{t\bar{t}}$ distribution, is equally likely. We therefore consider a 'flat' prior for each source while constructing the posterior probability distribution for $\sigma_X B$. But we study the effect of a Gaussian prior also for the background sources, and consider the following two cases:

Case A

We consider a Gaussian prior for the background from Standard Model $t\bar{t}$ production. We convolute the posterior probability density for $\sigma_X B$ with a Gaussian distribution with the mean number of expected counts from Standard Model $t\bar{t}$ production, $< n_2 > = 23.6$, and standard deviation[1], $\delta(n_2) = 3.8$.

[1]The values for the mean number of expected counts from Standard Model $t\bar{t}$ production, $< n_2 >$, and standard deviation, $\delta(n_2)$, are obtained from Table 7.1 by appropriately combining the $< n_2 >$ values for M_X = 400–1000 GeV/c^2.

That is, we re-write Eq. (8.1) as:

$$P(\sigma_X B|D, M_X) \propto \int_{A\mathcal{L}} \int_{n_2} \int_{n_3} P(n_1, n_2, n_3|D, M_X) e^{-\frac{1}{2}(\frac{A\mathcal{L} - <\sum_i A_i \mathcal{L}_i>}{\delta(\sum_i A_i \mathcal{L}_i)})^2} e^{-\frac{1}{2}(\frac{n_2 - <n_2>}{\delta(n_2)})^2} d(A\mathcal{L}) dn_2 dn_3. \quad \text{(F.1)}$$

The 95 % CL upper limits on $\sigma_X B$ thus obtained are listed in Table F.1.

Case B

We consider Gaussian priors for the background from Standard Model $t\bar{t}$ production, as well as from W+jets and multijets. We convolute the posterior probability density for $\sigma_X B$ with Gaussian distributions for the two sources of background with the following mean values and standard deviations obtained as for Case A above:

$$< n_2 >= 23.6 \quad \text{(F.2)}$$

$$\delta(n_2) = 3.8 \quad \text{(F.3)}$$

$$< n_3 >= 14.2 \quad \text{(F.4)}$$

$$\delta(n_3) = 3.4 \quad \text{(F.5)}$$

We re-write Eq. (8.1) as:

$$P(\sigma_X B|D, M_X) \propto \int_{A\mathcal{L}} \int_{n_2} \int_{n_3} P(n_1, n_2, n_3|D, M_X) e^{-\frac{1}{2}(\frac{A\mathcal{L} - <\sum_i A_i \mathcal{L}_i>}{\delta(\sum_i A_i \mathcal{L}_i)})^2} e^{-\frac{1}{2}(\frac{n_2 - <n_2>}{\delta(n_2)})^2} \; e^{-\frac{1}{2}(\frac{n_3 - <n_3>}{\delta(n_3)})^2} \; d(A\mathcal{L}) dn_2 dn_3. \quad \text{(F.6)}$$

The 95 % CL upper limits on $\sigma_X B$ thus obtained are listed in Table F.1.

Upon comparing Tables 8.2 and F.1, we find that choosing Gaussian prior distributions for the background sources instead of flat prior distributions,

Table F.1: The 95% CL upper limits on $\sigma_X B$ with Gaussian priors for backgrounds. The effect of errors on $\mathcal{AL}$ is included.

	95% C.L. upper limits on $\sigma_X B$ (pb)	
$M_X(\mathrm{GeV}/c^2)$	Case A	Case B
400	5.0	3.7
450	4.4	3.4
500	2.8	2.4
550	2.3	2.1
600	2.4	2.2
650	2.0	1.9
750	1.3	1.3
850	1.5	1.5
1000	2.2	2.3

produces no significant change on the upper limits on $\sigma_X B$, at 95 % CL. We may therefore assume flat prior distributions for all sources and claim our maximal ignorance of their prior distributions.

Bibliography

[1] Review of Particle Physics, Phys. Rev. **D**, Vol. 66(I): 23-29 (2002).

[2] Gordon L. Kane. Top Quark Topics. In J. Hawthorne, editor, *Gauge Bosons and Heavy Quarks: Proceedings of the Eighteenth SLAC Summer Institute on Particle Physics*, pages 123-142. SLAC-REPORT-378, July, 1990.

[3] R. Cahn, Rev. Mod. Phys. **68**, 951 (1996); N. Cabibbo, Phys. Rev. Lett. **10**, 531, (1963); M. Kobayashi and T. Maskawa, Prog. Theor. Phys. **49**, 652, (1973).

[4] J. L. Hewett, "The Standard Model and why we believe it", hep-ph/9810316.

[5] S. Martin, "A Supersymmetric Primer", hep-ph/9709356.

[6] S. Weinberg, Phys. Rev. **D13**, 974 (1976); L. Susskind, Phys. Rev. **D20**, 2619 (1979); S. Dimopoulos, L. Susskind, Nucl. Phys. **B155**, 237 (1979); E. Eichten, K. Lane, Phys. Lett. **B90**, 125 (1980).

[7] T. Appelquist, R. Shrock, Neutrino Masses in Theories with Dynamical Electroweak Symmetry Breaking, hep-ph/0204141.

[8] C. T. Hill, Phys. Lett. **B266**, 419 (1991);
S. P. Martin, Phys. Rev. **D45**, 4283 (1992), *ibid* **D46**, 2197 (1992); Nucl. Phys. **B398**, 359 (1993).

[9] V. A. Miransky, M. Tanabashi, K, Yamawaki, Phys. Lett. **B221**, 177 (1989); Mod. Phys. Lett. **A4**, 1043 (1989);
W. A. Bardeen, C. T. Hill, M. Lindler, Phys. Rev. **D41**, 1647 (1990).

[10] C. T. Hill, Phys. Lett. **B345**, 483 (1995).

[11] R. M. Harris, C. T. Hill and S. Parke, Cross section for Topcolor Z'_t decaying to $t\bar{t}$, arXiv:hep-ph/9911288 (1999).

[12] T. Affolder *et al.* (CDF Collaboration), Phys. Rev. Lett. **85** , 2062 (2000).

[13] S. Abachi *et al.* Nucl. Inst. Meth., **A338** , 185-253 (1994).

[14] Helen T.Edwards, *Ann. Rev. Nucl. Part. Sci.*, **35:** 605-660, 1985.

[15] M.P.Church and J.P.Marriner, *Ann. Rev. Nucl. Part. Sci.*, **43:** 253-295, 1993.

[16] D. Mohl, G.Petrucci, L.Thorndahl, and S.van der Meer, *Phys. Rep.*, **C 58:** 73-119, 1980.

[17] William Joseph Thompson, *Search for the top quark in the muon + jets channel at DØ*, Ph.D thesis, State University of New York at Stony Brook, Stony Brook, New York (1994).

[18] Richard Fernow, Introduction to Experimental Particle Physics, Cambridge University Press (1992).

[19] C. Brown *et al.* Nucl. Inst. Meth., **A279** , 331-338 (1989).

[20] James Herbert Cochran, Jr., *Search for the truth in the eμ channel at DØ*, Ph.D thesis, State University of New York at Stony Brook, Stony Brook, New York (1993).

[21] B.S. Acharya *et al.* (DØ Collaboration), Nucl. Inst. Meth., **A401** , 45-62 (1997).

[22] John M. Butler, Main Ring Deadtime, DØ note 1682 (1993).

[23] V.M. Abazov *et al.* (DØ Collaboration), *$t\bar{t}$ Production Cross Section in $p\bar{p}$ collisions at $\sqrt{s}$ = 1.8 TeV*, (submitted to Phys. Rev. D).

[24] Srinivasan Rajgopalan, *The dE/dx capabilities of the DØ tracking system*, Ph.D thesis, Northwestern University, Evanston, Illinois (1992); Ties Behnke, *The Central Drift chamber for the DØ Detector: Design, Construction, and Test*, Ph.D thesis, State University of New York at Stony Brook, Stony Brook, New York (1989); Domenico Pizzuto, *DØ Central Tracking chamber Performance Studies*, State University of New York at Stony Brook, Stony Brook, New York (1991); Jeffrey W. Bantly, *The DØ Detector Forward Drift Chamber Performance and Physics Capability in the 1990 FNAL Testbeam Run*, Ph.D thesis, Northwestern University, Evanston, Illinois (1992).

[25] Jonathan Kotcher, *Response of the DØ Calorimeter to Cosmic Ray Muons*, Ph.D thesis, New York University, New York (1992).

[26] Myungyun Pang, *Search for top in $p\bar{p}$ collisions at $\sqrt{s}$ = 1.8 TeV by constrained kinematic fitting*, Ph.D thesis, Iowa State University, Ames, Iowa (1994).

[27] Jaehoon Yu, *Determination of the strong coupling constant (α_s) and a test of perturbative QCD using W+jets processes in the DØ detector*, Ph.D thesis, State University of New York at Stony Brook, Stony Brook, New York (1993).

[28] J. Kotcher (DØ Collaboration), in *1994 Beijing Calorimeter Symposium, Beijing, China*, edited by H.S.Chen (IHEP, Beijing, 1994); J. Guida (DØ Collaboration), Nucl. Phys. Proc. Suppl. **44**, 153 (1995).

[29] J. Womersley (DØ Collaboration), in *Proceedings of the XXVI International Conference on High Energy Physics, Dallas, Texas,* edited by J. R. Sanford (AIP, New York, 1993), p.1800; R. Brun and F. Carminati, CERN Program Library Long Writeup W5013, 1993 (unpublished).

[30] Scott S. Snyder, *Measurement of the top quark mass at DØ*, Ph.D thesis, State University of New York at Stony Brook, Stony Brook, New York (1995).

[31] R.Kehoe (DØ Collaboration), in *Proceedings of the sixth international conference on Calorimetry in High energy Physics, Frascati, Italy* (World scientific, River edge, NJ, 1996), Fermilab-Conf-96/284-E (1996).

[32] G. Marchesini *et al.*, Comp. Phys. Comm. **67**, 465 (1992).

[33] B. Abbott *et al.* (DØ Collaboration), Phys. Rev. D **58**, 4769 (1999).

[34] B. Abbott *et al.* (DØ Collaboration), Phys. Rev. D **61**, 072001 (2000).

[35] H. L. Lai, *et al.*, Phys. Rev. **D51** , 4763 (1995).

[36] F. A. Berends, H. Kuijf, B. Tausk and W. T. Giele, Nucl. Phys. B **357** , 32 (1991).

[37] S. Abachi *et al.* (DØ Collaboration), Phys. Rev. D **52** , 4877 (1995).

[38] Frank Paige and Serban Protopopescu, ISAJET, BNL Report 38034, Brookhaven, 1986, release v6.49 (unpublished).

[39] **DØNote 3061**, Measurement of top mass using lepton+jets events, Bhat P., Cochran J., Hsieh F., Jones M., Gilmartin R., McDonald J., Partridge R., Prosper H., Protopopiscu S., Snyder S., Strovink M., Trippe T., Varnes E., Watts G. (1997).

[40] T. Sjøstrand, Comput. Phys. Commun. **82**, 74 (1994).

[41] **DØNote 3943**, S. Jain, N.K. Mondal, D. Chakraborty, Search for $t\bar{t}$ resonance using DØ Run I data at Tevatron (2003).

[42] **DØNote 3281**, Stephen J. Wimpenny, Studies of the MuSmear Correction Factors for the Run 1b/c Single Top Analyses (1997).

[43] **DØNote 3282**, Stephen J. Wimpenny, Muon Efficiency Corrections for Single Top Analyses (1997).

[44] P. C. Bhat, H. B. Prosper, and S. Snyder, Phys. Lett. **B407** , 73 (1997).

[45] **DØNote 2716**, David Hedin *et al.*, Run 1b Muon Event Scanning (1995).

[46] **DØNote 2865**, Paul z. Quintas, Reconstruction and Selection Efficiencies for High p_T Muons in Run 1b (1996).

[47] John Hobbs, private communication, and his note at :
http://www-d0.fnal.gov/physics_analysis/top/mujets/mujets.html.

[48] **DØNote 2808**, H. Greenlee, N. Hadley, Theory of correlated errors in top quark background and cross section calculation (1995).

[49] F. James, MINUIT *Minimization Package Reference Manual*, 1994, CERN Program Library Number D506 (unpublished).